ELECTRICAL BREAKDOWN OF SF$_6$

AT HIGH PRESSURE

by

RUSSELL VELA, B.S.E.E.

A THESIS

IN

ELECTRICAL ENGINEERING

Submitted to the Graduate Faculty
of Texas Tech University in
Partial Fulfillment of
the Requirements for
the Degree of

MASTER OF SCIENCE

IN

ELECTRICAL ENGINEERING

Approved

Andreas Neuber
Chairperson of the Committee

Hermann Krompholz

Accepted

John Borrelli
Dean of the Graduate School

August, 2007

ACKNOWLEDGEMENTS

TABLE OF CONTENTS

ABSTRACT

This project was conducted to assist the upgrade of the Z-machine at Sandia National Laboratories. At Sandia, the 5.5 Megavolt Laser Triggered Gas Switch (LTGS) developed surface flashover within the PMMA envelope. This surface flashover occurs initially during the regular cascade switching process without affecting the switch's electrical performance. However, the switch will pre-fire in the successive shot. The damage to the envelope has to be repaired before normal switch operation can resume. One of the more probable failure modes is that the existing electric field on the surface of the envelope with the addition of the UV from the volume breakdown event initiates surface flashover.

A 340 kV system was designed which replicated conditions found in the LTGS between two adjacent backbone electrodes. Besides measurement of flashover delay times for different dielectric materials (Lexan, Acrylic, Epoxies, etc.), emphasis was put on the detailed characterization of the flashover phenomenology. Hence, in addition to voltage and current diagnostics, fast optical imaging of the flashover along with the acquisition of optical emission spectra (~200 nm to 700 nm) was employed.

This paper will investigate individually the two events that are occurring within the chamber, surface flashover and volume breakdown. The conclusions will serve to lay the groundwork for experiments to follow this paper which will directly investigate the impact of volume breakdown on flashover across surfaces in the vicinity of the volume breakdown in high pressure SF_6. Understanding the fundamental physical mechanisms and the extent to which these processes influence discharge behavior is vital to characterizing and modeling electrical breakdown in high pressure SF_6.

LIST OF TABLES

LIST OF FIGURES

CHAPTER 1

INTRODUCTION

With the new requirements in switching voltage, the present Z-switch design is deemed inadequate due to switch failure occurring after only a few shots. The primary failure mode in the Laser Triggered Gas Switch (LTGS) is surface flashover in the high pressure gas (SF_6, > 40 psig) on the inside of the PMMA envelope. This surface flashover occurs initially during the regular cascade switching process without affecting the switch's electrical performance. However, the switch will pre-fire in the successive shot. The damage to the envelope has to be repaired before normal switch operation can resume.

In the following experimental results of pulsed surface flashover, different dielectric materials and volume breakdowns in SF_6, primarily at high pressure, are presented. Results of flashover and volume breakdown in SF_6 at pressures from 10 Torr to atmospheric pressure can be found in Appendix B. Besides fast voltage and current monitoring of the breakdown event, an increased emphasis was put on imaging the event, as well as, gathering optical emission spectra (~200 nm to 700 nm) from it. The role of UV emission due to a volume SF_6 arc, potentially a flashover hold-off reduction cause, is discussed. The small scale experiments were designed to reproduce at least part of the conditions as they are found in the large 5.5 MV Z-switch.

1.1 Motivation

The motivation for this project was to assist in the upgrade of the LTGS for the Z-machine at SNL. A flashover event in high pressure SF_6 (~40 psig) frequently occurred on the inside of the PMMA envelope when the switch was pushed to a voltage exceeding 5.5 MV. This appeared to be one possible switch failure mode, and as such, warranted an investigation. Identifying the underlying physics of surface flashover in the switch environment; plus, the determining of key processes was necessary. The Center for Pulsed Power and Power Electronics at Texas Tech University has performed many experiments on surface flashover behavior over the past two decades. Recent research has investigated the effects of UV on a surface flashover event [1, 38].

An example of the LTGS at SNL can be seen in Figure 1.1. First, the trigger gap of the LTGS is broken down by a laser. This over-voltages the backbone electrodes, thus causing a cascaded breakdown over the backbone electrodes, see Figure 1.2. In failure mode, an additional breakdown path develops across the surface of the PMMA envelope, see Figure 1.3. The hypothesis of why the surface flashover event was occurring encompasses the entire system encased in the PMMA envelope. Dynamic electric field simulations had shown that the electric field on the PMMA envelope is not equal to zero during the closing process [39, 40]. This, plus the light and UV emitted from the volume breakdown of the backbone electrodes, was thought to be enough to initiate the surface flashover event on the envelope. SNL also requested surface flashover testing on various materials. These tests were mainly concerned with surface erosion, material composition changes, time delays and identifying possible dielectrics which exhibited better voltage hold off than the PMMA.
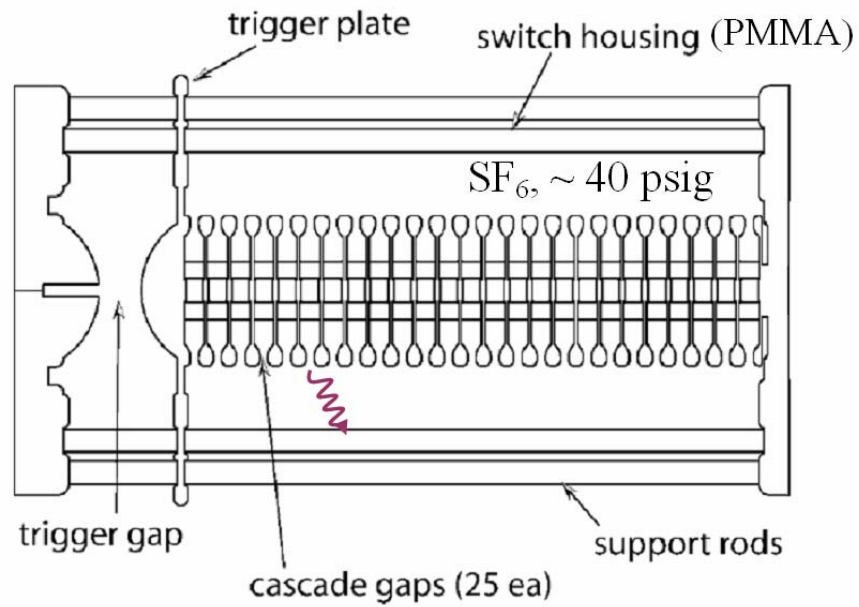
Figure 1.1: LTGS design [2]. Purple wave indicates light emission or UV.
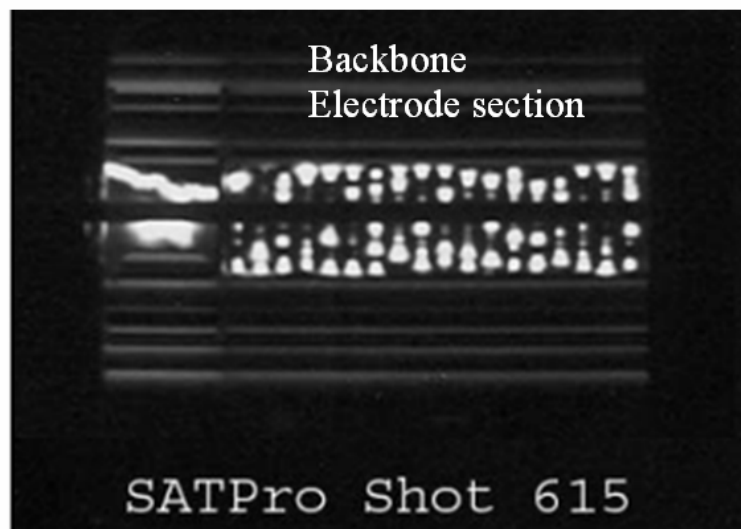
Figure 1.2: Example of normal operation of backbone electrodes (right) [2].
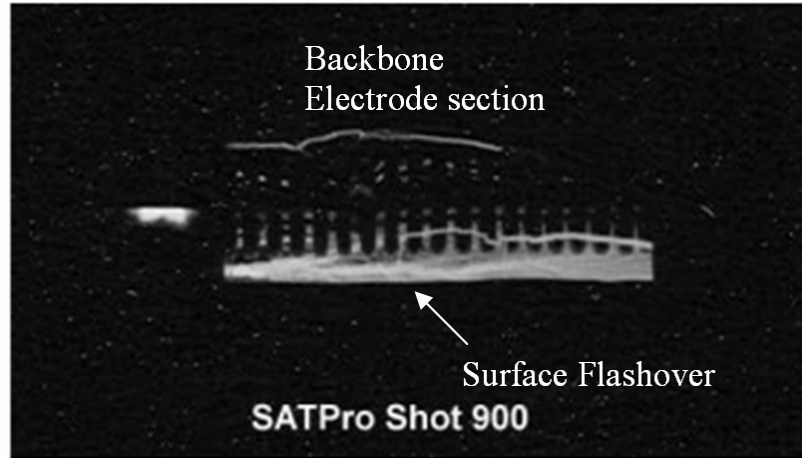
Figure 1.3: Example of failure in backbone electrode section [2]

In order to be able to identify how UV produced by a volume breakdown shapes a surface flashover event, both events had to be investigated in an environment closely mimicking the LTGS. This paper presents the foundations created for both volume breakdown and surface flashover in high pressure SF_6. Optically emitted spectra (~ 200 nm to ~700 nm), imaging of the event, fast current and voltage monitoring of surface flashover and volume breakdown will be discussed.

CHAPTER 2

. BACKGROUND

In order to better understand the processes involved in surface flashover, it is helpful to look at the known underlying fundamental mechanisms. Surface flashover is a complex situation, since the event contains a triple point junction. This is the point at which the dielectric material, electrode and gas meet. To better understand surface flashover, the junction can be investigated in two distinct categories. The first is from the interaction of the electrode material and the dielectric which results in the electron emission mechanisms. The second is from the gaseous electronics, which result in the ionization and electron loss mechanisms. The other processes which will be discussed are the Townsend Breakdown and streamer development.

2.1 Electron Emission Mechanisms

The emission of electrons from the surface is one dielectric surface flashover event. The main processes for electron emission when dealing with dielectric surface flashover are photoelectric and secondary electron emission. These processes are similar due to the fact that they must overcome the work function, $e\Phi$, of a particular material in order to extract an electron. The electron work function, $e\Phi$, is simply a measure of the minimum energy required to extract an electron from the surface of a solid [3]. Insulators, such as polycarbonate and nylon 66, have work functions of 4.26 eV and 4.08 eV, respectively [4]. It should be important to note that $e\Phi$ is dependent on the cleanliness of the surface and as such measurements reported in literature may often vary.

Table 2.1: Common insulators used in experimentation and their corresponding work function, $e\Phi$ [4].

Polycarbonate (Lexan)	4.26 eV
Nylon 66	4.08 eV
Polytetrafluoroethylene (PTFE, or Teflon)	4.26 eV
Polystyrene "Rexolite"	4.22 eV
Polyimide "Kapton"	4.36 eV
Polyethylene Terephthalate "PVC"	4.85 eV

2.1.1 Field Electron Emission

Field electron emission is directly related to the electric field strength and is relevant to the case at hand. For field emission to occur, the effective potential barrier at the surface of the material must become sufficiently low. For an electron leaving the surface, the field between can be approximated as a point charge and an equipotential plane. The potential energy from this field is found using Coulomb's law for the force on the electron and then integrating the expression from ∞ to x [5]. The result yields the potential barrier without an external field, see Figure 2.1, curve 1. Application of an electric field to the cathode yields the dashed line in Figure 2.1, curve 2. Thus, combining the energies represented by 1 and 2 produces a lowered potential energy curve, identified as curve 3 in Figure 2.1.
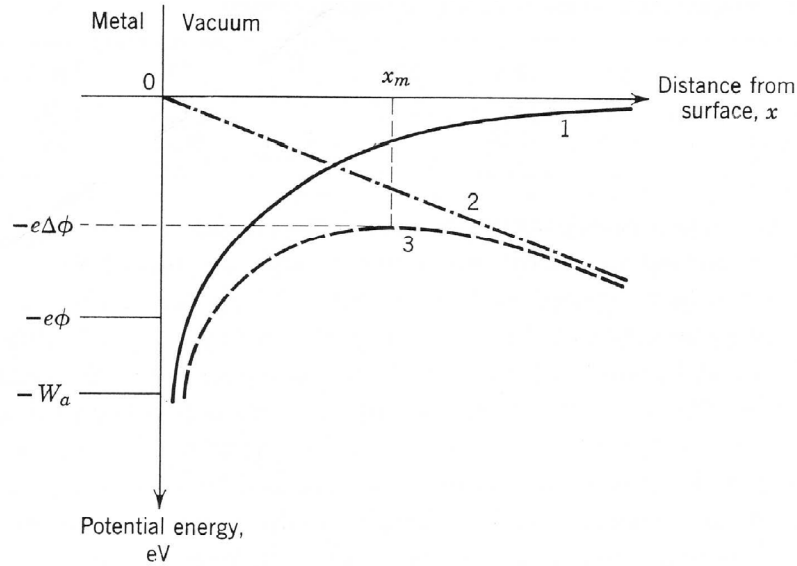
The lowering of the potential barrier by an external field: curve 1—energy curve with no external field, $-W = e^2/16\pi E_0 x$; curve 2— energy due to applied field, $-W_f = eEx$; curve 3—total energy curve, $W_t = W_f + W_e$.

Figure 2.1: Illustration of the effective potential barrier due to an applied field [5].

The modified potential barrier now has a height of finite value. However, electrons in the conduction band, range between $e\Phi$ and W_a in Figure 2.1, still do not have enough energy to overcome the barrier. Nevertheless, a quantum mechanical phenomenon, called "tunneling", allows or increases the probability that an electron will be able to penetrate through a barrier of finite height and thickness [6].

The emission current due to the applied field is described by the Fowler-Nordheim equation; see Equation 2.1 and Table 2.2 [5]. Currents of only a few microamperes require field intensities on the order of 10^8-10^9 V/cm [7]. The currents at lower fields are enhanced by microscopic protrusions and dielectric inclusions present on the material surface. These factors can increase local electric fields to intensities sufficiently high for field emission to occur [7]. The Fowler-Nordheim equation is

modified to include the influence of micro-protrusions by introducing β, the field enhancement factor. Typical values for β range somewhere from 10 to several 100 for vacuum environments [8] or from 1 to 250 for atmospheric air [9]. Thus, macroscopic fields much lower than 10^8 and 10^9 V/cm, such as those in the 10^6 V/cm range, can lead to significant field emission currents [7].

$$j = f \cdot \frac{(\beta E)^2}{e\Phi} \cdot e^{\frac{-g \cdot \Phi^{\frac{3}{2}} \cdot u}{\phi\beta E}}$$

(2.1)

Table 2.2: Variables for Fowler-Nordheim equation.

Variable (units)	Variable Definition
j (A/m^2)	current density
E (V/m)	macroscopic electric field
f	1.54 x 10^{-6}
g	6.83 x 10^9
$e\Phi$ (V)	work function
u	1-√(1.4 x 10^{-9} βE/Φ^2)

2.1.2 Photoelectric Emission

Photoelectric emission is the process by which electrons are released from liberated from a material by irradiating it with photons. The energies of incident photons, $h\nu$, are imparted upon the surface electrons. If the electron gains sufficient energy to overcome the work function, photoelectric emission occurs. With an energy $h\nu$ greater than the work required to liberate an electron, $e\Phi$, the remaining energy is found in the form of kinetic energy in the liberated electron. The energy necessary for electron emission (non-relativistic case) is expressed by [5]:

$$\frac{1}{2} \cdot m_e \cdot u_e{}^2 = h\nu = e\Phi \tag{2.2}$$

Table 2.3: Variables for photoelectric emission equation 2.2.

Variable (units)	Variable Definition
m_e (kg)	mass of electron
u_e (V/m)	electron velocity
h (kg m^2/s)	Planck's constant
ν (1/s)	photon frequency
$e\Phi$ (V)	work function

A quantity used for the characterization of photoelectric emission is the photoelectric yield γ. The photoelectric yield is the number of electrons per incident photon. Significant photoelectric yield, ~10^{-2} to 10^{-1}, typically occurs in the far UV or below the 200 nm range [7]. A list of work functions for various materials is located in Table 2.1. For a detailed explanation of photoemission see Reference [10].

2.1.3 Secondary Electron Emission

Secondary electron emission is the process of releasing a secondary electron from a dielectric surface by impacting it with another electron called the primary. For every primary electron incident on the dielectric's surface there is a certain probability that a secondary electron will be release from the surface. The yield, called δ, is the ratio of secondary electrons emitted for every primary electron. An important factor in the release of secondary electrons is the energy of the incident primary electrons, as well as, the penetration depth of the primary electron. Other factors in determining the yield are the material absorption coefficient and probability of escape. These factors are shown by the Gerald Dionne model [11]:

$$\delta = \left(\frac{B}{\xi}\right) \cdot \left(\frac{An}{\alpha}\right)^{1/n} \cdot (\alpha d)^{1/(n-1)} \cdot \left(1 - e^{-\alpha d}\right). \qquad (2.3)$$

Table 2.4: Variables for the Gerald Dionne model

δ	SEE Yield
B	Secondary escape probability
ξ	Secondary-Electron Excitation Energy
A	Primary Electron Absorption Constant
α	Secondary-Electron Absorption Constant
n	Power-Law Exponent
d	Maximum Penetration Depth

The curve shown in Figure 2.2 shows the yield of secondary electrons vs. the energy of the primary electrons. The curve has two "cross-over" points where the yield is equal to 1. The reason that the curve has a maximum at a certain level is that the electrons with too large an energy will penetrate deep into the surface and the secondary electrons will have a low probability of reaching and escaping the surface.
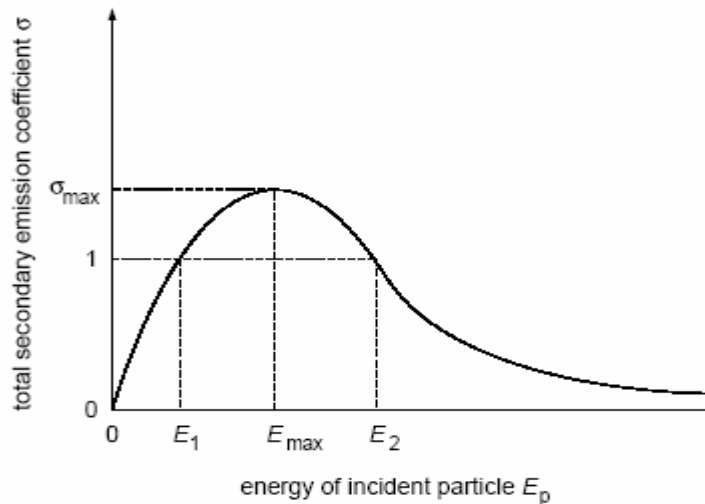
Figure 2.2: Graph of total SEE coefficient versus the energy of incident electron

10

2.2 Ionization and Electron Loss Processes

Electrical breakdown cannot occur without the presence of ionization and electron losses. In this experiment, a large contributor to ionization is the electric field between the electrodes. This field serves to accelerate free electrons and thereby increases the probability of impact ionization. The high field strength also can contribute electrons to this process by means of field electron emission. Photoelectric emission is another contributing factor due to UV radiation. It is essential to know exactly how charged particles are created and possibly lost within a gas that normally consists of neutral molecules only. Key types of ionization and de-ionization processes will be presented. Typical collision processes is presented in Table 2.5.

Table 2.5: Summation of typical collision processes, where A, B are atoms, A^*, B^* are excited atoms, A^+, B^+ are positive ions, e is an electron, A^+, B^+, e are ions and electron with appreciable kinetic energy , v is the frequency, and h is Planck's constant [12].

$A + e \rightarrow A^* + e$	Excitation by electron impact.
$A + e \leftarrow A^* + e$	A collision of the second kind.
$A + e \rightarrow A^+ + e + e$	Ionization by electron impact.
$A + hv \rightarrow A^*$	Photo excitation (absorption of light).
$A + hv \leftarrow A^*$	Emission of light.
$A + hv \rightarrow A^+ + e$	Photo-ionization.
$A + hv \leftarrow A^+ + e$	Radiative recombination.
$A + B \rightarrow A^* + B$	Excitation by atom impact.
$A + B \rightarrow A^+ + e + B$	Ionization by atom impact.

$A^* + B \rightarrow A + B^*$	Excitation by excited atoms.
$A^+ + B \rightarrow A + B^+$	Change of charge.
$A^+ + B \rightarrow A^+ + B^+ + e$	Ionization by positive ion impact.

2.2.1 Ionization Processes

The process of liberating an electron from a gas particle with either the simultaneous production of a positive ion, or with the increase of positive ion charge, is called ionization. Electron impact ionization is the most prominent gaseous mechanisms for increasing the number of liberated electrons within a gas. A sufficiently large applied electric field is the cause of ionization by accelerating free electrons and increasing the probability of collision and energy transfer with surrounding gas molecules. Free electrons for ionization mechanisms are also provided from field and photoelectric electron emission mechanisms, all of which contribute to final breakdown of the gas.

2.2.1.1 Impact Ionization

Electron impact ionization is a significant factor leading to breakdown in gases. Impact ionization results from the collision between an electron and a neutral atom. Dissociative ionization is a type of ionization dominant in molecular gases resulting in the disassociation of the molecule due to an electron collision [5]. A symbolic representation of impact ionization can be seen in Table 2.5.

Collisions may also free additional electrons or excite an atom or molecule to a higher state. A key factor in impact ionization is the application of an external electric field. In the presence of an applied field, electrons will experience a force parallel to the

field direction, thus accelerating free electrons. Electrons gain kinetic energy along the mean free path while being accelerated, increasing the probability that a collision will lead to ionization. The impact ionization cross sections for oxygen and nitrogen are shown in Figure 2.3 and for comparison the total ionization cross section of SF_6 is shown in Figure 2.4.
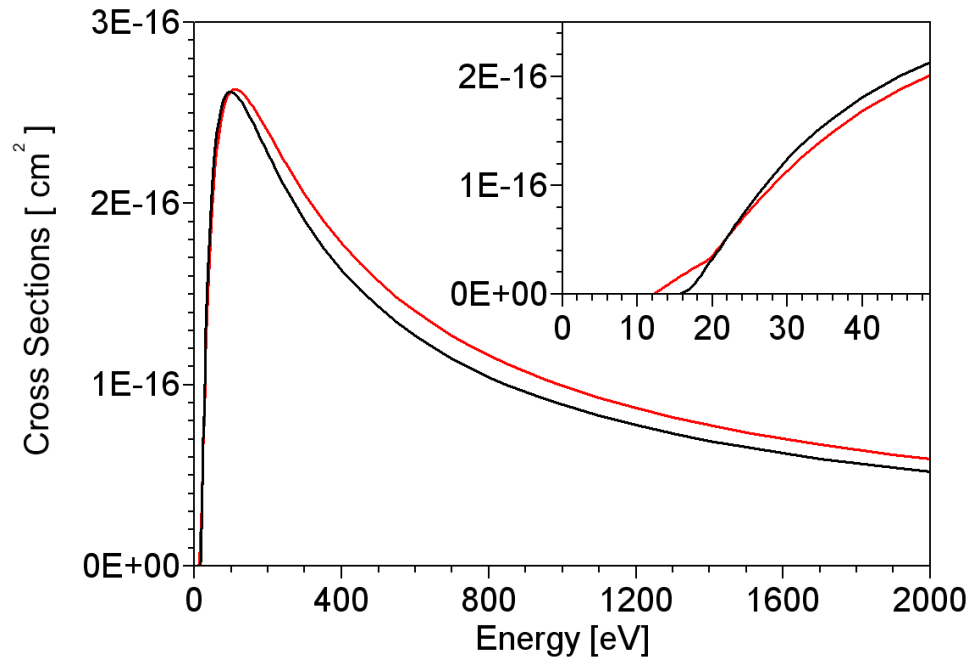
Figure 2.3: Impact ionization cross section for oxygen (red) and nitrogen (black) [14].
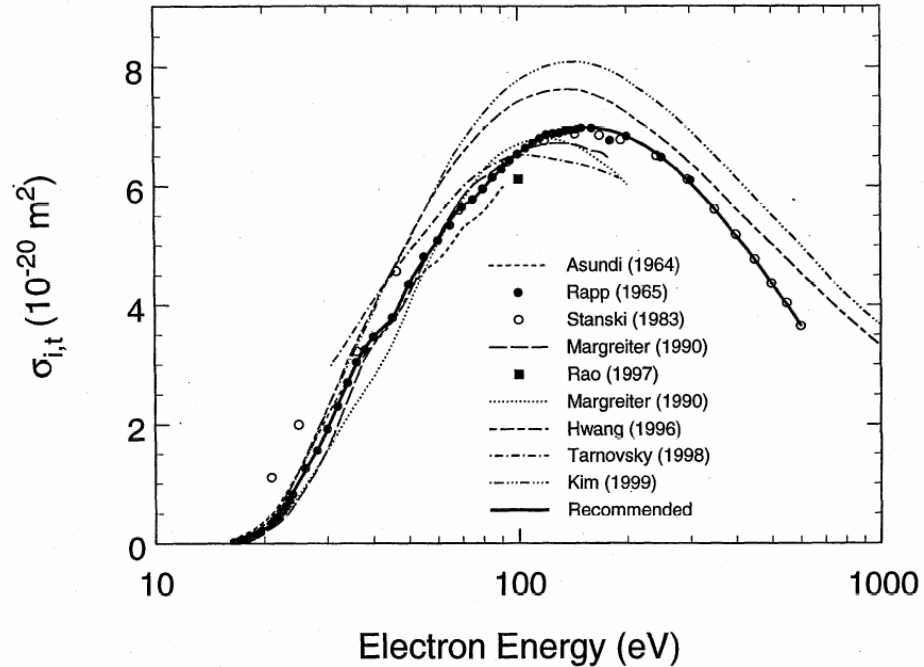
Figure 2.4: Total electron-impact ionization cross section for SF_6 as a function of electron energy [13].

It is of great importance to quantify the number of ionizing collisions a single electron undergoes over a certain distance, including the distance from the cathode to the anode. The number of electrons per unit length in the field direction is the called the ionization coefficient, α, or *Townsend's first ionization coefficient*. The first ionization coefficient, α, is also the number of ions produced due to the fact that each ionization event produces a secondary electron and positive ion. The equation for α at high values of E/p and moderate energy levels can be approximated to [5]:

$$\alpha = \mathrm{A}p\, e^{-\left(\frac{\mathrm{B}p}{\mathrm{E}}\right)}$$
(2.4)

Table 2.6: Variables for equation to solve Townsend's first ionization coefficient

$\alpha(\mathrm{cm}^{-1})$	Townsend's First Ionization Coefficient
$\mathrm{A}(\mathrm{cm}^{-1}{\cdot}\mathrm{torr}^{-1})$	Constant Related to Temperature
$\mathrm{B}(\mathrm{V/cm{\cdot}torr})$	Constant Related to Type of Gas
$p(\mathrm{torr})$	Atmospheric Pressure
$\mathrm{E}(\mathrm{V/m})$	Electric Field

Gas	A ion pairs $cm^{-1}\,Torr^{-1}$	B $V\,cm^{-1}$ $Torr^{-1}$	E/p range $V\,cm^{-1}\,Torr^{-1}$	V_i volts
H_2	5	130	150–600	15.4
N_2	12	342	100–600	15.5
air	15	365	100–800	–
CO_2	20	466	500–1000	12.6
He	3	34	20–150	24.5
Hg	20	370	200–600	–

Figure 2.5: Selected ionization constants and ranges of applicability. T = 20 ºC. [15]

2.2.1.2 Photoionization

Ionization may occur due to absorbtion of energy from either an external radiation source or background radiation gas. In the case of an incident photon on a gas molecule, ionization occurs if $hv \geq W_i$, where W_i is the ionization energy of the gas molecule and hv is the energy of the photon. The relationship can be expressed in the form:

$$\frac{ch}{\lambda} \geq W_i$$
(2.5)

Ultraviolet light, in the range of 125 nm, has been shown experimentally to have sufficient energy to ionize a majority of gases [5]. Thus, any VUV emitted during the

breakdown process, or provided by an external UV source, will have a significant impact on the importance of photoionization leading to flashover. The total photodissociation and total photoionization cross sections for SF_6 is shown in Figure 2.6
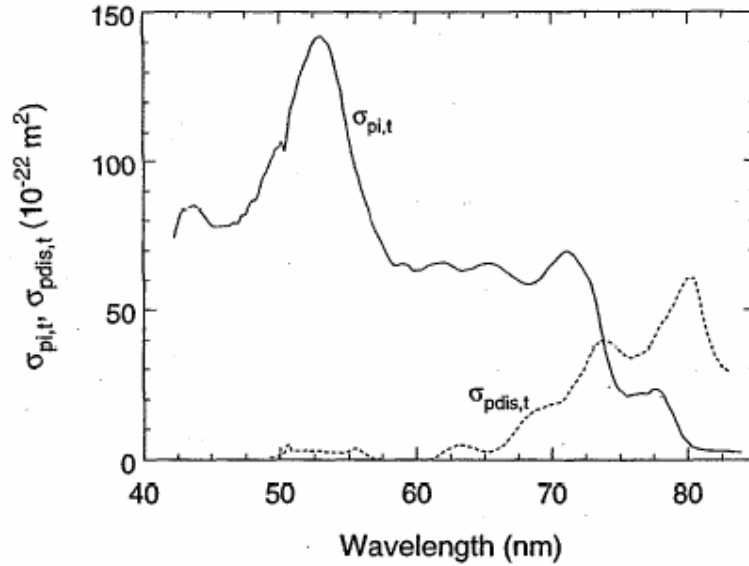
Figure 2.6: Total photodissociation $\sigma_{pdis,t}(\lambda)$, and total photoionization $\sigma_{pi,t}(\lambda)$, cross sections of SF_6 as a function of photon wavelength [13].

2.2.2 Electron Loss Processes

Diffusion, recombination and electron attachment are loss mechanisms that reduce the number or energy of free electrons in the background gas. These processes occur simultaneously along with electron amplification mechanisms, such as ionization. Gaseous breakdown can only occur if the rate of ionization is greater than the rate of de-ionization. Symbolic examples of de-ionization are seen in Table 2.5.

2.2.2.1 Diffusion

Diffusion is a process by which the particles of one type (in this case charged particles) spread throughout a volume of particles of a second type (neutral particles)

until the concentration difference of both particle densities in the volume in the absence of any external forces present, goes to zero. The primary factor contributing to diffusion is the natural thermal chaotic motion of all particles in a gas. The process of diffusion removes charges carrying particles from a potential breakdown channel.

The constant of proportionality between the rate of flow and the concentration gradient is known as the *diffusion coefficient*, D, and is given by

$$D = \frac{1}{3} \bar{\lambda} \bar{\upsilon} \qquad \text{m}^2/\text{sec} \tag{2.6}$$

with υ as the average velocity and λ as the mean free path of the charged particles [5]. It is important to note that D is proportional to p^{-1}.

2.2.2.2 Recombination

Whenever there are positively and negatively charged particles present, recombination takes place. The potential energy and the relative kinetic energy of the recombining electron-ion is released as quantum of radiation. Symbolically the reaction can be seen in Table 2.5.

At high pressures, ion-ion recombination takes place. The rate of recombination in either case is directly proportional to the concentration of both positive and negative ions. For equation concentrations of positive ions, n_+ and negative ions n_- the rate of recombination

$$\frac{dn_+}{dt} = \frac{dn_-}{dt} = -\beta n_+ n_- \tag{2.7}$$

where β is a constant known as the recombination rate coefficient.

Since $n_+ \approx n_- = n_i$ and if it assumed at time t = 0: $n_i = n_{io}$ and at time t: $n_i = n_i(t)$, then equation (2.7) becomes

$$n_i(t) = \frac{n_{io}}{1 + n_{io}\beta t} \qquad (2.8)$$

The variation of the recombination rate coefficient β with pressure in air is shown in Figure 2.7. The recombination process is particularly important at high pressures for which diffusion is relatively unimportant [15].
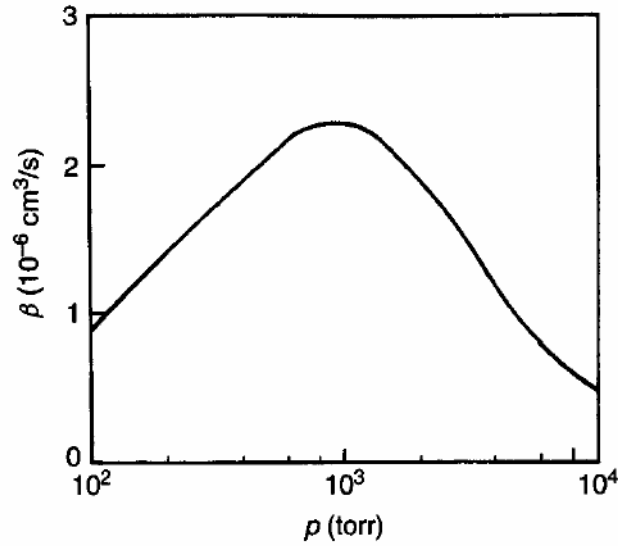
Figure 2.7: Recombination coefficient (ion-ion) in air at 20 °C [15].

2.2.2.3 Electron Attachment

In electronegative gases (gases with unfilled outer electron shells) such as SF_6, the attachment of electrons to gas particles is a common deionization process. This type of attachment is also known as dissociative electron attachment [5]. Like deionization, attachment results in decreasing the amount of free electrons within the gas and reducing

18

the likelihood of breakdown. The *probability of attachment* [16], *h*, is sometimes given as β, which is analogous to the first ionization coefficient α and is given by

$$\beta = \frac{\upsilon_a}{\mu E} \tag{2.9}$$

with υ_a as the frequency of attachment and *E* as the applied field.
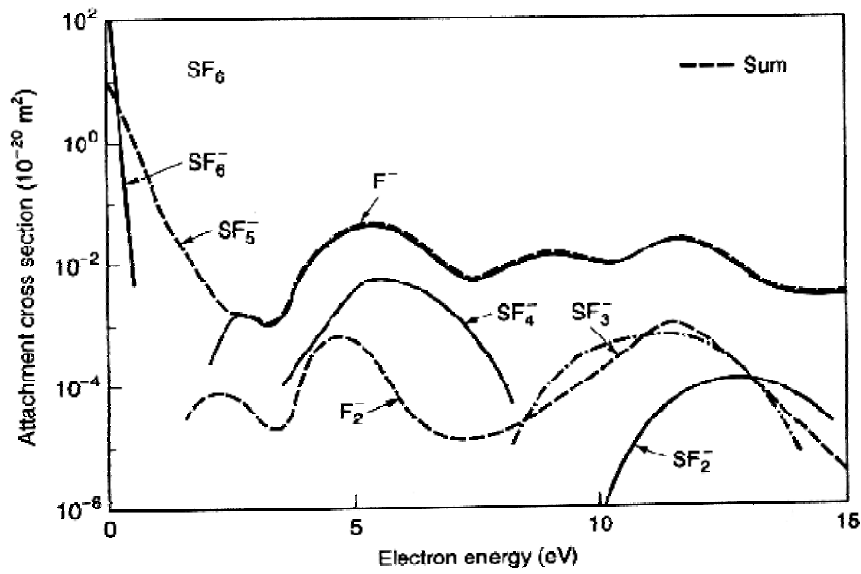
Figure 2.8: Direct and dissociative attachment cross section of SF_6 as a function of energy [17].

2.3 Electrical Breakdown Mechanism

Electrical breakdown is a colloquial term used to describe the process by which a nonconducting medium becomes conductive through the application of a sufficiently strong electric field. There exist many comprehensive literature sources describing the characteristics of electrical breakdown mechanisms, including but not limited to books by Nassar, Raizer, Meeks and Loeb [5, 7, 12, 18].The mechanisms leading to gaseous

19

breakdown, studied by Townsend, Raether, and Nasser, will be discussed in the following sections.

2.3.1 Townsend Mechanism

As the voltage between electrodes in a gas increases, the electrode current at the anode increase in accordance. Until at some point there is a sudden transition from dark current to a self sustaining discharge, Figure 2.9. J.S. Townsend observed that an applied voltage results in a linear increase to point V_1. Past V_1, the current remains constant until a threshold point is reached V_2. The increase in current beyond V_2 Townsend ascribed to ionization of the gas by electron collision. As the field increases, electrons leaving the cathode are accelerated more and more between collisions until they gain enough energy to cause ionization on collision with gas molecules or atoms [15].
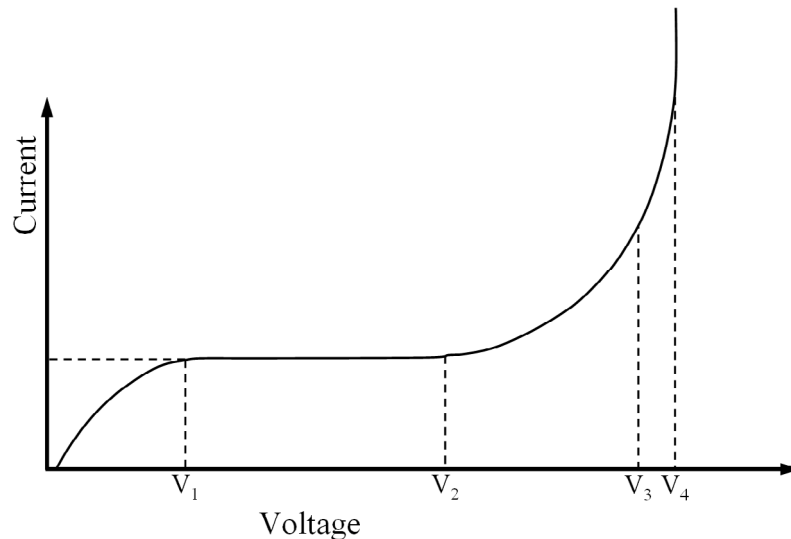
Figure 2.9: Current vs. voltage relationship developed by Townsend [15].

This observation led Townsend to introduce a quantity known as *Townsend's first ionization coefficient*, α. The ionization coefficient expresses the number of ionizations

produced by an electron per unit length of path in the direction of the applied electric field. Equation 2.4 is the empirical formula used to derive Townsend's first ionization coefficient, Section 2.2.1.1.

For the point beyond V_2, Townsend developed Equation 2.10 to quantify the number of electrons at distance x from the cathode in the direction of the applied field [15]. A loss coefficient, η, accounts for deionization and attachment mechanisms leading to a reduction in the number of unbound electrons. Equation 2.10 can also be expressed in terms of the current leaving the cathode, I_0, see Equation 2.11 [15].

$$n = n_o \cdot e^{(\alpha - \eta) \cdot d} \tag{2.10}$$

Table 2.7: Variables for describing electron amplification in Equation 2.10.

Variable (units)	Variable Definition
n (m^{-3})	electron density
n_o (m^{-3})	electron density at cathode
α (m^{-1})	Townsend's first ionization coefficient
η (m^{-1})	loss coefficient
d (m)	distance from cathode

$$I = I_o \cdot e^{(\alpha - \eta) \cdot d} \tag{2.11}$$

Table 2.8: Variables for describing current due to electron amplification, Equation 2.11.

Variable (units)	Variable Definition
I (A)	current
I_o (A)	current leaving cathode

The exponential growth of electrons, expressed by Equations 2.10 and 2.11, is called an electron avalanche. Avalanches develop in the direction opposite of the applied electric field. High mobility electrons advance towards the anode leaving heavier positive ions behind at the cathode [5]. The relatively immobile ions stay behind and form the avalanche tail, while the mobile electrons form the spherical avalanche head, Figure 2.10. Compared with the applied field, the field behind and ahead of the avalanche is increased by the space charge and reduced between the electron and ion clouds. The variation in the field around the avalanche is shown in Figure 2.10.

According to Raether, [19], UV light emitted in recombination and de-excitation events creates electrons by photoionization ahead and behind the avalanche, initiating further avalanches; which finally forms a conducting bridge between the anode and cathode. Because of the higher fields at the ends of the avalanche, electrons created there can cause ionization more efficiently. This kind of discharge is called the streamer mechanism and will be discussed in the following section [20].
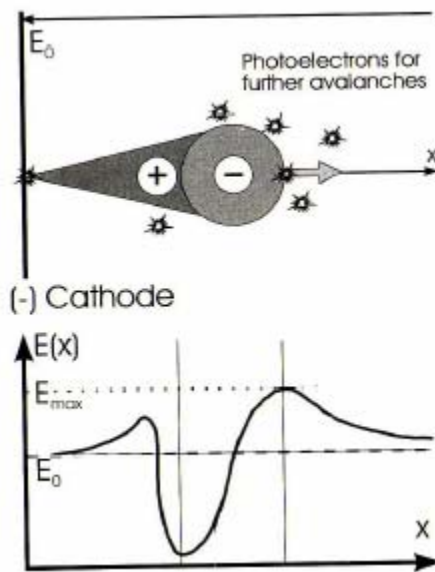
Figure 2.10: Diagram of the electron avalanche structure and effect of space charge [20].

22

2.3.2 Streamer Formation

As mentioned above, streamer formation is the event in which the channel is formed between the anode and cathode via multiple electron avalanches. An explanation of streamer formation is taken from Nasser [5] see Figure 2.11. In part (a) of Figure 2.11, the developing avalanche creates a space charge on the order of the externally applied electric field. The associated high amplitude fields allow the electrons in the head of the avalanche to acquire higher energy, leading to increased UV emission. In part (b), absorption of the UV radiation by neutrals leads to seed electrons for a second generation of avalanches. As the positive space charge bridges the gap as shown in (c), the secondary avalanches are attracted to the positive space charge trunk. In part (d), the accumulation of positive ions at the cathode has increased by the addition of two auxiliary streamers, and an ionization channel is forming between the anode and cathode. Two subsequent streamer branches grow into incoming avalanches in (e) whereas one dies out due to the lack of incoming avalanches in (f). If the process continues, the streamer will eventually bridge the gap as shown in part (g), and the ionization channel becomes the breakdown path.
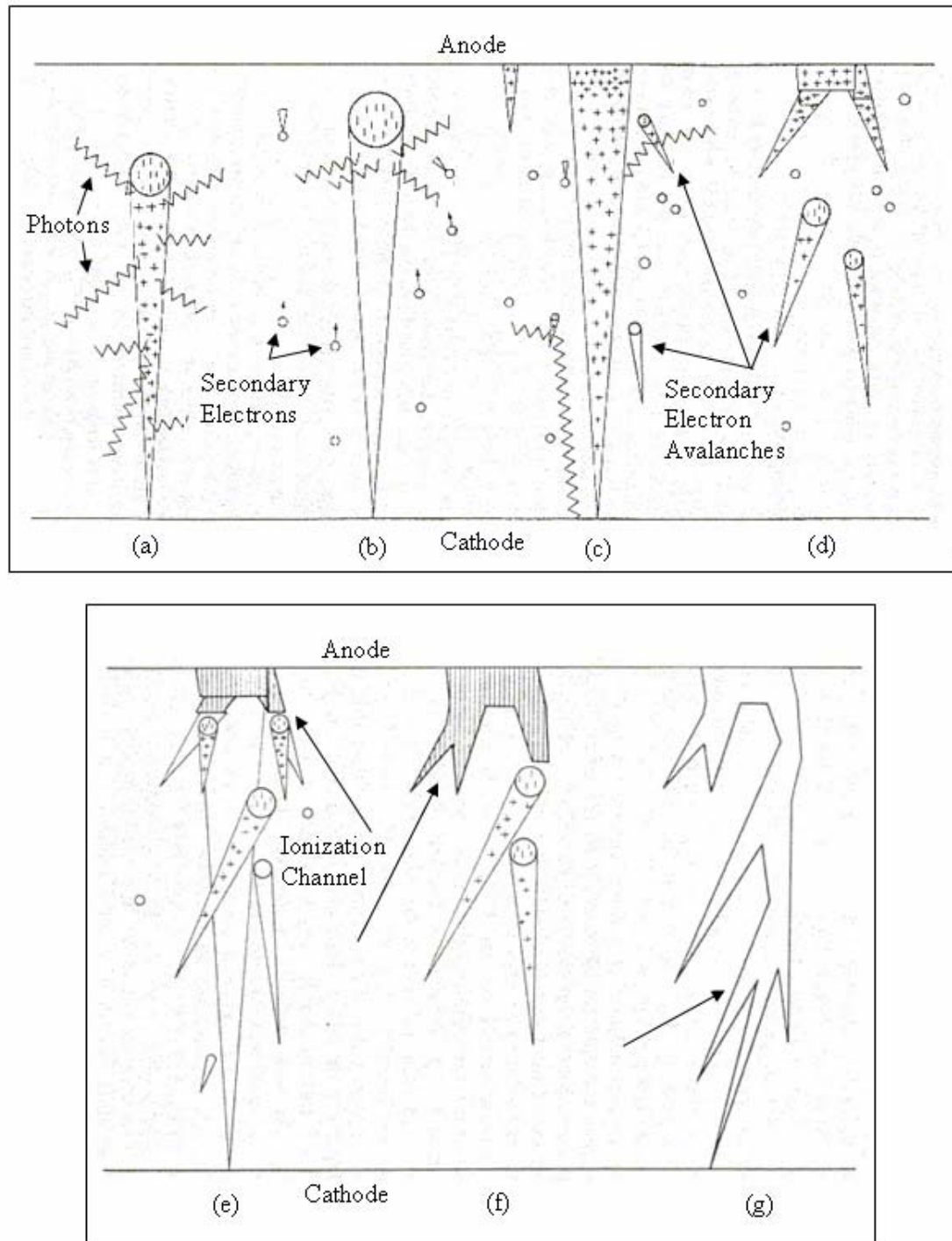
Figure 2.11: Diagram of the stages of streamer formation [5].

The transition from a Townsend breakdown to a streamer breakdown is illustrated in Figure 2.12. In part (a), an avalanche emits photons to produce photoelectrons at the cathode. Part (b), the photoelectrons then produce avalanches of varying size with electrons drifting at the same velocity. Next, positive space charge is accumulated at the anode enhancing the field and augmenting the avalanche size to reach the critical size, in part (c). Finally, a streamer grows from the avalanche toward the cathode by the oncoming avalanches, part (d).
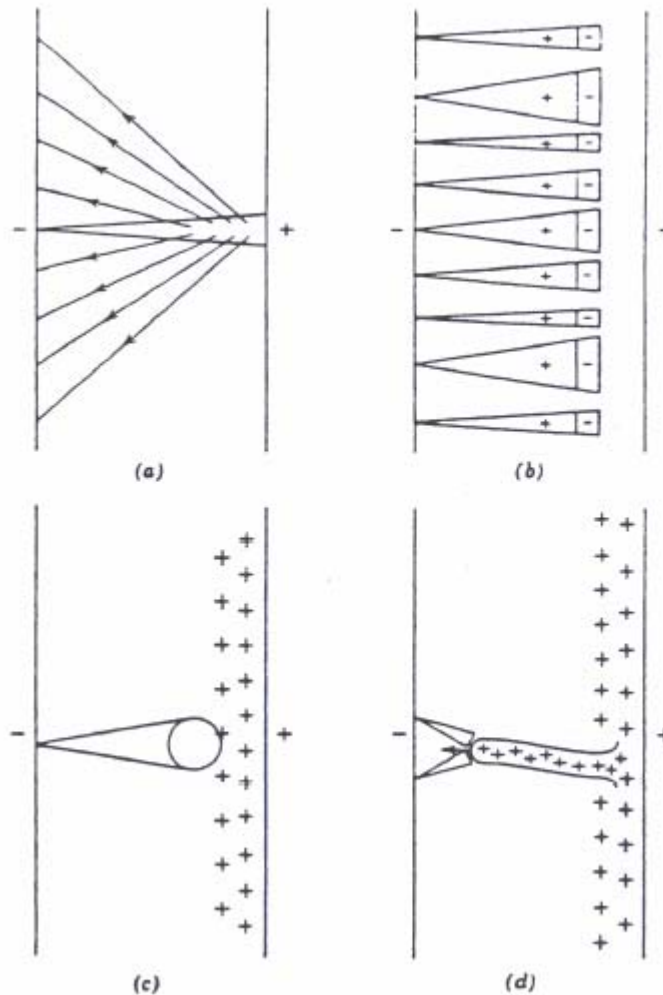
Figure 2.12: The transition of a Townsend (generation) type of breakdown to a streamer breakdown [5].

2.3.3 Secondary Electron Emission Avalanche

Secondary Electron Emission Avalanches (SEEA) are one of the most widely accepted mechanisms that contribute to surface flashover in vacuum [21]. In SEEA, electrons are emitted from the surface of a dielectric via secondary emission due to the impact of some primary ion or electron incident upon the surface. Once free from the surface, the electrons experience acceleration parallel to the surface in the direction of the applied electric field. The process of liberating electrons from the dielectric surface leaves a net positive charge on the surface, and thus, a DC restoring field appears. This restoring field accelerates the "freed" electrons back towards the surface. If the applied field is large enough, the freed electrons will impact the surface of the dielectric with enough energy to liberate more electrons, having gained this energy from the applied electric field in the time of flight between departing from and returning to the surface. The continuation of this process leads to a SEEA illustrated in Figure 2.13.
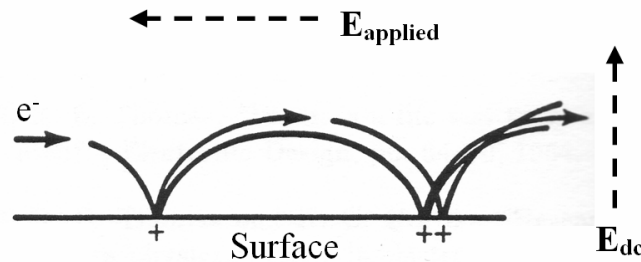
Figure 2.13: Diagram of secondary electron emission avalanche

An important parameter in the development of SEEA is the "hopping distance" of the electrons, i.e. the lateral range of the electron trajectory [44]. For Lexan with a gap distance of 1 cm and an applied breakdown field of 20 kV/cm, the average value for

26

hopping distance is 22 μm and about 2 μm for the maximum height above the surface. Since the mean free path in SF$_6$ at high pressures is much less than 22 μm (< 100 nm), an SEEA will not develop under the conditions given by the described high pressure flashover experiments.

2.3.4. Paschen's Law

The *second Townsend coefficient*, γ, allows for a discharge to become self-sustaining. In the case of SF$_6$, γ is most likely due to photo emission, and is generally represented by

$$\gamma(e^{\alpha d} - 1) = 1 \tag{2.12}$$

meaning that each initial electron must produce at least one secondary electron to make the discharge self-sustaining. When discussing the Townsend breakdown mechanism, it can be shown that the αd in equation 2.12 is equivalent to ηV_b [22, 16]. η is the ionization proportionality constant related to the applied electric field and is given by:

$$\eta = \frac{\alpha}{E} \tag{2.13}$$

Substituting these into equation 2.12 and rearranging shows that the breakdown voltage can be written as:

$$V_b = \frac{Bpd}{\ln\left[\dfrac{Apd}{\ln\left(1 + \dfrac{1}{\gamma}\right)}\right]} \tag{2.14}$$

A and B values for various gases can be found in Figure 2.5. This method of relating the breakdown voltage as a function of pd is known as Paschen's Law. From equation 2.14, it can be seen that at large and small values of pd, the breakdown voltage V_b increases. Consequently, V_b must go to a minimum which is called the Paschen minimum. Calculation of this minimum breakdown voltage gives:

$$V_{b(min)} = 2.718 \ln\left(1 + \frac{1}{\gamma}\right) \frac{B}{A} \tag{2.15}$$

Similarly, the minimum value of pd is found to be:

$$pd_{b\,min} = 2.718 \frac{\ln\left(1 + \frac{1}{\gamma}\right)}{A} \tag{2.16}$$

With a voltage lower than the V_{bmin}, it is impossible to cause the breakdown of a gap with a uniform distribution, no matter what the pressure or spacing [20].
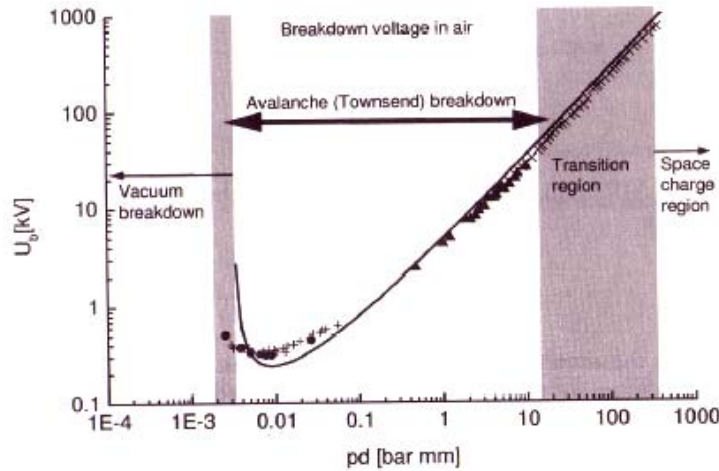
Figure 2.14: Measured and calculated Paschen curves for atmospheric air [20].

28

Gas	$(pd)_{min}$ torr cm	V_{bmin} volts
Air	0.55	352
Nitrogen	0.65	240
Hydrogen	1.05	230
Oxygen	0.7	450
Sulphur hexafluoride	0.26	507
Carbon dioxide	0.57	420
Neon	4.0	245
Helium	4.0	155

Figure 2.15: Minimum breakdown voltages for various gases [15].

In electronegative gases, in which attachment is significant, the Paschen law holds in general and specifically within a limited range around the breakdown minimum [23]. There are many literature sources for Paschen's law with respect to SF_6 [24, 25]. The Paschen curve with respect to SF_6 can be found in Appendix A.

2.3.5 Static Breakdown of SF_6

To describe the breakdown properties of electronegative gases such as SF_6, the attachment coefficient η must be considered. η defines the attachment probability of an electron per unit path length. Similarly to α/p, η/p is a unique function of E/p. The effective ionization coefficient α_e is defined as the difference between α and η:

$$\alpha_e = \alpha - \eta = pf\left(\frac{E}{p}\right) \qquad (2.17)$$

Electron avalanche formation becomes possible only if α_e is greater than 0. For SF_6, this is the case if E/p is greater than 8.84 kV/ (mm*bar). $(\alpha - \eta)$/p can be expressed as a linear function of E/p as seen in Figure 2.16 [20].

$$\frac{(\alpha - \eta)}{p} = k\left[\frac{E}{p} - \left(\frac{E}{p}\right)_o\right] \tag{2.18}$$

For SF_6, k = 27.7 kV and $(E/p)_o$ = 8.84 kV/ (mm*bar). Using these parameters and the linear relationship (2.18) to determine the static breakdown voltage V_b for a uniform field the following can be obtained:

$$V_b = pd8.84[kV / mm * bar] + 0.5kV \tag{2.19}$$
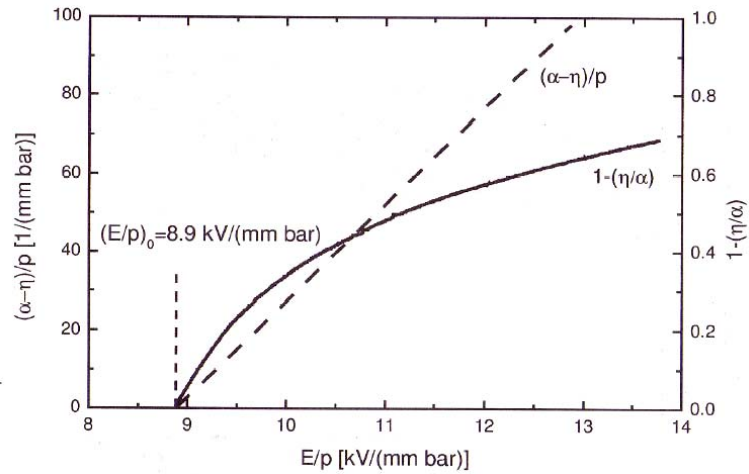
Figure 2.16: Effective ionization coefficient $(\alpha - \eta)$/p and weight function $1 - (\eta/\alpha)$ describing the probability that an electron creates further avalanche electrons, for SF_6 [20].
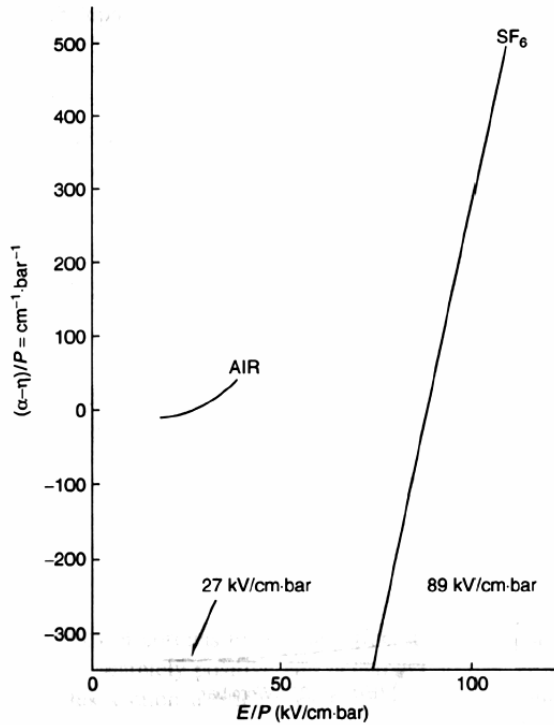
Figure 2.17: $(\alpha-\eta)/p \sim E/p$ relationship in SF_6 [15].

2.4 Surface Flashover

Dielectric surface flashover in vacuum has been studied rather extensively and the

processes involved have been documented. It is upon these processes that the theoretical

basis for flashover at high pressures has been derived. The prevalent model divides this

type of surface flashover into three stages: (a) initiation, (b) growth and (c) gaseous

ionization along the surface of the dielectric [21].

It is generally accepted that the initiation is triggered by the field emission of

electrons at the cathode triple point [21, 26]. The triple point is a term which describes

the point at which the dielectric, electrode and vacuum intersect. The most commonly

accepted mechanism of the second stage is a SEEA, see Section 2.3.3. The final stage of

31

surface flashover in vacuum is generally accepted as an event which involves gaseous ionization near the surface due to atoms or molecules desorbed by the SEEA [21].

Given these processes at the vacuum level, one could speculate that at higher pressures, it is more probable that a discharge develops as a result of impact ionization versus desorption as seen for vacuum flashover. In addition, since molecules are more abundant at high pressures, the spark channel is not limited to just developing near the dielectric surface.

CHAPTER 3

EXPERIMENTAL SETUP

As stated earlier, the experimental chamber accommodated volume breakdown, surface flashover and a system that would allow for the testing of volume breakdown effects on surface flashover. To develop this environment within the chamber, two separate HV pulse systems were created as seen in Figure 3.1, 3.2. The primary system allowed for a high voltage/high current discharge which could also be adjusted to administer a high voltage low current setup. Interchangeable electrodes made both volume and surface flashover tests possible. The secondary system was designed to be used in testing the effects of an electric field on a surface and UV produced from a volume gap. As such, the electrode configuration was strictly a surface flashover design, see Figure 3.3.
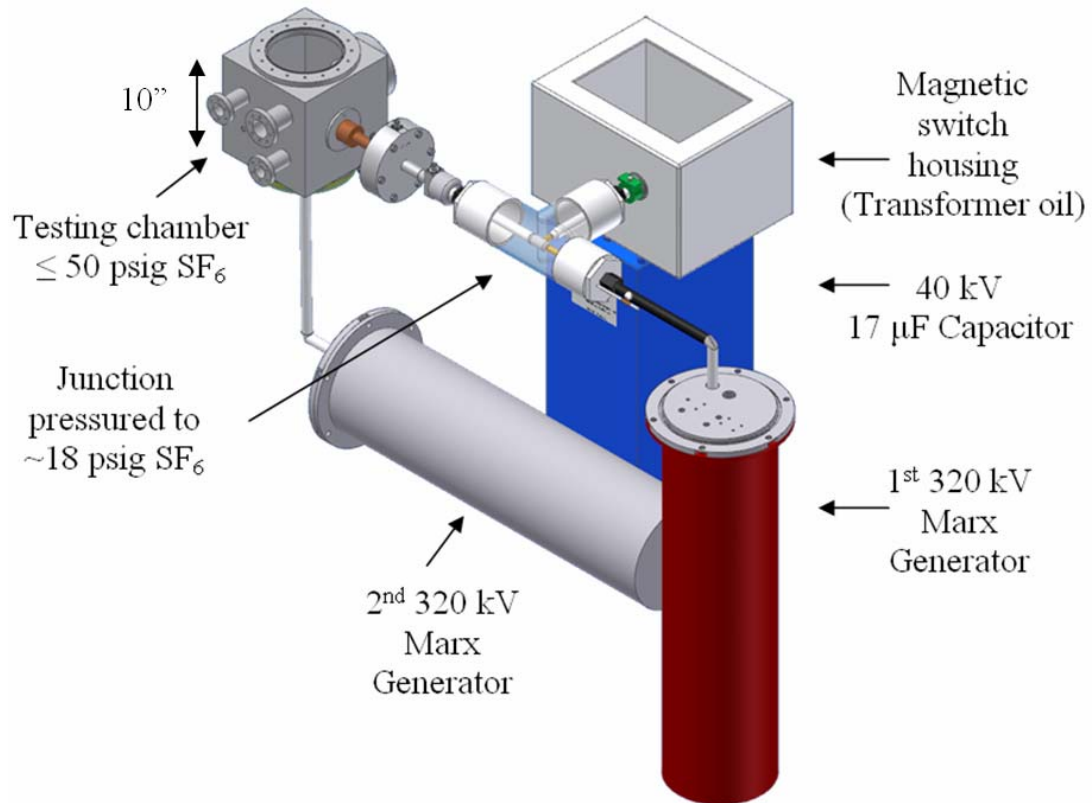
Figure 3.1: Experimental setup for pulsed volume and surface flashover testing.
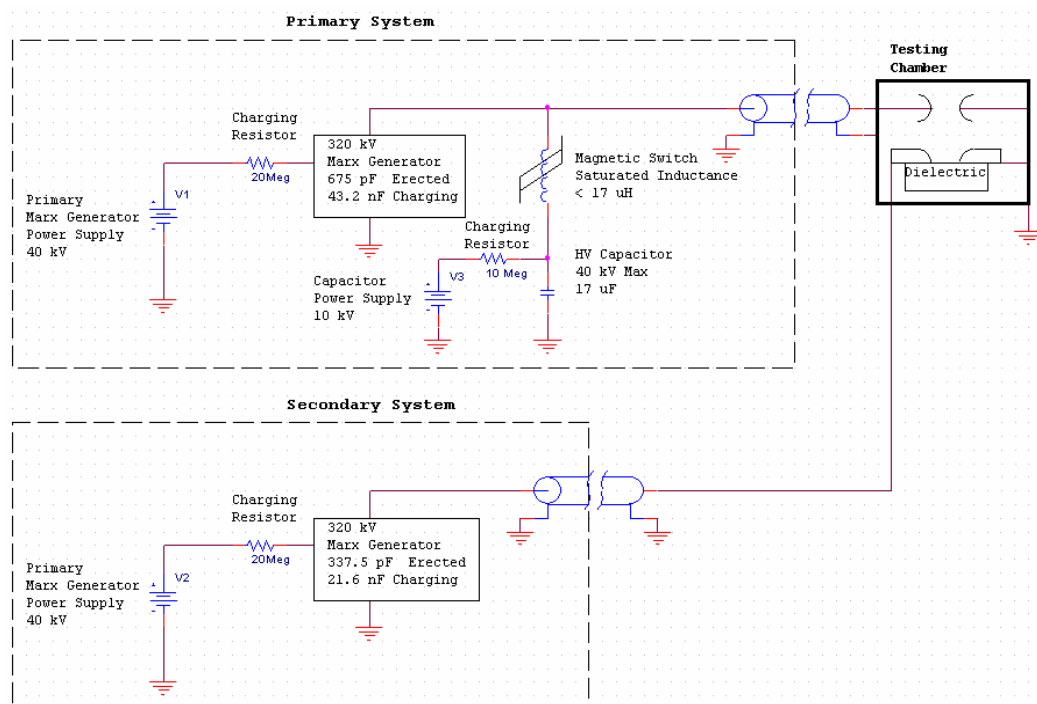
Figure 3.2: Overall circuit diagram of testing setup.

Figure 3.3: Secondary setup surface flashover electrode configuration.

3.1 Experimental Test Chamber

The experimental testing chamber was designed to house essentially two separate electrode systems, allow for maximum accessibility and have visibility of the electrodes for imaging, see Figure 3.4. The chamber is composed of approximately 0.1 inch stainless steel and has external dimensions of 10x10x10 inches. The chamber has a 1 inch Lexan (polycarbonate) lid which seals via an o-ring to the top flange. There is also a one inch thick epoxy lid used for sealing the bottom of the chamber. A plastic compression flange allows the secondary system to enter the chamber from the epoxy lid. For an added viewport, the front of the chamber has a 1 in thick quartz window with a 3 inch diameter and a top surface accuracy of $\lambda \, {}^{1}\!/_{10}$ and a polished bottom surface from Edmund Industrial Optics (Stock # 32640, Serial # 361). The chamber also has ports for the vacuum system, SF_6 pressure adjustment, over pressure valve, fiber optic lines for spectra imaging and a relief system which will all be discussed in the following sections.
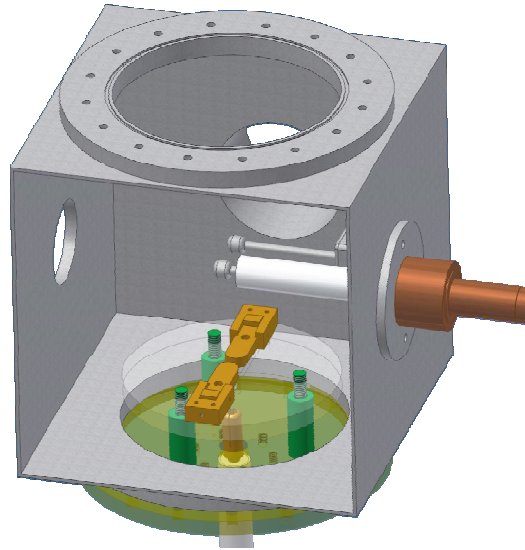
Figure 3.4: View of chamber internals with both primary and secondary gaps installed.

The electric field at the coaxial line chamber entrance caused surface flashover issues from the electrodes to the chamber, see Figure 3.5.
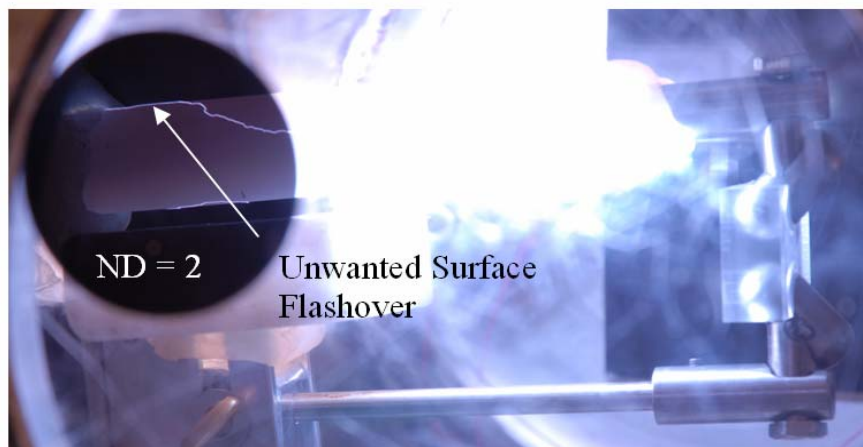
Figure 3.5: Example of surface flashover to chamber wall.

To remedy the field enhancement found at the RG220 entrance, static electric field simulations using Maxwell 3D and 2D were used to help minimize field strength, see Figure 3.6. After many designs, a toroidal corona ring was designed which attached to the chamber wall and a plastic compression flange was used to replace a previously existing

metal one. The combination of these two fixes through simulations showed a reduction in electric field strength, see Figure 3.6.
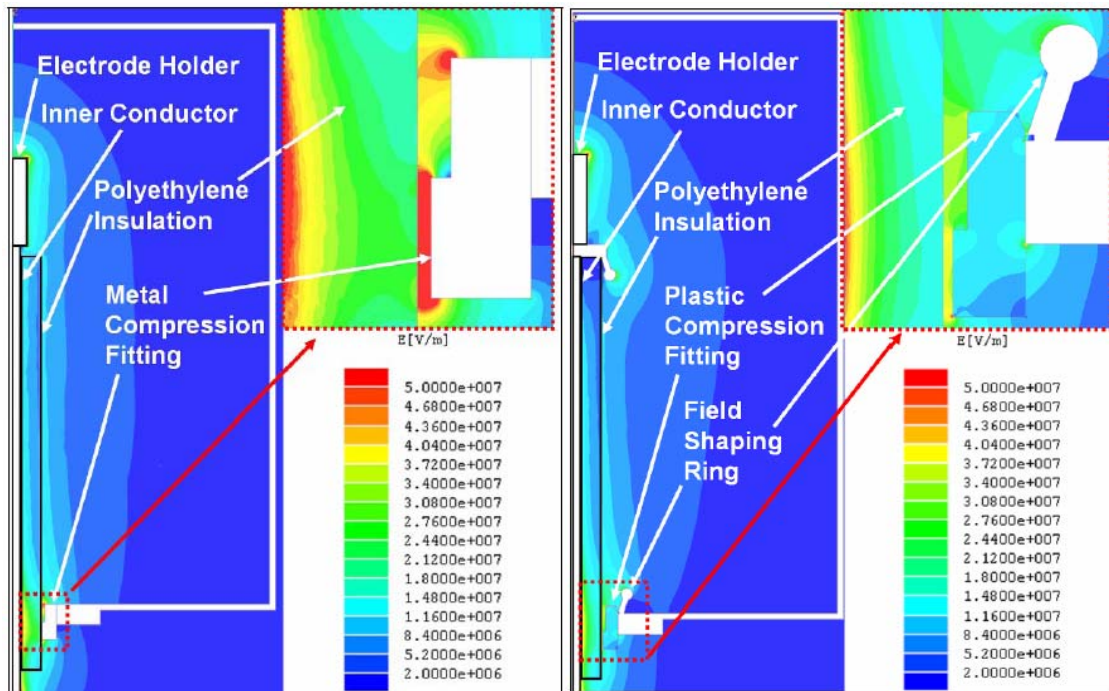
Figure 3.6: Maxwell 3D simulations showing original field enhancements (left) at chamber entrance and the field reductions (right) after improved feedthrough design. Applied voltage = 320 kV.

3.2 Charging System

The experimental setup had two independent charging systems. The first was used to charge the primary Marx generator, the HV capacitor and the trigger pulsers, see Figure 3.7. The second system had only the secondary Marx generator to charge. Each of which will be discussed thoroughly in their respective sections. For a list of component specifications, see Table 3.1.
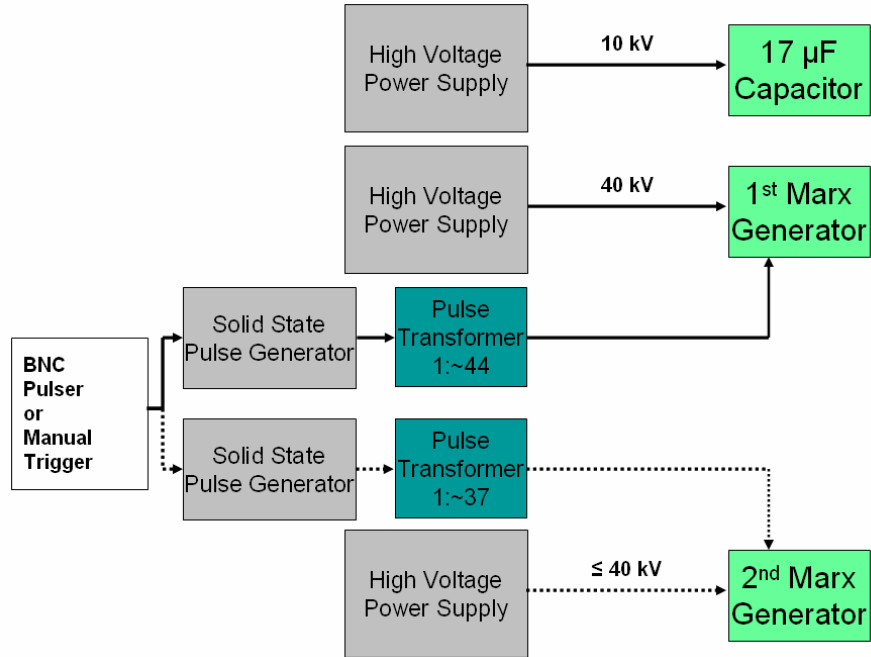
Figure 3.7: Charging setup of overall system.

Table 3.1: Overall delivery system component characteristics

Primary Marx Generator	Erected capacitance: 675 pF Charging capacitance: 43.2 nF Maximum stored charge: 229.5 μC Maximum voltage: 340 kV Maximum energy: 39 J
Secondary Marx Generator	Erected capacitance: 337.5 pF Charging capacitance: 21.6 nF Maximum stored charge: 114.8 μC Maximum voltage: 340 kV Maximum energy transfer: 19.5 J
HV Capacitor	Voltage: 40 kV Capacitance: 17 μF Maximum stored energy: 13.6 kJ
Magnetic Switch	Saturation determinant: 24.5 – 26 mVs Saturation time @ 320 kV: 76 – 81 ns Saturated inductance: < 17 μH

3.2.1 Primary Setup

The high voltage and high current that allowed for the breakdown of the primary gap is supplied by a Marx generator and a high voltage capacitor, see Figure 3.2. First, the Marx generator and high voltage capacitor are both charged. The Marx generator is then triggered while the high voltage provided breaks down the primary gap. While the arc is on, the magnetic switch saturates; reducing the inductance in the system causing a decrease in voltage through the switch and an increase in current. This supplies the desired high current to the breakdown event. The primary setup involves three major components. The first, power supplies, contained all the high voltage power supply systems for the components of the primary system, and the triggering system for the primary Marx generator. The second will be the Marx generator used in breaking down the main gap. The third will be the magnetic switch used in the delivery of the high current.

3.2.1.1 Power Supplies

The primary setup had two identical high voltage power supplies. The high voltage DC power supplies are from Hipotronics and each are capable of delivering up to 50 kV DC at a maximum of 5 mA. One, set to 40 kV DC, was used to charge the Marx generator. The other was used to charge the high voltage capacitor to 10 kV.

Triggering of the high voltage Marx generator was accomplished via a solid state high voltage pulse generator. An initial pulse of ~1.2 kV was generated by the pulser and then input into a pulse transformer with a turn ratio of 1:44. The pulse generator had an

electronic trigger system which allowed it to be synchronized with the secondary Marx generator.

3.2.1.2 Marx Generator

The voltage necessary to breakdown the primary electrodes was supplied by a 320 kV Marx generator, see Figure 3.8. Housed in an aluminum casing, the 8 stage Marx generator had 5.2 nF capacitance per stage and a charging voltage of < 40 kV. Typically, the pulse width was ~150 to 200 ns and had a rise time of ~80 to 100 ns. To monitor the transient voltages a capacitive voltage-divider integrated onto the RG220 coaxial line was used, see Section 3.5. If this Marx generator is charged with a positive voltage, the output will be a negative voltage, see Figure 3.8.
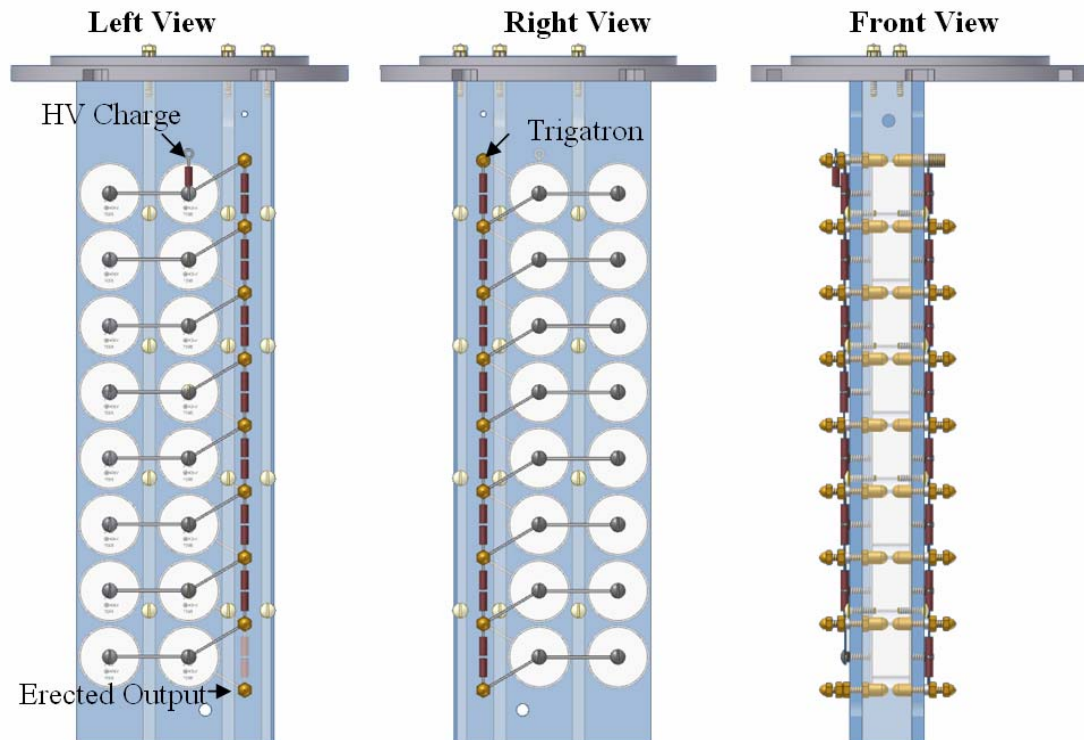
Figure 3.8: Primary setup 320 kV Marx generator design. 2.7 nF Capacitors (2 in parallel per stage), 6 kΩ per stage and 1 MΩ on HV charging.

3.2.1.3 Magnetic Switch

In the design presented above, a method of delivering a high amount of current (10-50 kA) had to be designed. The scaled current amplitudes were chosen with respect to the amplitude found in the LTGS (600 kA). It was decided that a charged high voltage capacitor could deliver the current to a formed arc via some means of a closing switch. Due to the high voltages involved in this design, the list of closing switches soon became scarce. A magnetic switch was chosen as the solution to this problem since it could be designed to handle both high voltages and currents, and still have a high lifetime [27, 28]. Using the fundamental equations for a magnetic switch, as given in equation 3.1, a basis for a design which could hold off the 320 kV pulse for the duration of the arc lifetime was formed. The formation time of an arc in SF_6 at 20 psig was taken from experimental waveforms dealing with SF_6 at these pressures [29].

a) $\quad \Delta B \cdot A \cdot N = \int_0^{t_{sat}} V(t)\, dt$

ΔB is the change in magnetic flux density $(B_r + B_s)$
A is the cross section area of core
N is the number of turns

(3.1)

b) $\quad L = \dfrac{\mu_0 \cdot \mu_r \cdot A \cdot N^2}{1}$

l is the magnetic path length
μ_r is the relative permeability of the ferromagnetic material

Setting the constants into the left side of equation 3.1 (a), results in what is called a saturation determinant. The saturation determinant used in the design was a 24.5-26 mVs with a saturated inductance of less than 17 μH. This meant that the switch could

hold off a 320 kV pulse for 76-81 ns, which was more than sufficient for arc formation. Three switches acting as one were used to lower the saturation time of the switch and the total inductance. Two AMCC1000 Metglas c-cores were used due to their high magnetic field saturation of 1.56 Teslas, see Figure 3.9. The core edges were grinded to a chamfer to reduce the field strength. To avoid breakdown issues caused by the high voltage levels, high density polyethylene was used to create bobbins for the AMCC1000 cores. Their wire wrappings consisted of 15 kV DC 12 gauge corona resistant Teflon wire (CRT 12-3) from Daburn. The outer bobbins were wrapped counterclockwise, while the center was wrapped clockwise. This ensured that the magnetic fields flowed in a continuous pattern, thus working together to saturate the cores. The bobbins were given a tapered effect on each side to decrease the points at which the electric field magnitude was at its highest. After wrapping the outer and inner bobbins with 22.5 turns of the CRT wire, the switch was submerged in transformer oil and then out-gassed over night to insure maximum voltage hold off of the oil, see Figure 3.10.
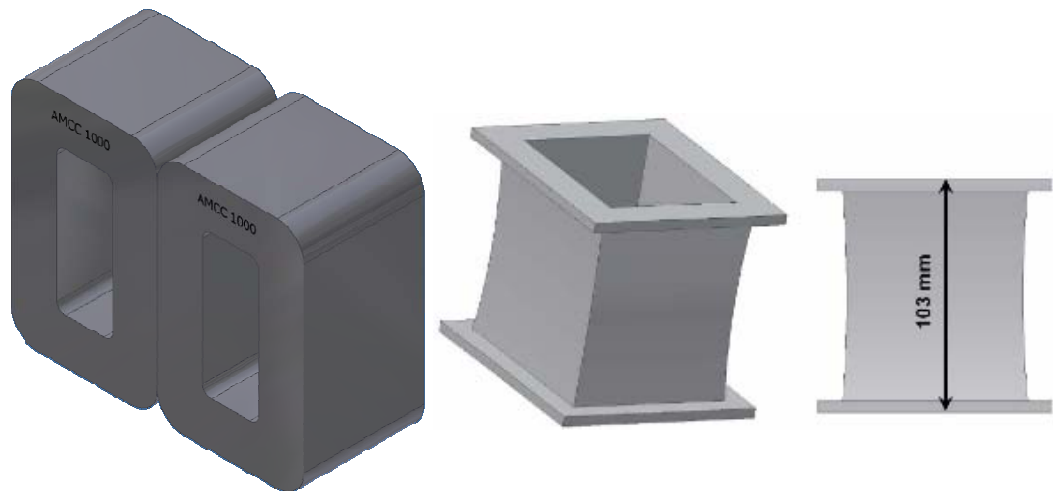
Figure 3.9: Magnetic switch core configuration and center bobbin dimension.
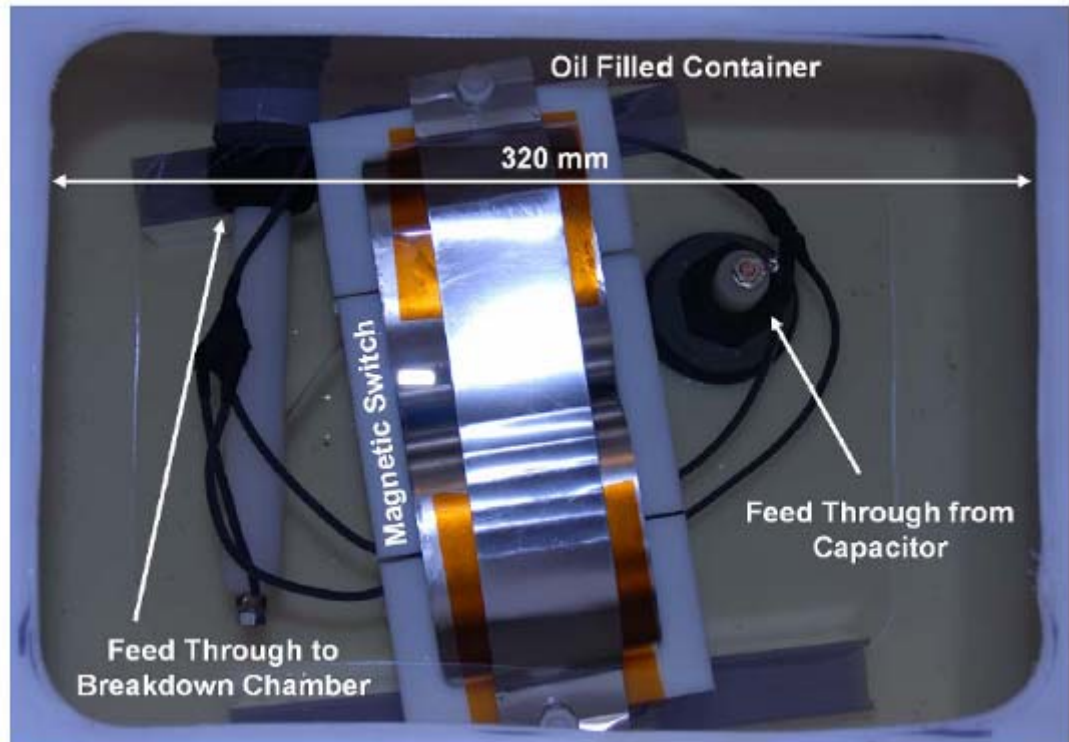
Figure 3.10: Final magnetic switch assembly in a reinforced oil vessel.

A pressurized T-style junction was developed in order to integrate the magnetic switch into the setup, see Figure 3.11. The junction was pressurized because previous experience at these high voltages had exhibited corona problems. The junction was made of clear PVC and pressurized to 20 psig with SF_6. Compression interconnects were utilized to ensure a current carrying path.
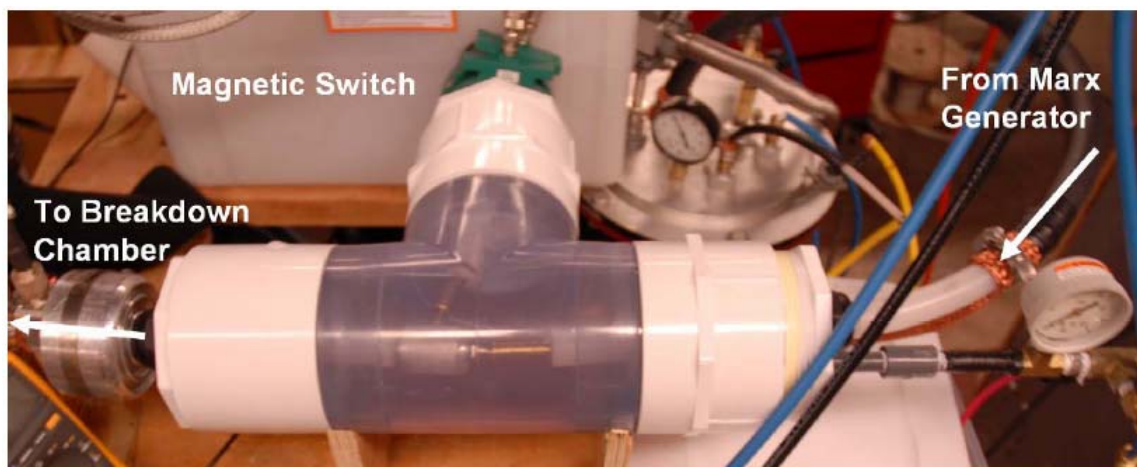
Figure 3.11: T-junction connecting magnetic switch to main chamber path, 20 psig SF_6.

3.2.2 Secondary Setup

The purpose of the secondary electrodes in the chamber is to be excited to the point of breakdown, as well as, under breakdown. To accomplish this, a second high voltage Marx generator was incorporated. The secondary surface flashover electrodes in the chamber are excited by a separate system from the primary. Hence it can be synchronized to the primary Marx generator. The secondary setup is very similar to the primary setup, except that it is consistent of only a Marx generator and high voltage power supply. Since only breakdown was required, a high current pulse was not necessary.

3.2.2.1 Power Supplies

The Marx generator used in the secondary setup is charged by high voltage DC power supply from Glassman High Voltage, Inc (model # PS/WR125P2.0-11) and is capable of providing a DC voltage of up to 125 kV at a maximum current of 2 mA. A

high voltage resistor is put between the output of the power supply and the Marx generator to limit current and to help protect against transients.

The triggering of the Marx generator is performed via a 1.2 kV solid state pulse generator identical to the one described in section 3.2.1.1. The pulse transformer used for this design has a ratio of 1:37. Both the primary and secondary setup pulse transformers are wound on bobbins on AMCC100 Metglas cores. The primary windings consist of 0.1" diameter, 20 AWG wire with FEP insulation from Reynolds Industries coated wire. The secondary is a quadruple build magnet wire 22 AWG from Magnetic Wire Co.

3.2.2.2 Marx Generator

The Marx generator used in exciting the secondary setup surface flashover electrodes is essentially identical to the Marx generator used in the primary setup. The physical arrangement is similar except that each stage has half the capacitance of the primary Marx generator stages, see Table 3.1. Another varying feature is that this Marx generator is triggered by a triple electrode configuration. Trigger differences between the two Marx generators, pressure differences and closeness to the Marx generator self-break point all cause variances in the time to Marx generator erection.

3.3 Volume Breakdown UV Source

For the experiments involving the testing of an applied UV source on a surface flashover event, both breakdown gaps were used. The primary setup was put into the volume breakdown configuration and a surface was placed underneath the electrodes on the secondary setup. The high current volume arcs produced a larger contribution in the

UV region ($\leq$320 nm) than previous low current experiments. The synchronization of the two Marx generators was not completed at the time of thesis publication. Results will be presented in a future report to Sandia.

3.4 Environmental Control

Since the voltage levels of the system were greater than the breakdown strength of air, the gas sulphur hexafluoride (SF_6) was chosen to be used as high voltage insulation. The magnetic switch T-junction and both Marx generators where filled with SF_6 (20/20/9 psig respectively) as a high voltage insulator. The testing chamber required SF_6 for experimenting in high pressure environments was equipped with gas lines, pressure release valves and, as a safety precaution, an automatic over pressure release valve set to 50 psig, see Figure 3.12.

Since the chamber had an operating pressure ranging from 10^{-4} torr to 50 psig (2586 torr), a vacuum pressure system was incorporated. A Varian roughing pump (model # PTS03001UNIV, serial # LPE80462) was used to evacuate the chamber. Once a set point was reached, the Varian turbo-V550 MacroTorr pump (model 969-9050, serial # 75046) was activated and pulled the chamber to the 10^{-4} torr range. The vacuum pressures where recorded by three separate measurement devices. An MKS 999-Quattro ion gauge measured pressures low 10^{-4} torr pressures while two MKS BARATRON gauges recorded 0-100 torr and 100-1000 torr respectively.
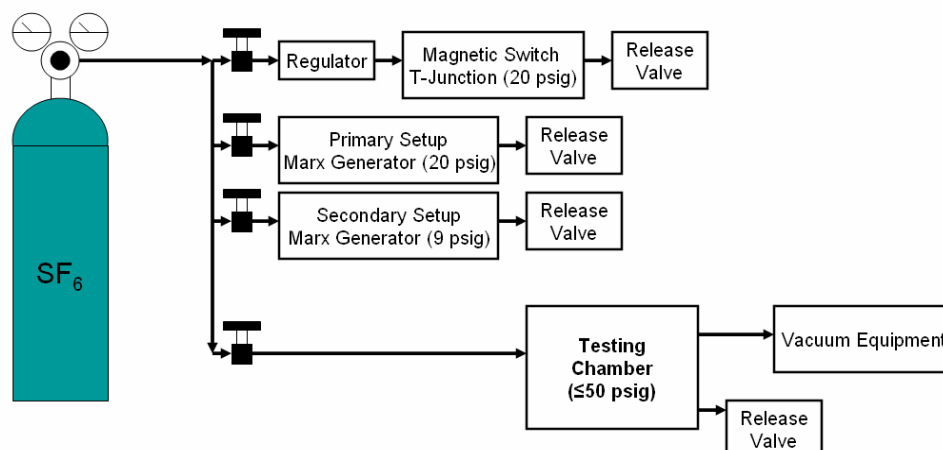
Figure 3.12: Gas flow configuration for experimental setup.

3.5 Diagnostic Setup

Since the breakdown processes occur in the nanosecond regime, instrumentation with a high temporal resolution is required. In addition to a high temporal resolution, consideration had to be placed on the physical placement of the measurement devices in order to minimize the signal reflections and distortions. The signals used for characterizing both the surface flashover event and the volume breakdown are the current and voltage waveforms. Three different styles of probes where chosen and used to obtain these signals.

3.5.1 Current Sensors

Originally the current measurements were obtained from a traveling wave current sensor incorporated into the RG220 transmission line entering the testing chamber. When dealing with signals in the nanosecond regime, the current sensor produced minimal signal distortion and proved suitable for the measuring of the current signals produced at

both low current breakdown events with a resolution of 0.1 V/A [30]. However, with the incorporation of the magnetic switch and high voltage capacitor, the time regime changed. Since the magnetic switch had a saturation time in the microseconds, due to the lower voltages being applied to it, the traveling current sensor was deemed unsuitable for use. Thus, two commercially available Pearson coils (Model: 101, 100 ns rise time, 0.01 V/A; Model: 4418, 200 ns rise time, 0.001 V/A) were incorporated into the setup to monitor the current. While one was used to record the current, the other was used to trigger the pulse generator for the ICCD camera and spectrograph. Both sensors were placed at the exit of the transformer oil filled magnetic switch housing that entered the T-junction, see Figure 3.11.

3.5.2 Voltage Measurements

Voltage waveforms are obtained by a capacitive voltage divider embedded in to the RG220 transmission line at the entrance of the testing chamber, see Figure 3.1. The reason for choosing the capacitive voltage divider is that they are easily incorporated into the coaxial transmission line and provide low nanosecond rise-times. Capacitor, C_1, of the divider consists of a piece of copper tape and the inner conductor with the transmission line insulation as the dielectric. C_2 of the divider includes the copper tape and the outer conductor with a piece of Kapton tape placed in between. Figure 3.13 is a simple cross-sectional diagram of a capacitive voltage divider. An aluminum shell with a built in type N connector, for signal transmission, is placed over the divider with a center pin that extends through the Kapton to make contact with the copper tape. The particular divider utilized for the surface flashover experiments has a sensitivity of 259 mV/kV and

a rise time better than 1 ns. For a more detailed explanation of operation, see reference 31.
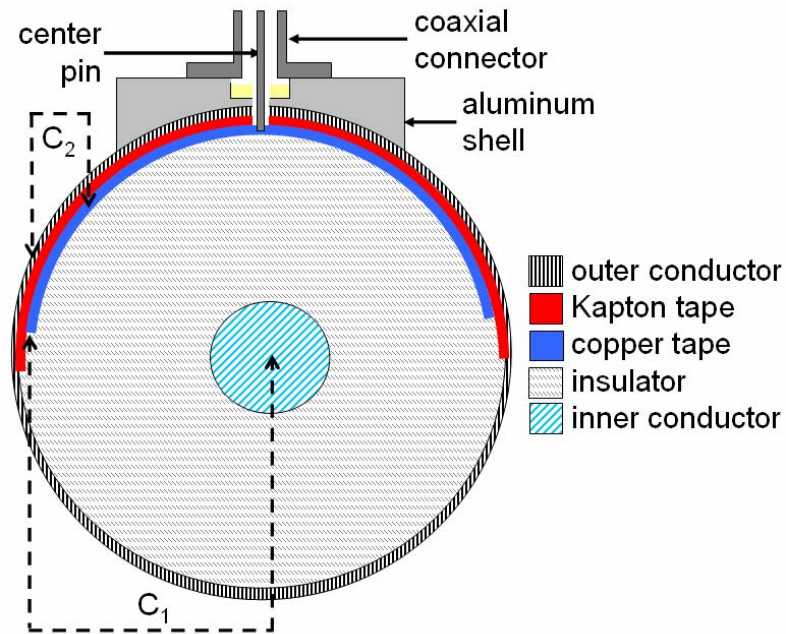
Figure 3.13: Cross-sectional rendering of a capacitive voltage divider.

As for the high voltage DC used in charging the capacitor, primary Marx generator and secondary Marx generator, high voltage DC probes by Fluke where used. Each Fluke probe (model # 80K-40), rated up to 40 kV, has a sensitivity of 1000:1 and required an individual multi-meter.

3.5.3 Breakdown Event Imaging

An Andor Technology Intensified CCD (charge couple device) DH-734 GenIII camera with nanosecond temporal resolution is used to capture the flashover images. Intensified CCD (ICCD) cameras are either lens coupled or fiber optically coupled to the

microchannel plate shutter. This allows for the nanosecond gating times required to capture surface flashover events. The camera is fitted with a zoom lens and is mounted on a fully adjustable camera stand. The camera is typically positioned either directly in front of the chamber viewing through the quartz window or 45 degrees from normal to the breakdown event looking through the Lexan lid. Since the fiber optic lines are positioned directly above the breakdown event within the chamber, the camera had to be given the slight angled offset. The camera is either focused on the dielectric gap space between the electrodes or the volume between the electrodes when used for volume breakdown imaging. The output of the .01 V/A Pearson coil current senor is used to trigger a trigger-delay generator that sends a TTL gate pulse to a second trigger-delay generator which then sends a 14 V pulse to both the ICCD camera and the spectrograph, see Figure 3.14. An optical gate time of 500 ns was utilized for both breakdown experiments. Along with the ICCD camera, a Nikon D200 camera was used to take time integrated photos of the breakdown events. With the high current breakdown events, the intensity necessitated a neutral density filter on both the ICCD camera and the Nikon camera. Usually a neutral density filter (ND) of 4 was taped to the Nikon and a ND of 4 or 5 was placed in front of the ICCD camera.
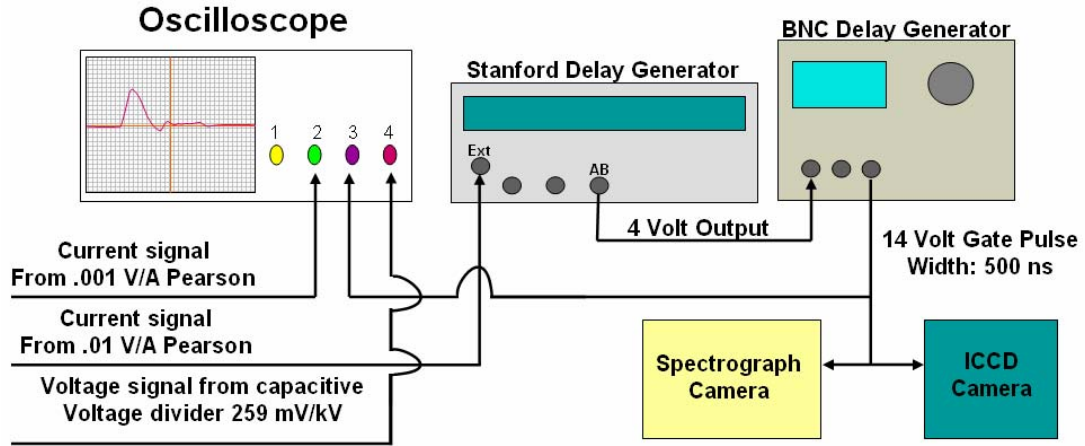
Figure 3.14: Triggering setup used for testing.

3.5.4 Fiber Optics

Since imaging of the discharge provides just a single picture of the developing discharge, an approach utilizing fiber optics was chosen to capture spatially resolved light emissions from the discharge gap, see Figure 3.15, 3.16. This spatially resolved light is used to gain a temporal picture of the arc formation in the gap or to gather spatially resolved spectra. A special system is constructed to gather the light from the breakdown. For a given distance, the expected light transmission can be calculated from the cross section using Beer-Lambert Law,

$$T = I/I_o * \exp(-\sigma * n * d) \tag{3.2}$$

with the transmission T, intensity of the incident/transmitted light I_o or I, respectively, absorption cross section σ [cm^2], n molecule density (2.5 x 10^{19} cm^{-3} for STP), and d distance [cm]. The resulting transmission for the switch conditions, $d = 2.75$ inches, n corresponding to 40 psig of gas, reveals that light above 160 nm is easily transmitted in an SF$_6$ atmosphere, while this limit is roughly 180 nm for molecular oxygen, see Figure 3.13.

51
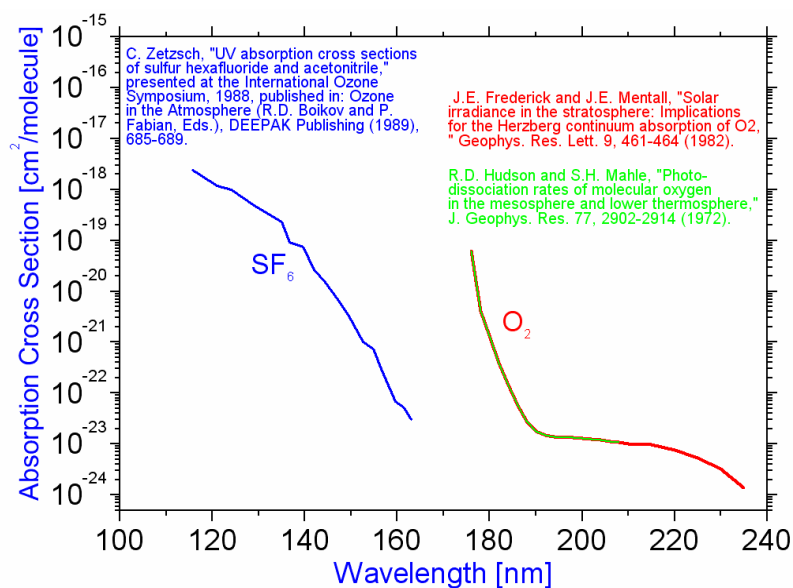
Figure 3.15: Absorption cross sections for molecular oxygen and sulfur hexafluoride [2].
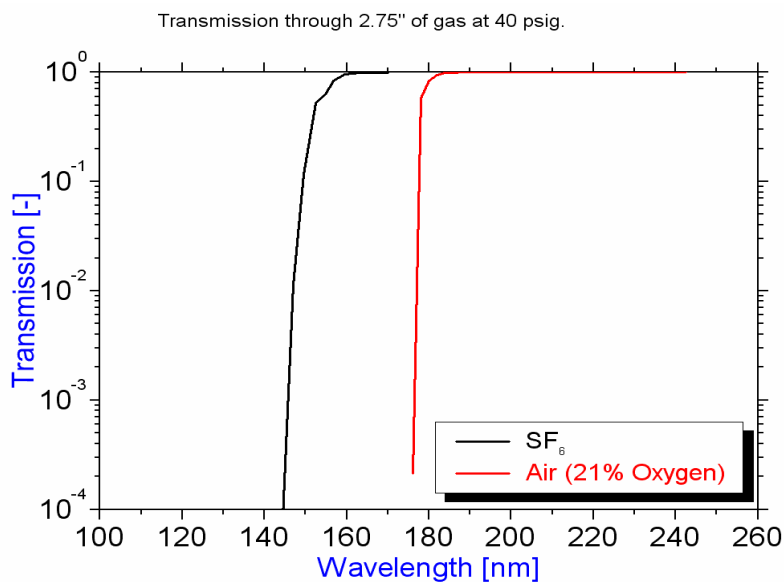
Figure 3.16: Light transmission for molecular oxygen and SF_6 through 2.75 inches of gas at a pressure of 40 psig [2].

The light gathering setup has a specially designed lens holder that supports three cylindrical rod lenses shown in Figure 3.17, 3.18. These rod lenses are made of Suprasil®; a highly pure, synthetically-fused silica material that does not attenuate light

above 175nm and can be purchased from J. R. Cumberland Inc. The lenses are 3.0mm in diameter and 5.0mm long. They are mounted parallel to one another and are 4.95 mm apart center to center.
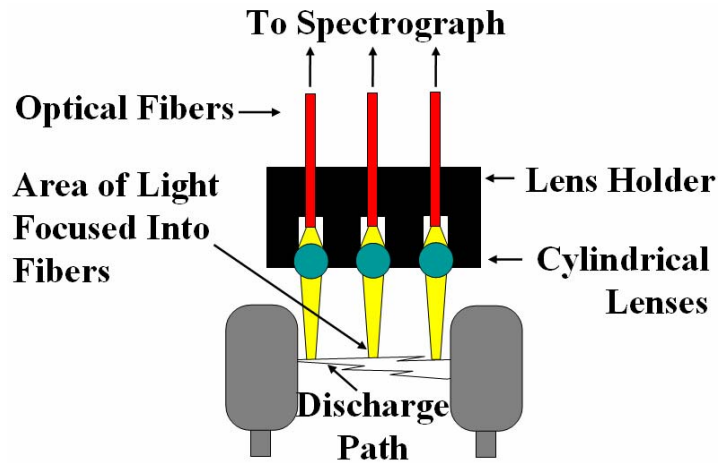
Figure 3.17: Fiber optics setup for spatially resolving light emission in the volume gap
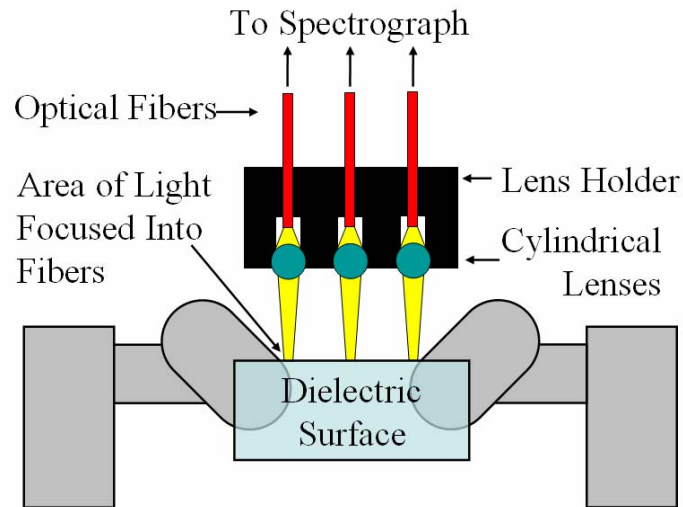
Figure 3.18: Fiber optics setup for spatially resolving light emission in the flashover gap

This places the field of focus of the outside lenses just in front of the two electrodes. The center lens is focused between the electrodes. Behind each lens is a quartz fiber optic cable into which the lens focuses any collected light. The optical fibers used are Superguide G fibers from Fiberguide industries. The fibers have a 200 μm core diameter and a 220 μm cladding including the diameter. The fibers contain a high hydroxyl ion content which provides high transmission efficiency from UV through visible and into near IR. The fibers are fed out of the removable, outer conductor through a small hole that connects to a series of feed-throughs located on a specially designed leak-proof flange on the side of the test chamber. Connected to the outside of the feed-throughs is a spectrograph. The entire lens assembly is held in place above the gap by a sliding Lexan mounting bracket attached to an aluminum support base, see Figure 3.19.
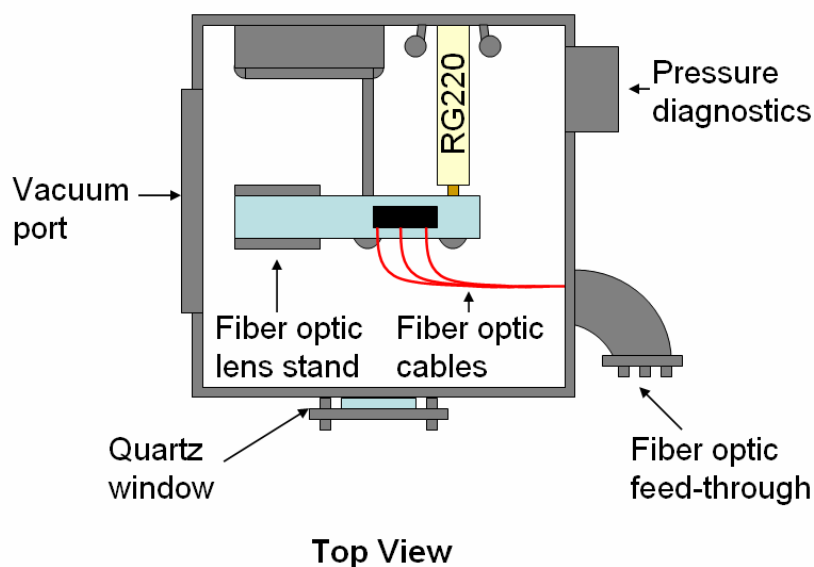
Figure 3.19: Top view of fiber optic lens layout.

3.5.4.1 Spectrograph

In order to further investigate the processes contributing to the flashover, a spectrograph is utilized to analyze the emissions from the arc. The spectrograph used is an Oriel MS 257 ¼ meter imaging spectrograph. It is equipped with a 4 grating turret and automatic grating switching. The MS 257 is a multi-track or imaging spectrograph. While normal spectrographs are designed for spectral (horizontal) resolution at the expense of vertical resolution, the MS 257 has specially shaped mirrors designed to allow multiple vertical points to be diffracted at one time as illustrated in Figure 3.20 and Figure 3.21. Because the F-number of the fiber optic cables, which is 1.67 (much smaller than the 3.9 F-number of the spectrograph), an F-number corrector is attached to the input of the spectrograph. The F-number corrector also holds the output of the three optical fibers in place.
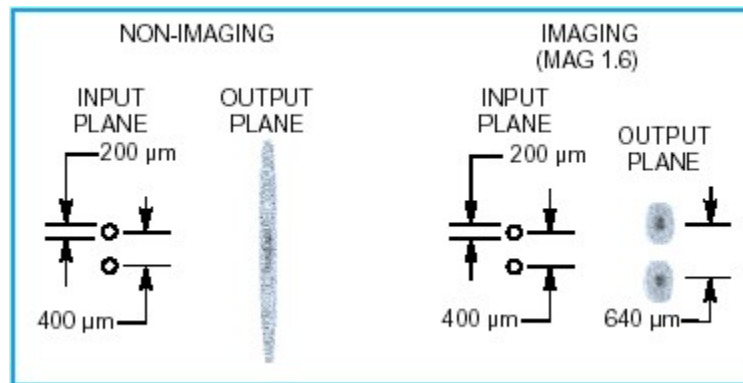
Figure 3.20: Demonstration of difference in imaging and non-imaging spectrographs, imaging spectrographs have specially designed mirrors to maintain vertical resolution
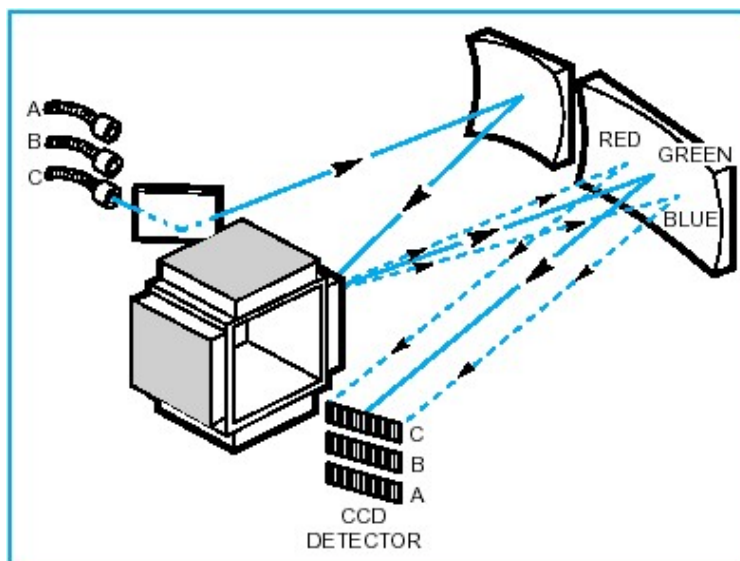
Figure 3.21: Schematic of multi-track spectrograph operation

The second ICCD camera is mounted to the output of the spectrograph. The spectrum collected is saved as an intensity map for later analysis [32].

3.6 Data Manipulation

The data collected by the oscilloscopes, plus the spectrograph, must each be corrected to account for the variances within the test setup. In the case of the waveforms collected by the oscilloscope, each had to be shifted to account for the differences in lengths found in the coaxial lines. Since 20 dB attenuators were used for both the current and voltage pulses, the amplitudes had to have the attenuation factors accounted for. Each row created by the individual fiber optic lines (20 pixels high) had to be converted into a usable form of data (nm). In order to identify the peaks, the individual rows of pixels were integrated and scaled to show the relative peak intensities. This integration is done by a script program written in Andor MCD. The rest of the conversions and all of the graphs used in this paper are done using PlotIt.

3.7 Electrode Design

Since the goal of the design was to mimic the breakdown occurring within the LTGS at Sandia National Laboratories, the electrodes used had to resemble the electrodes in the switch, see Figure 3.22. Since the volume breakdown was occurring on the outer edge of the backbone electrodes used in the rimfire switch, the volume breakdown electrodes were designed with a similar geometry. The surface flashover experiments used a geometry that was employed in previous surface flashover experiments at Texas Tech University. Finally, the electrodes on the secondary setup which also hold the UV test surface in place will be discussed.
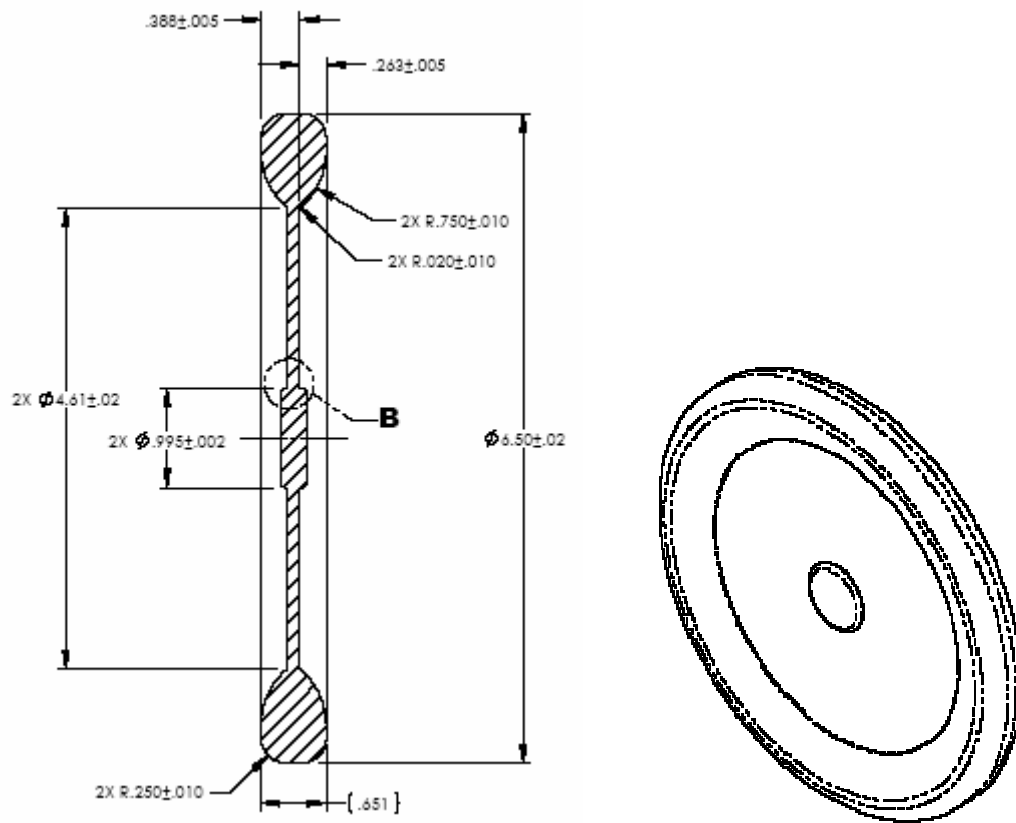
Figure 3.22: Ring electrode geometry in the LTGS at Sandia National Laboratories [2].

3.7.1 Primary Setup Surface Flashover Design

The angled electrode design for the surface flashover and surface erosion tests came from an earlier design which was used in arc formation tests, see Figure 3.24. The tests used grooved surface dielectric samples which tested whether the arc was more prone to follow the surface or the electric field lines, see Figure 3.23. If the arc would follow the lines parallel to the surface and the breakdown over the groove, it adhered to the electric field lines. The cut groove in the surface increased the distance anode to cathode. If the arc followed the surface, it would take the longer path and breakdown in the groove.
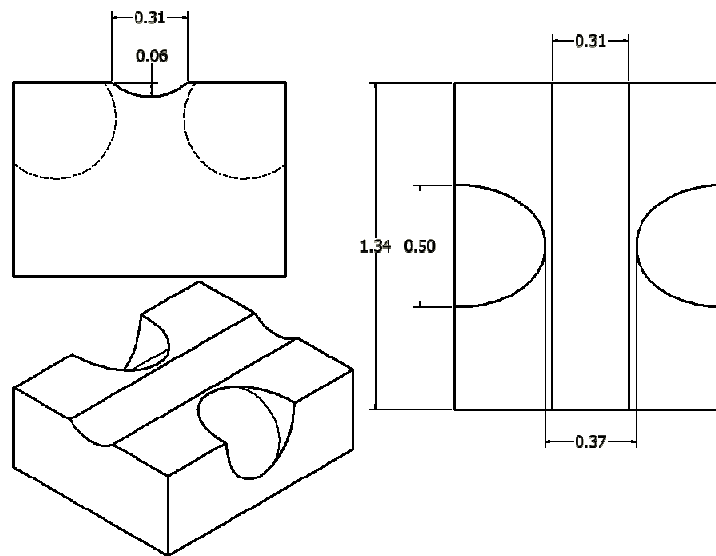
Figure 3.23: Dielectric sample geometry and dimensions used for testing.
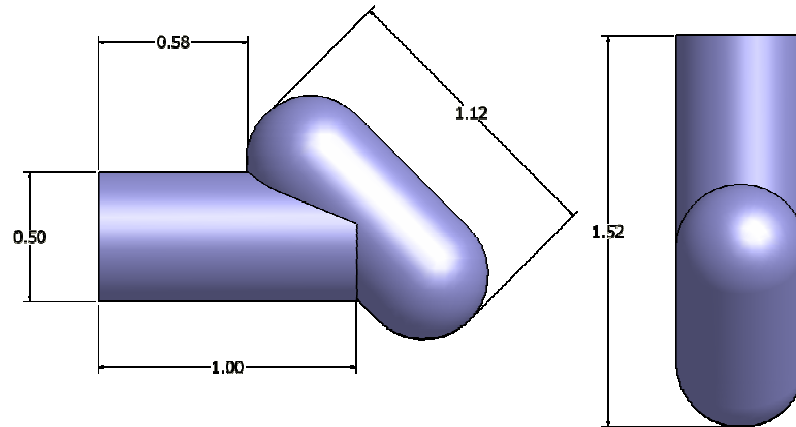
Figure 3.24: Drawing of angled electrodes used for surface flashover/erosion experiments.

The electrode design allowed for the creation of a triple point junction (electrode/dielectric/gas), a grasp of the electrode and strong electric field components normal to the dielectric surface, see Figure 3.25.
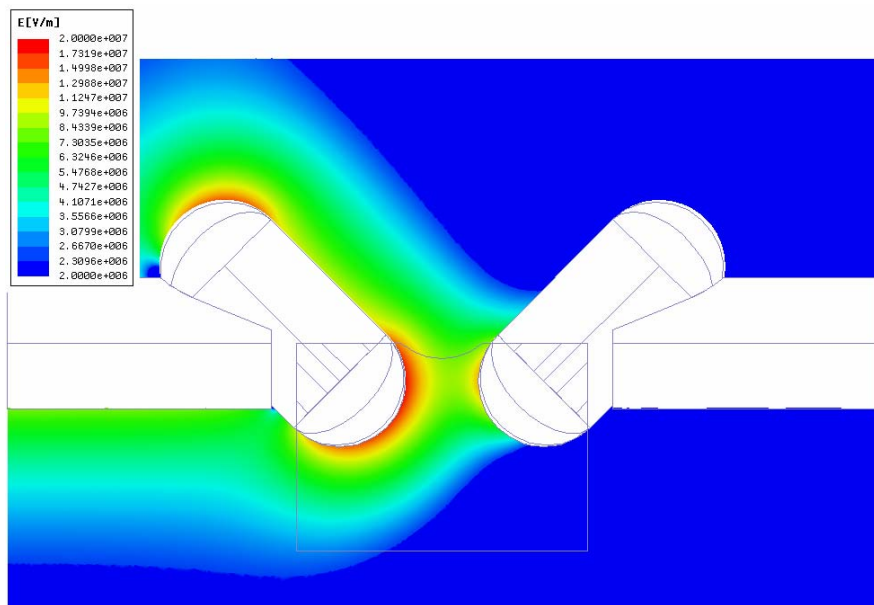
Figure 3.25: Maxwell 3D simulation of electric field magnitude for the angled electrode geometry in a cut plane normal to the dielectric surface with 72 kV applied.

3.7.2 Primary Setup Volume Breakdown Design

As explained above, the breakdown environment of the test chamber was to mimic that found in the rimfire switch. As such, the volume breakdown electrode geometry came from the outer edge geometry of the backbone electrodes found in the Z20 rimfire switch, see Figure 3.26, 3.22. Slight variations in machining created some minor distinctions in dimensions.
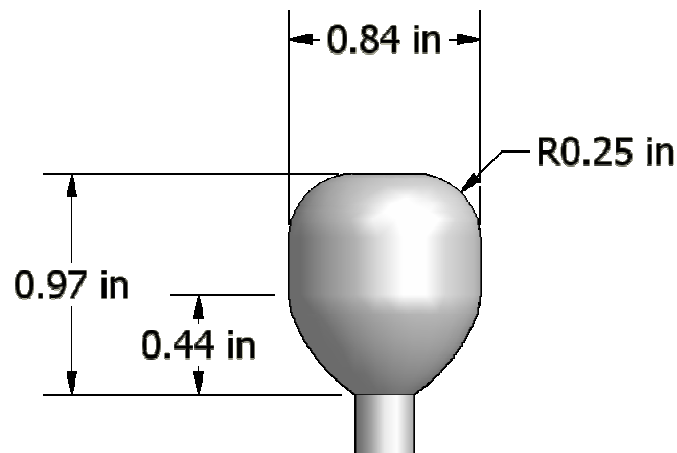
Figure 3.26: Electrodes used for volume breakdown in the high pressure chamber. The electrodes are designed to mimic outside edge of the "vertebrae" in the z20 rimfire switch.

3.7.3 Secondary Setup Surface Flashover Design

The design for these electrodes had to be one that allowed for a solid connection to a flat surface and produce strong field components parallel to the surface. Since the goal of this setup was to create an electric field on the surface, care was taken to ensure that the breakdown region was from triple-point to triple-point of each electrode. From previous experiments performed at Texas Tech University, an electrode design was chosen which ensured a triple point where the electrode met the dielectric surface, but not

any other regions under the electrode, see Figure 3.3. A method of compressing the dielectric surface with the electrodes was installed in the design. For positioning, a sliding stand was made, see Figure 3.27. It should be noted, that although it is not visible in Figure 3.27, half of each electrode was then cut in half with a tapered effect, see Figure 3.3.
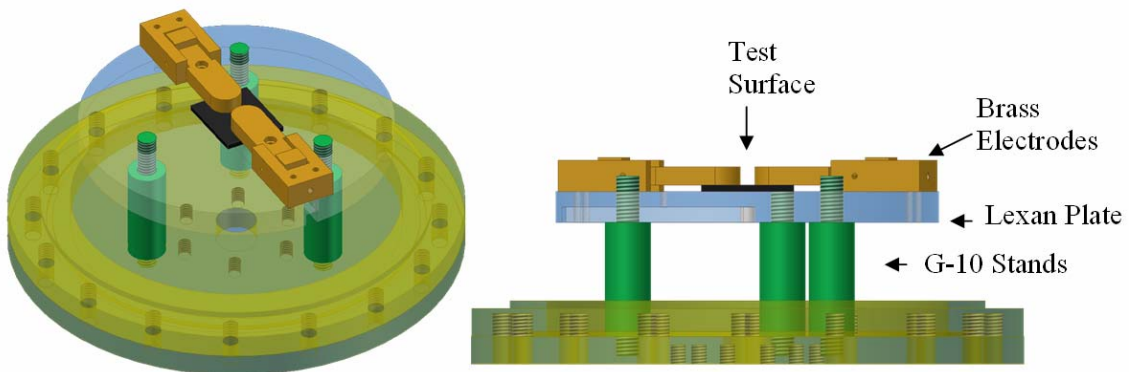
Figure 3.27: Secondary setup electrode configuration.

3.8 Procedure

Most of the components used in both modes of the primary setup remain the same except when conducting experiments in a low current fashion. When a low current mode (≤ 2 kA) is desired, the magnetic switch and capacitor are grounded. This allows only the Marx generator to deliver the current. The secondary has only one mode, the low current mode. The oscilloscopes used to collect the data from the voltage and current sensors, trigger-delay generators and spectrograph remain the same for high and low current tests.

3.8.1 Primary Setup Volume Breakdown Mode

As mentioned above, the two types of breakdown are either the low current or high current (>2 kA) configurations. To initiate the volume breakdown mode, first the volume breakdown electrodes are cleaned with methanol and then again with cyclohexane to ensure a clean surface. The electrodes are available in both brass and stainless steel. For the experiments discussed in this paper only the stainless steel electrodes were used. Once installed on the electrode connections inside the chamber, the fiber optic stand was aligned over the gap. Care is taken to ensure that the fiber optic lines are equally spaced throughout the gap.

After positioning the fibers, the chamber lid was sealed and the vacuum components were activated. While the system pressure was dropping to vacuum, the ICCD camera was typically aligned above the breakdown event and the Nikon camera was given a side view via the quartz window at the front of the chamber, see Figure 3.28. Literature has shown that small amounts of Nitrogen dominate the spectra of breakdowns in SF_6, so the chamber was evacuated during each test. Once the chamber reached ~ $5x10^{-5}$ torr, the gate valves were sealed and the chamber was back filled with SF_6 up to the desired testing pressure. In this paper testing pressure is assumed to be 20 psig unless otherwise stated. The next step after ensuring the chamber was at the desired pressure is to pressurize the T-junction and primary Marx generator to 20 psig and 19 psig of SF_6 accordingly. Once pressurized, the system was ready to be charged. The Marx generator was charged to 40 – 41 kV, and when the high current mode was desired, the capacitor was charged to 10 kV. Making sure that the oscilloscope was armed, plus the trigger-delays set accordingly, the solid state pulse generator was armed. When ready to fire, the

manual trigger on the solid state pulse generator was pushed. Once fired, the system

would recharge itself and be ready to fire again if need with a matter of minutes. An

overall system layout can be seen in Figure 3.29.
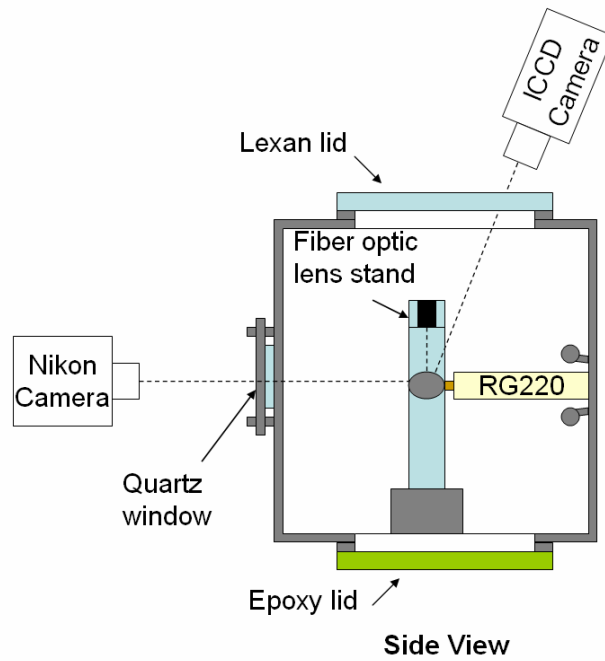
Figure 3.28: Side view of camera positions with respect to breakdown event.
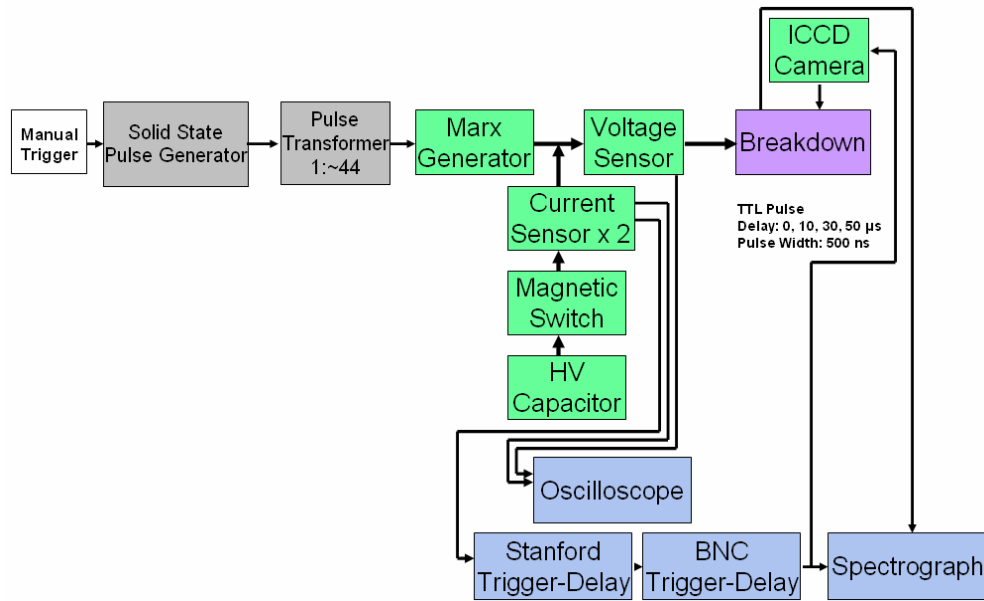
Figure 3.29: Overall primary setup layout. Gas and charge lines are excluded.

3.8.2 Primary Setup Dielectric Surface Flashover Mode

The dielectric surface flashover mode on the primary setup was essentially similar to the volume breakdown mode. Rather than the volume breakdown electrodes, the angled surface flashover electrodes were used along with a dielectric sample of your choice.

The electrodes were cleaned with the same method as the volume breakdown electrodes. After the installation of the electrodes, the dielectric sample surface was cleaned using cyclohexane and a chemical wipe cloth. The electrodes were then inserted into the slots in the sample and great care was taken in making sure the sample and electrode made a tight seal. This helped avoid any air gaps between the electrode and dielectric sample which could lead to field enhancements. Henceforth, the procedure is the same as that listed in the volume breakdown section (3.8.1).

3.8.3 Secondary Setup Surface Flashover

Since the electrodes in the secondary setup were essentially fixed, the procedure started by cleaning the electrodes with methanol followed by cyclohexane. After this, the 0.1 in thick Lexan surfaces had their protective sticker removed. The surface was then cleaned with cyclohexane to remove any residual residue. After positioning the surface underneath the anode and cathode electrodes, the high voltage connections in the chamber were checked. The process from here on is the same listed in the volume breakdown section (3.8.1); except that along with the primary setup, the secondary Marx generator was charged as well. The charging voltage depended on whether the test required creating an electric field capable of breaking down along the surface, or a field which lies just under the critical field intensity. Once the voltage is applied, the secondary solid state pulse generator is armed along with the primary one. At this point, both pulse generators were setup to be triggered off of the same source. Typically a BNC model 510 trigger-delay generator was used and set to 14 volts output.
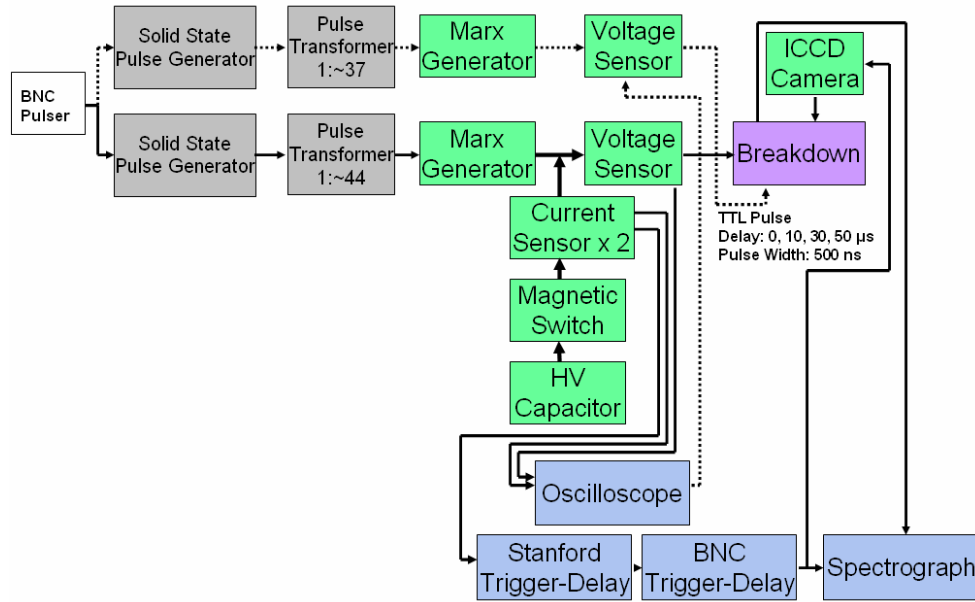
Figure 3.30: Overall primary and secondary setups in dual firing. Gas and charging lines excluded.

CHAPTER 4

ELECTRICAL BREAKDOWN RESULTS

Electrical breakdown experiments where conducted at various pressure and current conditions. The results presented in this paper deals with the higher pressure results, but at times will compare to previous low pressure results only to emphasize the differences. In the following sections, the results for volume breakdown at various current amplitudes and pressures will be presented. An explanation of the optical emission spectra gathered from the breakdown event will be presented as well. In the latter, the results for surface flashover events at varying currents and pressures will also be presented. The results for varying dielectric materials have been tested and cataloged and will be presented.

4.1 Reference Waveforms

Typically, the waveforms collected were the camera gate, current and voltage. These waveforms were saved in a comma delimited file format which allowed for importing into graphing software such as PlotIt. Small deviations occurred from time to time in voltage amplitude, time scale offsets due to triggering and coaxial line lengths, and current amplitude. The current amplitude deviations occurred mainly with surface flashover due to fluctuations of the arc resistance. A representative set of waveforms can be seen in Figure 4.1.
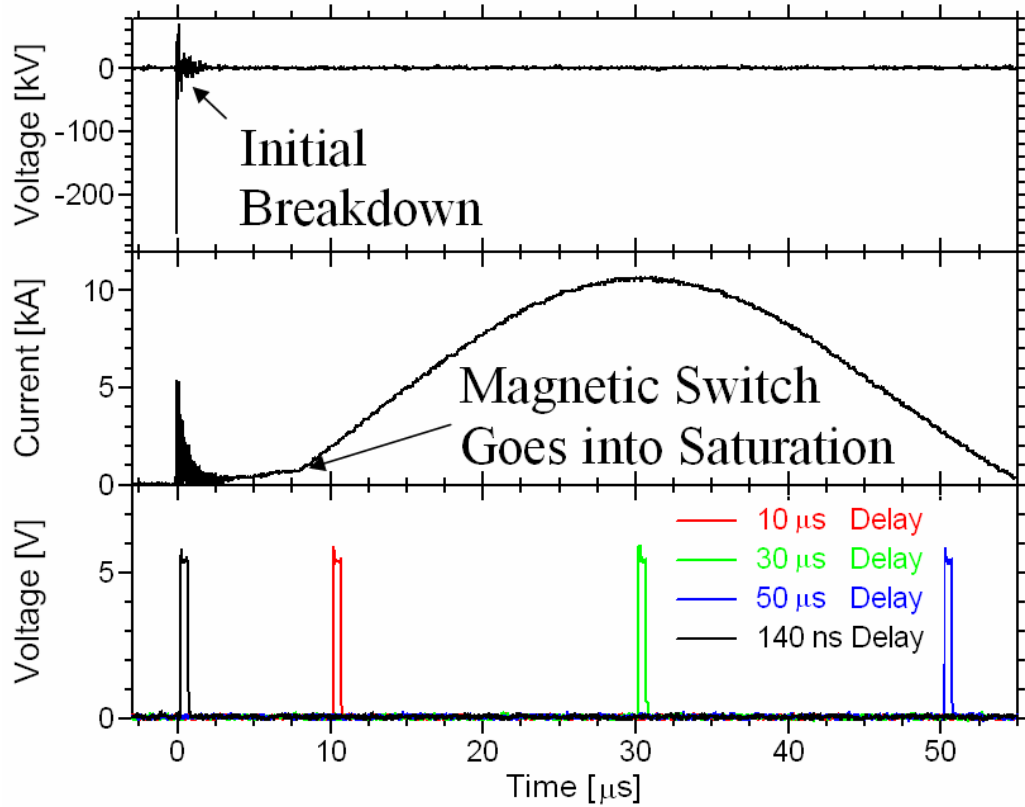
Figure 4.1: Representative set of waveforms typical of both surface flashover and volume breakdown.

The camera gate is a TTL gate pulse with a width that was set to 500 ns. After experimenting with the camera gate delay times, four times were chosen that gave a good representation of the current distribution. Each of the four current amplitudes resulted in a distinctly different spectrum and ICCD image. Although the initial breakdown of the gap occurs within the early ~ 200 ns regime, the magnetic switch does not go into saturation until ~ 9 μs. When the saturation point is reached by the switch, the current from the HV capacitor is then allowed to enter the formed plasma channel. It should be noted that previous data shows that the oscillations occurring in the current last for approximately 1.2 ms. This means that the arc is staying active for 1.2 ms. The typical voltage waveform is characterized by a sharp rise in amplitude as the voltage pulse is applied to the gap;

followed by a distinct drop in voltage as the breakdown event occurs. The bipolar appearance of the voltage pulse is due to the droop of the fast capacitive voltage divider incorporated in the transmission line, Figure C.6. It was confirmed with a voltage probe of slower rise time, but much larger droop time, that the gap voltage is constant after the initial rise or charging until breakdown occurs. The collapse of the gap voltage due to electrical breakdown is also indicated by the simultaneous rise in current. This also occurs during the initial breakdown event in Figure 4.1, but due to the time scales cannot be seen.

4.2 Volume Breakdown

For the volume breakdown experiments, the primary setup was used with stainless steel electrodes and a gap spacing of 9.25 mm. A detailed explanation of the electrodes and operating procedure when in volume breakdown mode can be found in section 3.8.1. As mentioned previously, the spacing between the electrodes is identical to that found between the backbone electrodes of the LTGS. Spectroscopic descriptions of the various environments and amperages, and corresponding image analysis of the arc formations are shown below. Also, an investigation into the solid by-products of electrical breakdown in SF_6 will be discussed.

4.2.1 Volume Breakdown Images

The results of electrical breakdown in SF_6 at various pressures were recorded. The influence of the various current intensities was also investigated. As far as the imaging was concerned, the difference was the intensity of the arc. As the delay time of the

camera gate shifted from lower to higher currents, a larger attenuation was required from the neutral density filters. Typically a neutral density filter of 5 was required in the 10 kA range. To better show the effect of the higher current on the breakdown, a series of breakdown events from lower to higher pressures will be shown. Keep in mind that at the lower pressures, sub 0 psig, the influence of gases, such as Nitrogen due to a small leak, can be noticed by the variation of arc color. Nitrogen for example is known to have a pinkish color when electrically broken down, see Figure 4.2.
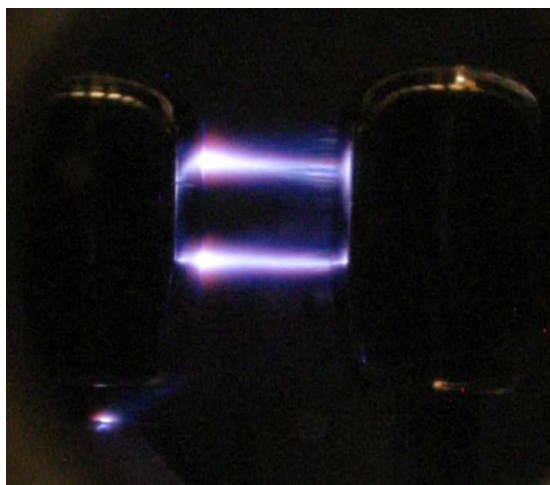
Figure 4.2: Time integrated image of volume breakdown (~ 1 kA) between two stainless steel electrodes in SF_6 at 10 torr. ND = 0. Charged electrode is on the left.
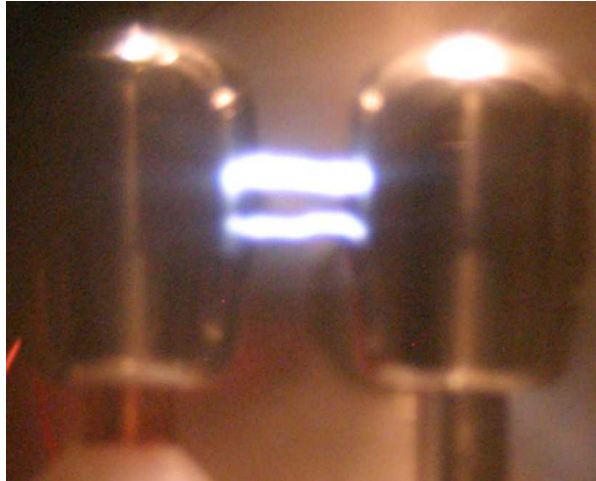
Figure 4.3: Time integrated image of volume breakdown (~ 2 kA) between two stainless steel electrodes in SF_6 at 20 psig. ND = 2. Charged electrode is on the left.

Figure 4.4: Time integrated image of volume breakdown (~ 10.2 kA) between two stainless steel electrodes in SF_6 at 20 psig. ND = 4. Charged electrode is on the left.

A noticeable difference in the arc behavior becomes apparent from Figure 4.3 to Figure 4.4 as the current amplitude is increased. The plasma length and width develop as large as the diameter of the electrodes as seen in Figure 4.5.

71
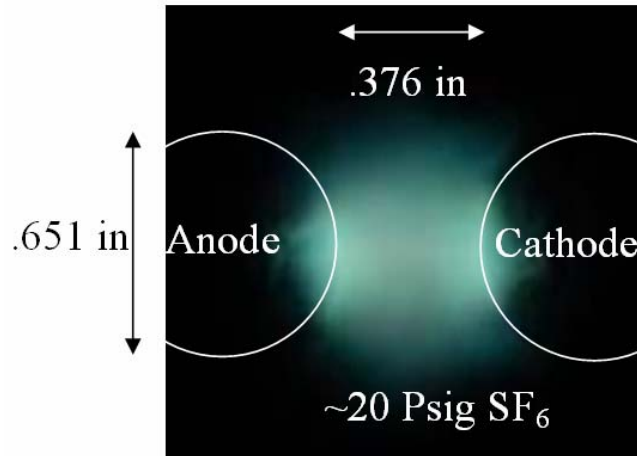
Figure 4.5: Front view of time integrated image of volume breakdown ($\sim$ 10.2 kA) between two stainless steel electrodes in SF_6 at 20 psig. ND = 4. Charged electrode is on the left.

At first glance, the breakdown at 20 psig of SF_6 seems to be a wide and large arc.

Yet when viewed with an ICCD camera, the main arc can be seen within the plasma

breakdown. In Figure 4.6, it should be pointed out that the inner arc is still more

prominent that an arc formed at 20 psig of SF_6 with a lower current.
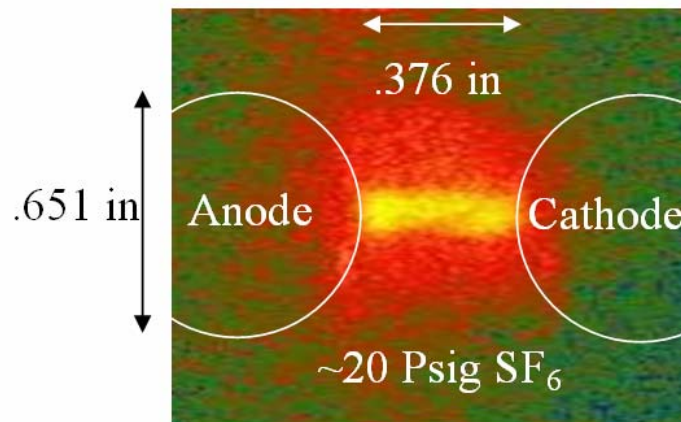
Figure 4.6: Front view of ICCD image of volume breakdown ($\sim$ 10.2 kA) between two stainless steel electrodes in SF_6 at 20 psig. ND = 4. Charged electrode is on the left.
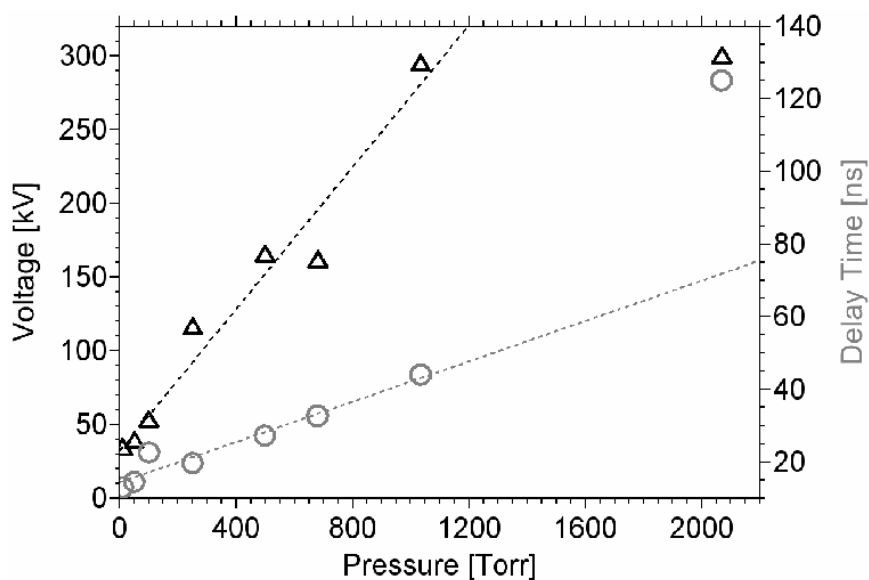
Figure 4.7: Volume breakdown voltage and delay time of a 9.52 mm gap in SF_6 at increasing pressures with ~ 50 ns risetime voltage pulse. Delay time is defined as the FWHM from the rise of the voltage pulse to the drop due to breakdown [41].

In Figure 4.7, the breakdown voltages by corresponding pressure and the average delay time per pressure can be seen. The pressures listed are from 10 Torr to 2069 Torr. Figure 4.7 shows that as the hold-off voltage increases, the corresponding delay time increases. This is expected, and can be attributed to increased electron energy loss processes, such as inelastic collisions, at higher pressures due to the decrease in mean free path. It should be noted that the values in Figure 4.7 correspond to a low current (≤ 2 kA) volume breakdown event and that in the pressure regime below 20 psig (1034 Torr), the breakdowns occur on the rising edge of the incident pulse.

4.2.2 Volume Breakdown Spectroscopy Analysis

The optical emissions of the breakdown event had been gathered and analyzed for various pressures and current amplitudes. An interesting observation between the spectra

gathered along the discharge path at low currents is that they are almost identical. For a look at the spectra gathered from low pressure breakdowns, see Appendix B. The spectra presented in this section were gathered by the center fiber optic lens. The fiber optics close to the electrodes showed similar spectroscopic results; except they showed iron lines from the steel electrodes.

The identification of prominent UV emission from volume breakdowns in SF_6 at high pressures was crucial. Previous experiments at Texas Tech University have shown that UV below 320 nm largely affects the behavior of a surface flashover event [1]. Since photoelectric emission from the surface increases with an increased photon energy, or decreased wavelength [34, 35], it is obvious that a higher UV output from the volume spark will liberate an increased number of photoelectrons from the LTGS PMMA envelope surface. As seen in the Figure 4.8 and 4.10, a larger contribution of UV in the < 320 nm region of the spectra is apparent and as such reaffirms the initial hypothesis of UV influencing the initiation of surface flashover in the LTGS envelope. The broad features in the spectra at 20 psig are compared to black body radiation in Figure 4.8, using equation 4.1. The spectral sensitivity of the collection apparatus drops off significantly at wavelengths approaching 200 nm, Figure 4.9, and is perhaps responsible for the drop in the spectra around 220 nm. The other possibility for the drop around 220 nm is self absorption.
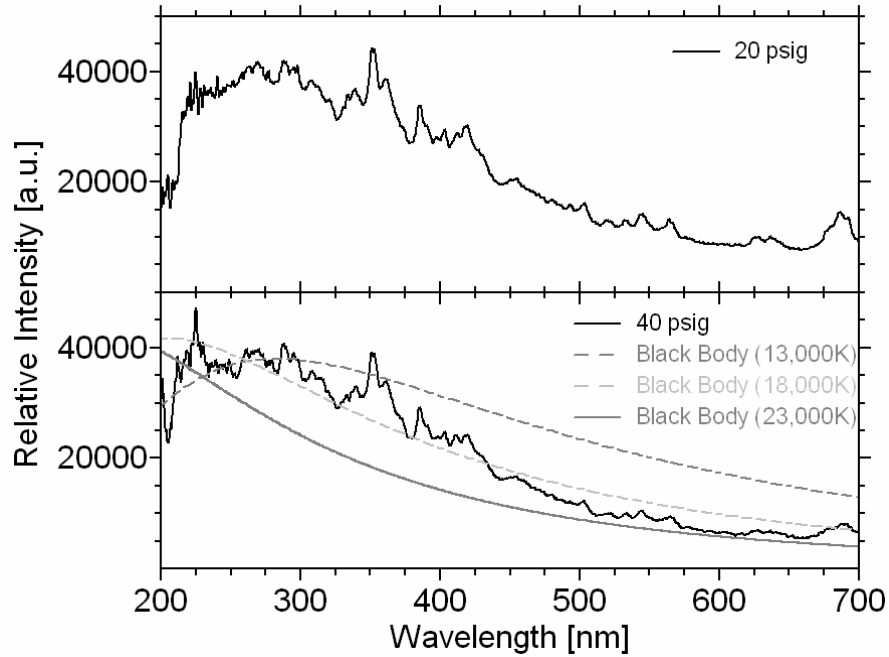
Figure 4.8: Spectra collected from a volume discharge in SF_6 at high pressures. Spectra gathered from low current breakdowns [41].
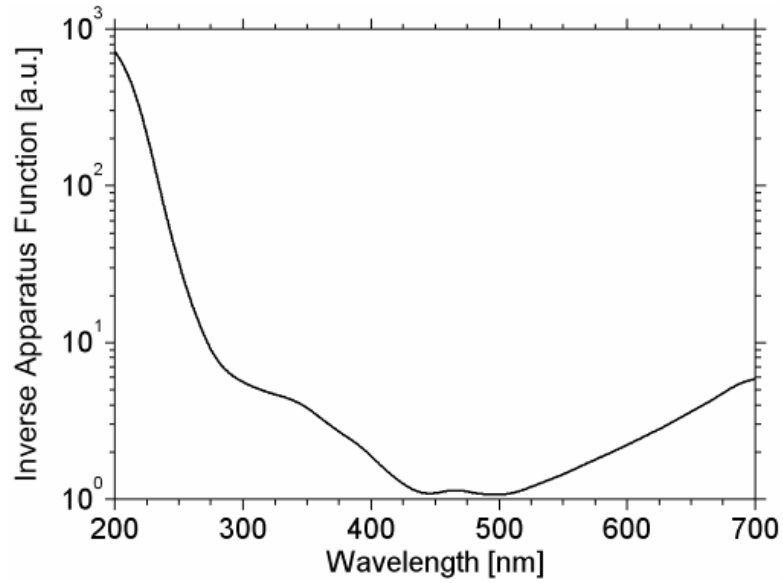
Figure 4.9: Scaling curve for all collected spectra, accounting for internal loss in the collection apparatus, spectrograph, and imaging camera.
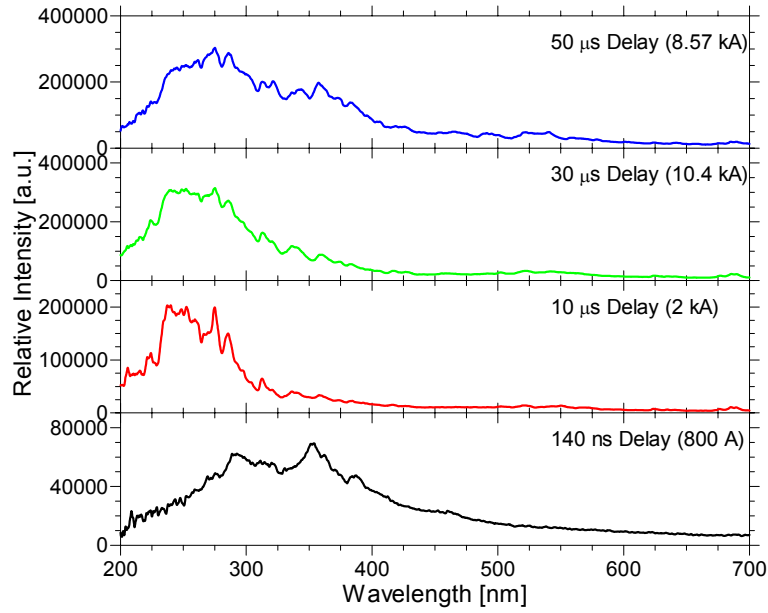
Figure 4.10: Spectra collected from a volume discharge in SF_6 at high pressures and at various current levels. Spectra gathered from higher current breakdowns.

According to previous surface flashover investigations, illumination of the surface with a UV pulse significantly decreases the delay time by up to 50% from pulsed excitation to flashover, and decreased variations in the delay time from shot to shot [42]. The UV also had a profound effect on the discharge path, resulting in the discharge following the surface as opposed to the electric field line [43]. This effect could easily contribute to the LTGS failure modes.

Comparison of the gathered spectra pattern to a black body radiation pattern was accomplished using Plank's equation. In Figure 4.10, Plank's equation:

$$\rho_\lambda(T) = \frac{2 \cdot h \cdot c^2}{\lambda^5} \cdot \frac{1}{\exp\left(hc/kT\lambda\right) - 1}$$

(4.1)

at 16,800 K, is used to model the broad features, which a high degree of correlation (h: Plank's constant, c: speed of light, λ: wavelength, T: blackbody temperature). It is

76

assumable that the higher the pressure, the closer the spectral output will be to a black body radiator. However, the spark plasma is still not completely thermalized at the 20 psig pressure as indicated by spectral line features superimposed onto the broad background.

Nevertheless, the estimated temperature of ~ 16,800 K for the SF_6 spark falls within the range of centerline temperatures measured for a stationary arc at a pressure of 120 psig (15,500 K for 400 A and 27,000 K for 13,000 A) [35], see Figure 4.11.
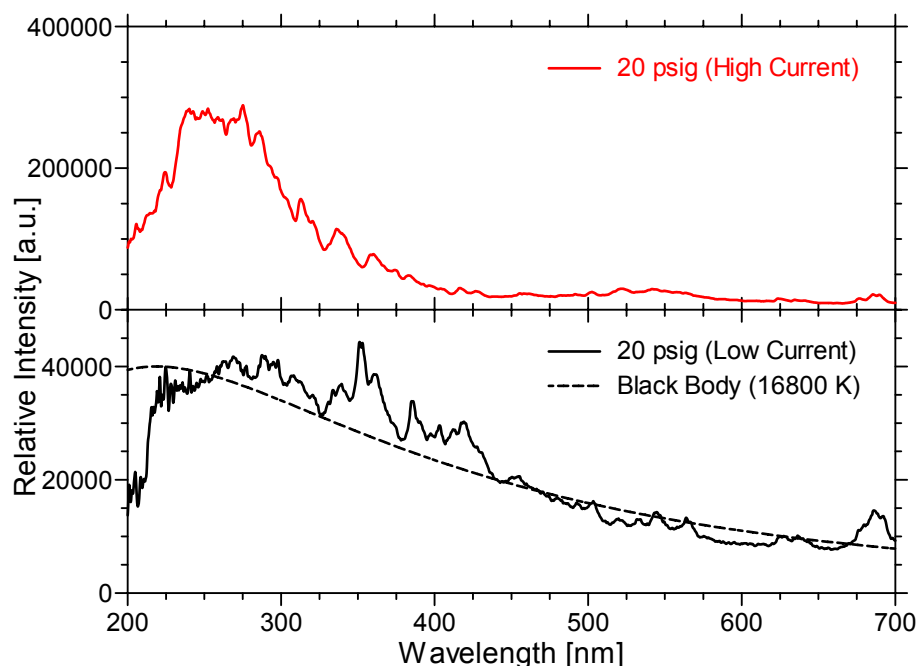
Figure 4.11: Spectra comparison of low current and high current breakdowns. High current is approximately 10.4 kA, and low current is roughly 1 kA. Low current breakdown at high pressures still maintains black body radiation pattern.

4.2.3 Solid By-Products of Volume Breakdown

After approximately 60 volume discharges at high currents several changes to the inside of the chamber were noticed. The most noticeable was a fine white powder like

77

substance found to be covering all components within the chamber. A thin film covered

items located greater than 5 inches horizontally from the breakdown event. An example

of the thin white layer found in the chamber can be seen in Figure 4.12.
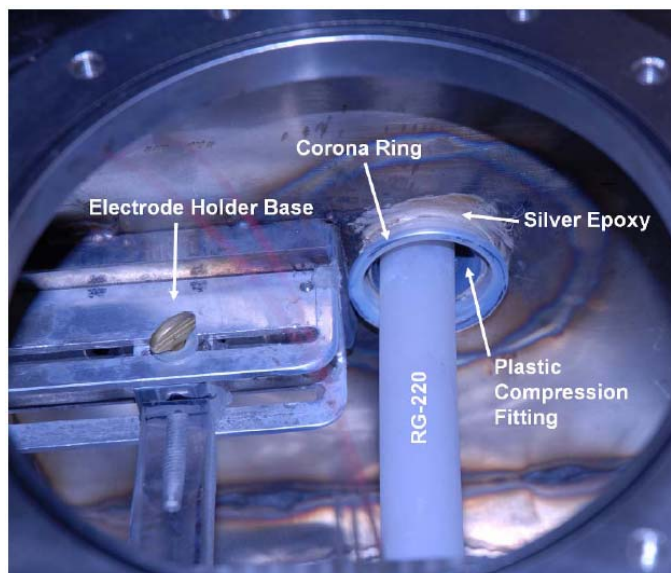
Figure 4.12: White powder deposit noticeable within the testing chamber. Powder is prominent on the electrode holder, corona ring and within the RG220 chamber entrance.

According to literature [36], X-Ray analysis has found that the dominant element

in the powder to be sulphur. The analysis also revealed a complex array of atomic species

– fluorine, sodium, aluminum, silicon, sulphur and potassium with traces of calcium and

zinc. The fluorine and sulphur were produced by SF_6 dissociation; silicon resulted from

the etching of the large chamber windows found in their experiment and the other atoms

were associated to the chamber aluminum-alloy walls. Except for the chamber walls

being stainless steel in our experiment, the design is similar in nature that found in the

literature reference. One could easily instigate that the powder found in the experiments

presented in this paper are similar in material composition. Identification of element

composition is still required.

The second most noticeable byproduct was that found on the stainless steel electrodes. Asides from pitting of the electrode surface, a build up on the electrode material was apparent. A literature search revealed that the deposit and accompanied pitting effect were caused by the fluorine disassociated from the SF_6 gas. The fluorine reacts with the surface of the electrodes to produce metal fluorides such as FeF_2. Although further identification is still required in our experiments, the same paper confirmed their findings through X-ray analysis. An example of the build up and deposit can be seen in Figure 4.13.

The last effect seen in the chamber was again found in conjunction to the electrodes. Hair-like fibers approximately 2.5 mm in length were found on both the anode and cathode, see Figure 4.13. Because of the method primary system design, when the capacitor is charged a DC voltage is put on the primary electrodes in the chamber. After firing of the primary setup, there is still a residual voltage left of the capacitor. At one such time, a voltage was left with ~ 80 Volts and the hairs became electrostatic. Once the capacitor was discharged, the electric field was removed and the hairs then drooped. Further investigation is required to identify the elements in the fibers, but they could contain either a metal fluoride or iron from the stainless steel electrodes.
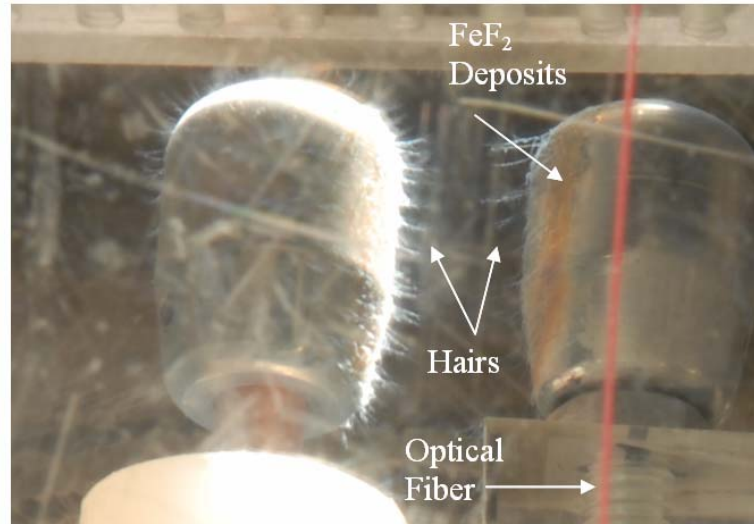
Figure 4.13: Hair like fibers found on the electrode surfaces with electrostatic effect. Metal fluorine deposits can be seen by the orange region.

4.3 Dielectric Surface Flashover

For the surface flashover experiments, the primary setup was used and the angled surface flashover electrodes were installed as well, see section 3.7.1. For a detailed explanation of the operation of the primary setup see section 3.8.2. The purposes of the surface flashover testing was to characterize various materials found within the LTGS, and then determine which characteristics would make a material more suitable for breakdown prevention and quantify the results. Asides from waveform analysis, each breakdown event was documented through spectroscopy. Post-surface flashover analysis will also be presented in this section.

4.3.1 Surface Flashover Images

Surface flashover testing occurred with various pressures of SF_6 and at varying current levels. The results for the higher pressures of SF_6 will be presented in this section,

while the lower pressure data can be found in Appendix C. A lower pressure breakdown image will be shown to emphasize the difference between high and low current breakdowns. The conditions of the surface were also varied to view the effects it had on the arc behavior at lower current levels. The three surfaces used are roughed (sand papered surface), grooved (notch cut tangential to the electrode slot) and smooth (cleaned factory smooth surface). This section will be limited to the results for a smooth surface. The data for the roughed and grooved surfaces at low currents can be seen in Appendix C. Although many material types were tested, Teflon and Lexan (polycarbonate) were materials of most interest and as such they will be presented. The distance between the electrodes averaged at 10 mm, but can vary ± .5 mm due to machining error.

Another noticeable difference in the surface flashover arc from lower to higher pressures was the color. As in the volume breakdown events, at lower pressures, the discharges had a pinkish hew, see Figure 4.14. Nitrogen is known to give a pinkish color when excited, and the change in color can be associated to a small leak in the chamber at the lower pressures.

Figure 4.14: Time integrated image of surface flashover of a Lexan (polycarbonate) surface in SF_6 at 10 torr. Charged electrode is on the left. Low current (< 2 kA) discharge.

Figure 4.15: Time integrated image of surface flashover of a Lexan (polycarbonate) surface in SF_6 at 40 pisg. Low current (< 2 kA) discharge.

Figure 4.16: Time integrated image of high current surface flashover at 20 psig of SF_6 on Lexan (polycarbonate) sample. ND = 4. High current (~ 10.2 kA) discharge. Side View.

Figure 4.17: Time integrated image of high current surface flashover at 20 psig of SF_6 on Virgin Teflon sample. ND = 4. High current (~ 10.2 kA) discharge. Side View.
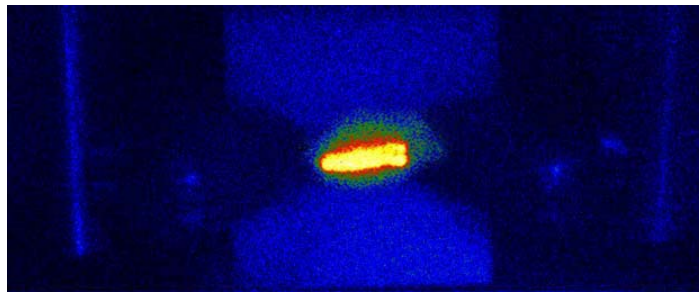
Figure 4.18: ICCD image of high current surface flashover at 20 psig of SF_6 on Virgin Teflon sample. ND = 3. High current (~ 800 A) discharge. 500 ns exposure time. Top view.
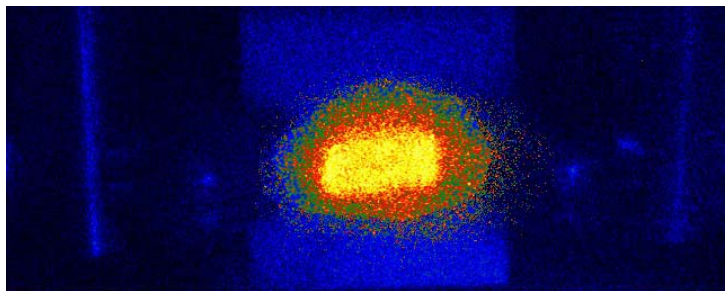
Figure 4.19: ICCD image of high current surface flashover at 20 psig of SF_6 on Virgin Teflon sample. ND = 3. High current (~ 2 kA) discharge. 500 ns exposure time. Top view.
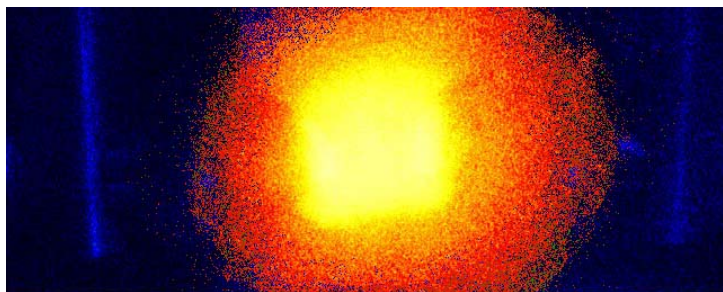
Figure 4.20: ICCD image of high current surface flashover at 20 psig of SF_6 on Virgin Teflon sample. ND = 4. High current (~ 10.2 kA) discharge. 500 ns exposure time. Top view.
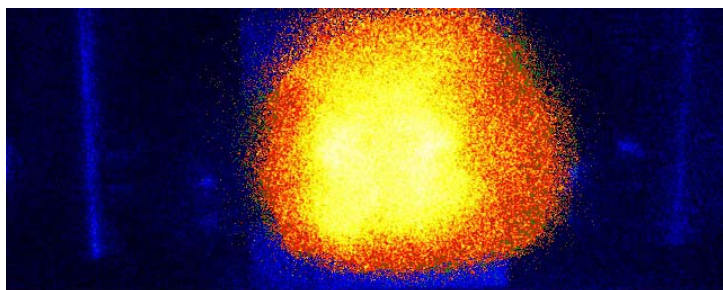
Figure 4.21: ICCD image of high current surface flashover at 20 psig of SF_6 on Virgin Teflon sample. ND = 4. High current (~ 8.6 kA) discharge. 500 ns exposure time. Top view.

In addition to the imaging of the surface flashover event, the time delay for breakdown was also recorded and was most revealing for the pulsed voltage hold-off capabilities of different materials. For the various materials tested at atmospheric pressure (Lubbock, TX: ~680 torr), a comparison table was created and lists the average time delays sorted by field strength, see Figure 4.22. The materials are sorted by field strength due to minor gap adjustments (± 1 mm) originating from the machining process. Despite the varying field strengths, Figure 4.22 indicates that Teflon had a longer breakdown delay time even at a higher applied field when compare to the Lexan and the epoxies. The one sample of Plexiglas (material taken directly from an unused Z switch envelope) exhibited the best performance at 1 atmosphere of SF_6, but must be treated with caution

since only a single sample was tested. The reason for this discussion of the lower pressure

results is due to a hypothesis of breakdown time delay and the dielectric constants.

Lexan, Teflon and Plexiglas have dielectric constants between ~ 2 to 3, while the epoxy

based materials have a relative permittivity of ~ 5, which could help explain their poor

performance. A higher dielectric constant could lead to increased electron emission at the

triple point.
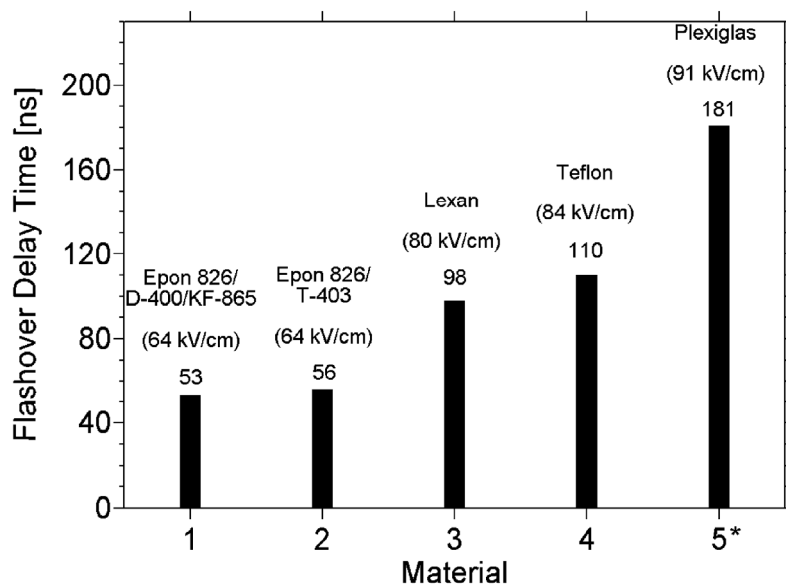
Figure 4.22: Dielectric material comparison of the average time delays. Samples arranged
by field strength (asterisk indicates one sample only tested). Surface flashover event at
atmospheric SF_6 and at low current (< 2 kA) breakdown. Only one sample of Plexiglas.

At the higher current levels, the same trend between the Teflon and Lexan

samples was noticed, see Figure 4.23. Yet again, the Teflon held off at higher field

strengths for a longer amount of time.
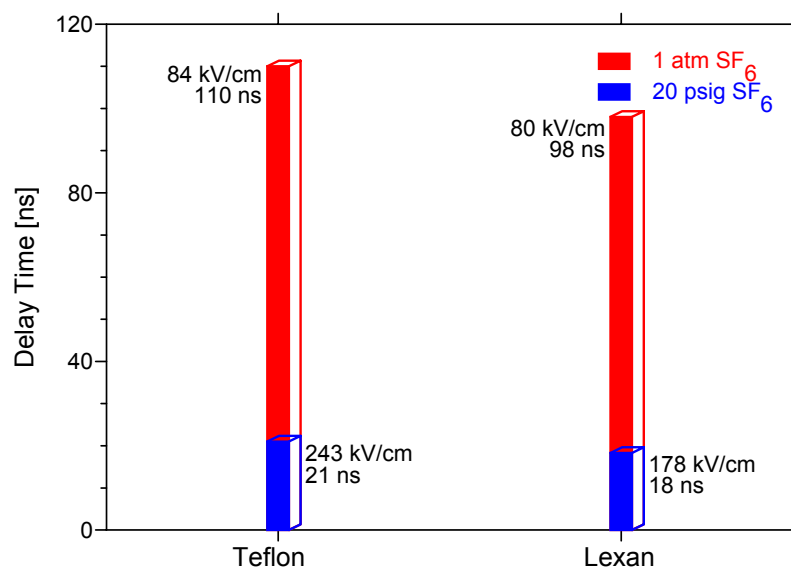
Figure 4.23: Dielectric material comparison of the average time delays. Samples arranged by time delay. Atmospheric breakdown with low current (< 2 kA) and 20 psig with high current (~10.2 kA).

4.3.2 Surface Flashover Spectroscopy Analysis

In order to understand the effects an applied UV excitation has on a surface flashover event, the surface flashover event must first be investigated and understood. The spectroscopic analysis of surface flashover events over various materials was documented and will be presented. For spectra collected at lower pressures, see Appendix C.

Overall, an important similarity was found between the surface flashover events and that of the volume breakdowns. At the lower current breakdowns, the spectra resembled the radiation pattern which was similarly found in the volume breakdown events, see Figure 4.24. A slight difference is the presence of carbon peaks found in the surface flashover due to the addition of the dielectric surfaces, see Figure 4.27. Easily noticeable are the carbon peaks at ~ 250 nm and at ~ 660 nm. Another interesting

observation is that since the composition of Teflon is ~76 % fluorine, a larger

contribution of fluorine is found in the spectra when compared to volume breakdowns at

high current amplitudes; see Figure 4.26, 4.10. A similar situation occurs in the Lexan

whose composition is ~ 75.6 % carbon. Some identified peaks can be seen in Figure 4.27.
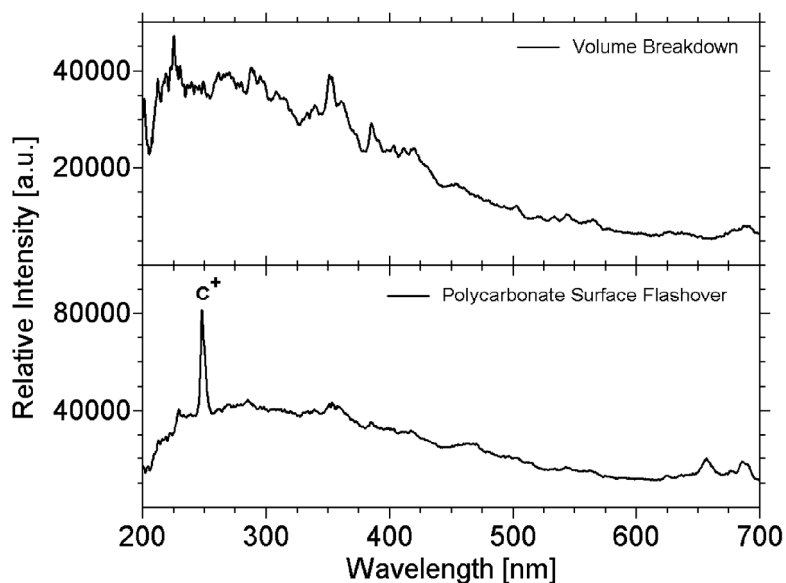
Figure 4.24: Comparison of spectra collected from a volume breakdown and a surface flashover of a Lexan (polycarbonate) surface in an SF_6 environment at 20 psig. Both are low current breakdown events.
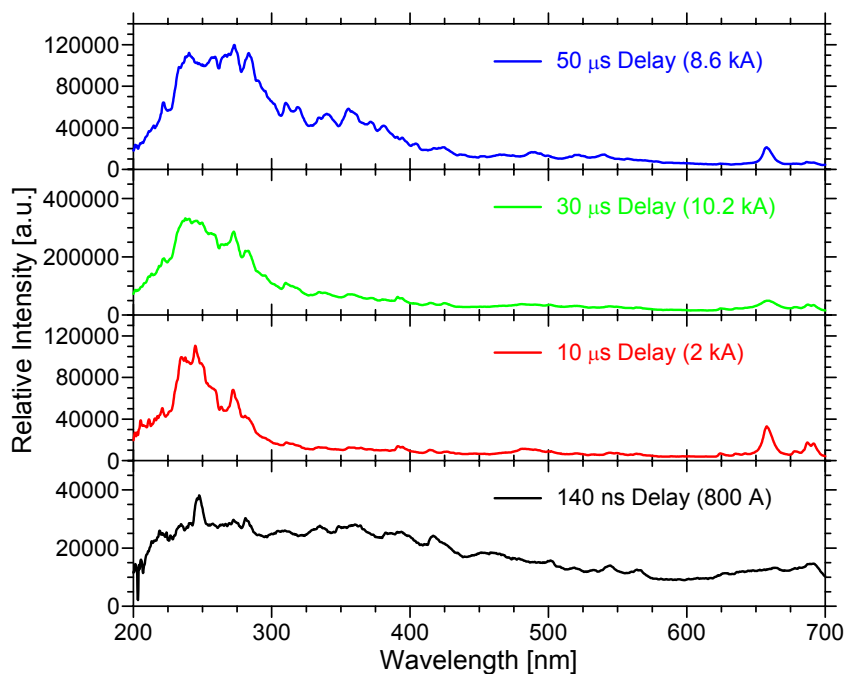
Figure 4.25: Spectra collected from a surface flashover on Lexan in SF_6 at 20 psig and at various current amplitudes.
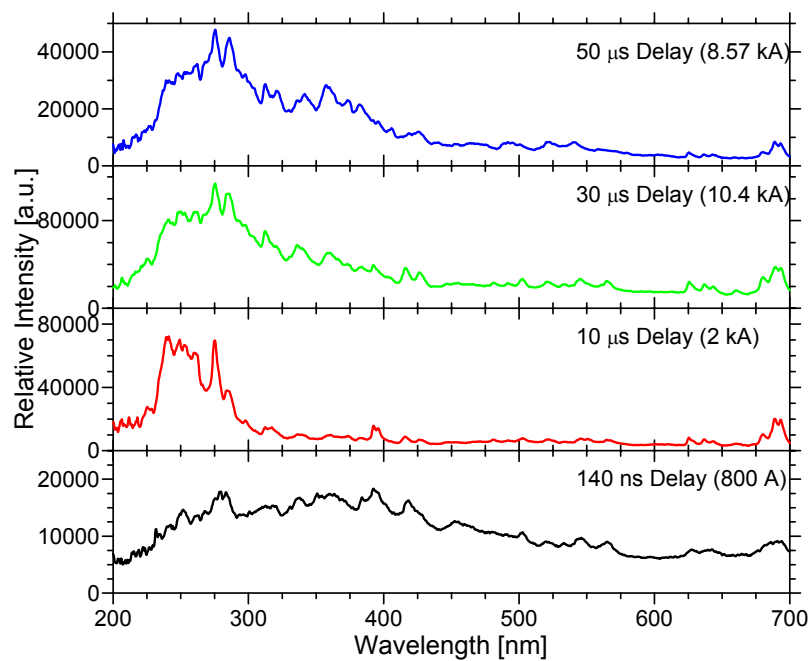
Figure 4.26: Spectra collected from a surface flashover on Teflon in SF_6 at 20 psig and at various current amplitudes.

As the current is increased in the arc, the UV contribution is larger than at the lower current levels. This is most likely attributed to the higher excitation states of the disassociated SF_6 molecules.
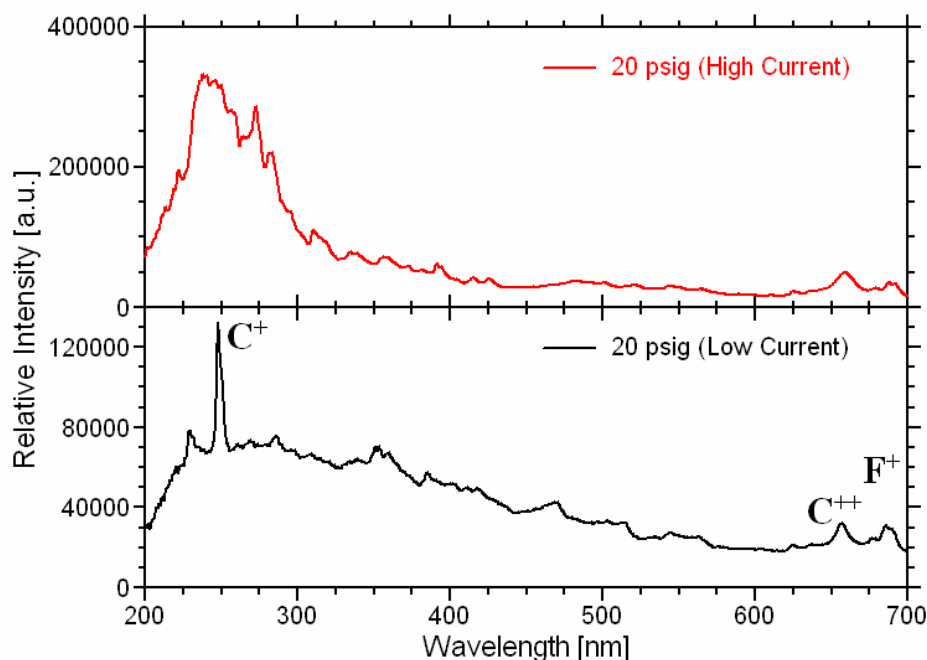
Figure 4.27: Spectra comparison of low current and high current surface flashover events on Lexan. High current is approximately 10.4 kA, and low current is roughly 1 kA. Low current breakdown at high pressures still maintains black body radiation pattern.

4.3.3 Post Surface Flashover Analysis

At the sponsor's request, post flashover analysis was also performed on the dielectric materials. The analysis helped in assessing the damage or tracking produced by the discharge in association with the material. Damage to the surface results in conditioning and as such the subsequent flashover event and material performance are both affected. Low level analysis was performed using an optical microscope. This level documented visual surface damage. The areas of interest were then investigated by means of a scanning electron microscope (SEM). The SEM proved useful for identifying

damage that could not be seen or was vague under a light microscope. At times, surface

contaminations required elemental identification, and as such analysis is further

performed via X-ray fluoroscopy. Most of the SEM analysis at this point was performed

on the low current discharges. Sulphur deposits at the low current discharges, for

example, were not as prominent in the higher current breakdowns. At the higher

breakdowns, the thin white sulphur film was easily collected via a cotton swab or finger.

The difference in the surface erosion with respect to the breakdown current can be seen in

Figure 4.35.
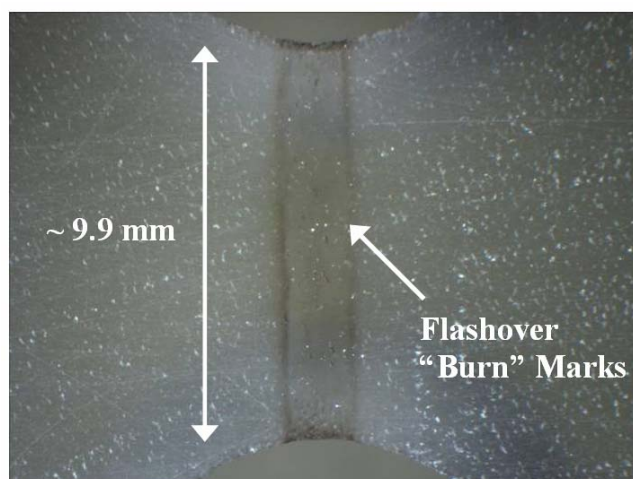
Figure 4.28: Smooth surface dielectric sample 826/D400/KF-865 cured at 80ºC for 3 days after 38 discharges (1 atm SF_6, 30 μC).
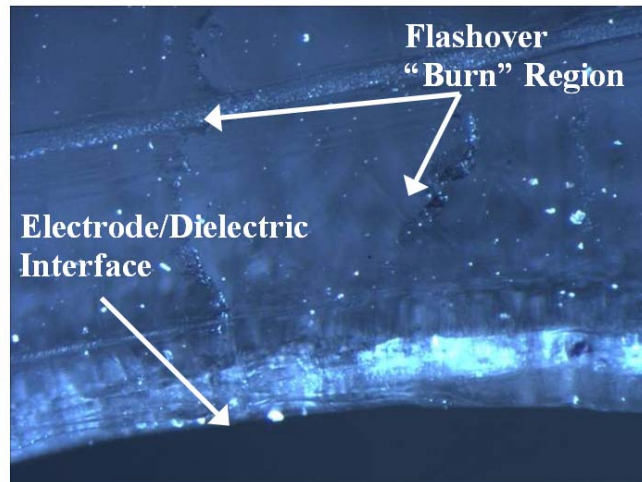
Figure 4.29: Smooth optical grade Lexan after 10 discharges (1 atm SF_6, 30 μC).
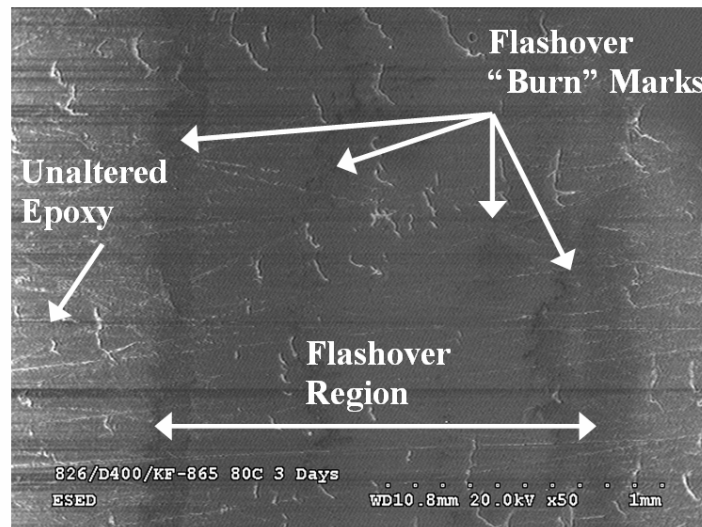
Figure 4.30: SEM image of smooth surface dielectric sample 826/D400/KF-865 cured at 80ºC for 3 days after 38 discharges (1 atm SF_6, 30 μC). Distinct difference between flashover region and the unaltered Epoxy surface.
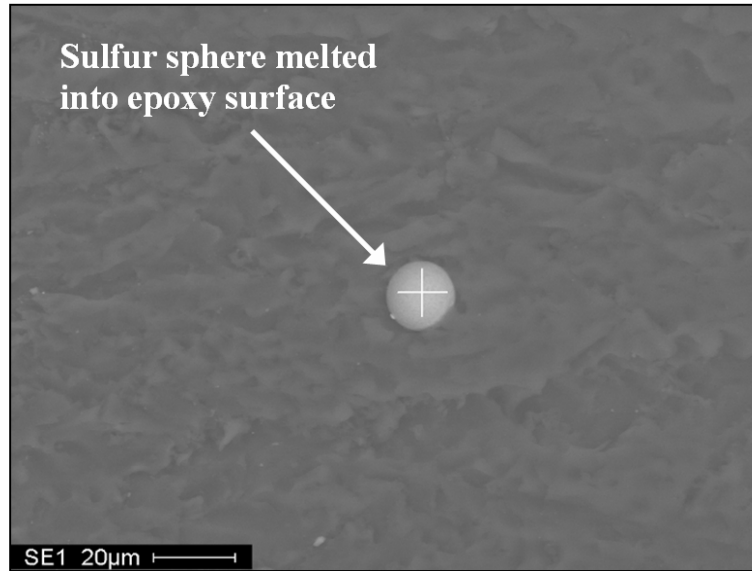
Figure 4.31: SEM image from dielectric material 826/D400/KF-865 used for X-ray fluoroscopy analysis (1 atm SF_6, 30 μC).
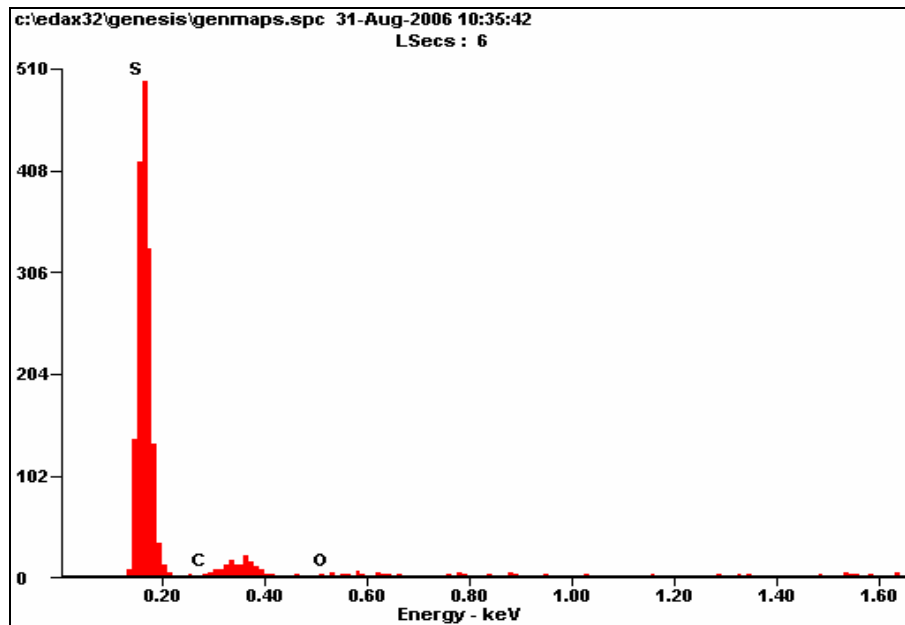
Figure 4.32: X-ray fluoroscopy results for crosshair location in Figure 4.31. X-ray fluoroscopy indicated sulphur deposit.
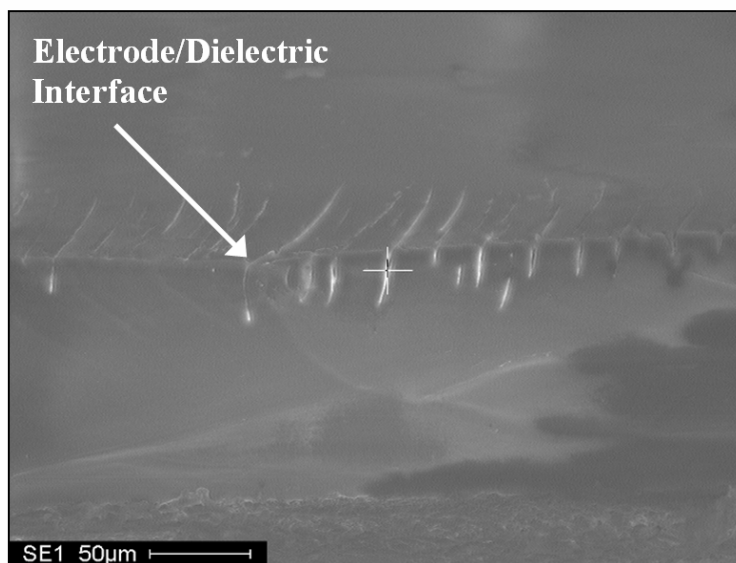
Figure 4.33: Lexan image used for X-ray spectroscopy (40 psig SF_6, 108 μC). Cross hair denoted point at which elemental composition was performed.
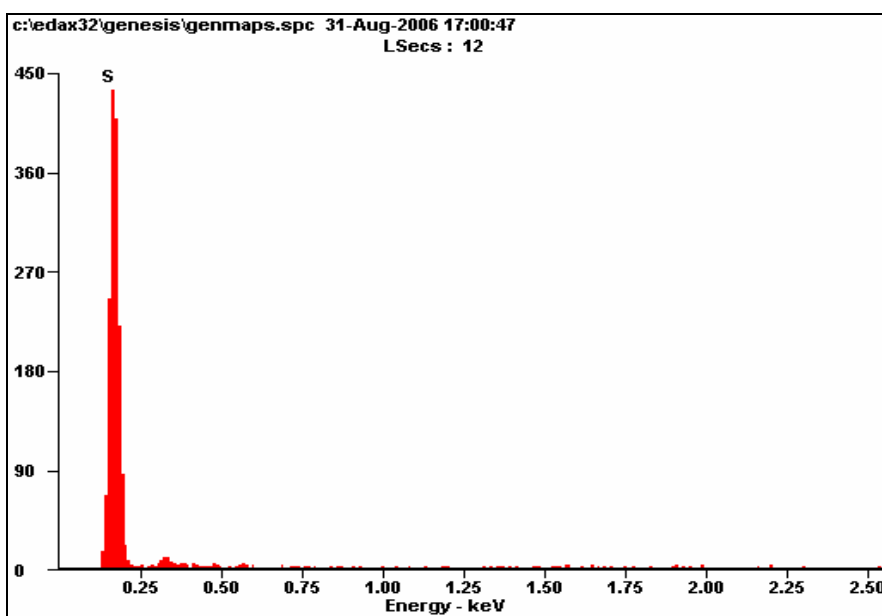
Figure 4.34: X-ray fluoroscopy results for crosshair location in Figure 4.33. X-ray fluoroscopy indicates sulphur deposit.

Although SEM analysis showed sulphur being disassociated from the SF_6, the gas was not the only material being excited. At the high current surface flashovers, carbon was being pulled from the surface of the dielectrics. In the top row of Figure 4.35, the black marks on the surface are from the carbon found in the various materials (Lexan,

Teflon, Rexolite). The carbon removal is more prominent in the Lexan and Rexolite than in Teflon. Most likely due to the fact that Teflon is composed of only ~ 24% carbon, a factor of 3 less than that found in Lexan (~75% carbon) [37].

The amount of carbon removed from the various materials is related to the quantity found in the material and directly impacts the behavior of the surface flashover event. An effect of surface flashover was found in the Lexan and Rexolite while charging the HV capacitor for a successive shot. The carbon pulled to the surface of the materials after a single surface flashover event was enough to create a carbon resistor (~50 kΩ). This new resistance allowed the current used to charge the HV capacitor a second path with lesser resistance and therefore did not allow for charging of the capacitor. Only one shot was allowed on the Lexan samples before cleaning of the surface was required. The same surface degradation occurred for the Rexolite, except that two flashover events were able to be performed rather than one as in the Lexan. The excitation of the carbon on the surface of the Teflon can be noticed by small black spheres appearing directly under the breakdown event. Not enough carbon was pulled from the material to cause an effect as seen with the Rexolite and Lexan. As a side note, a week after discharging across the Teflon sample, a yellow hew developed on the surface outside of the flashover region. Further investigation is required to identify the source of this phenomenon.
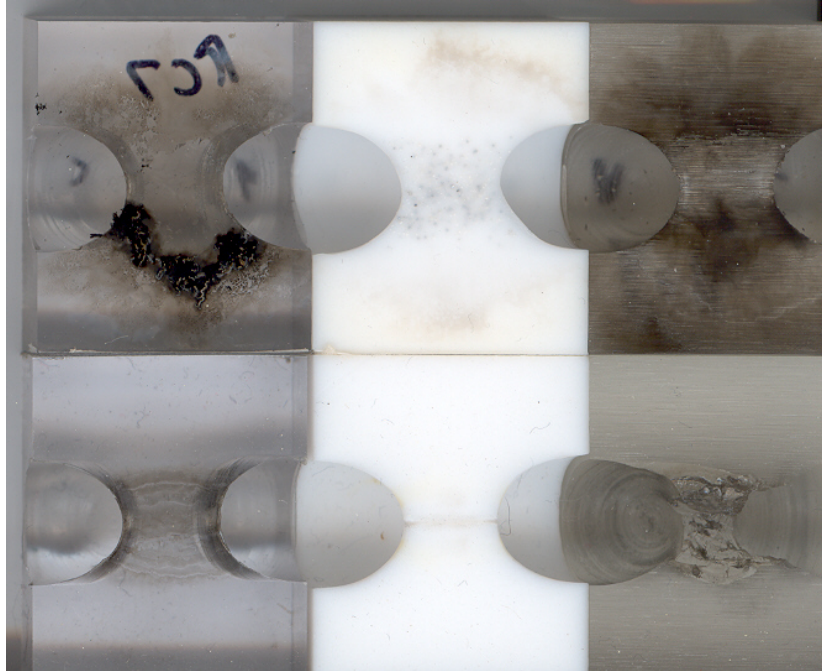
Figure 4.35: Material surface degradation comparison. Lexan, Teflon, and Rexolite from left to right respectively. Top row is high current discharges (301 mC), with 1, 6 and 2 surface discharges respectively. Bottom row is low current discharges at 100 shots per sample (108 μC).

CHAPTER 5

CONCLUSION

The phenomenology of volume breakdown and surface flashover in high pressure SF_6 has been experimentally investigated. While future work will focus on the direct impact of volume breakdown on a nearby surface under high electric field stress just below the surface flashover point, the following will summarize the results gained from each independent electrical breakdown type with a brief mentioning of a possible interaction between the two.

5.1 Volume Breakdown in SF_6

Photoemission of electrons by UV photons impacting the envelope is one of the suspected reasons that can initiate the unwanted tracking along the inside envelope surface in the Sandia LTGS. It is shown that a significant amount of UV light is produced by the volume spark in high pressure SF_6. The more intense light output is in the wavelength regime below 320 nm; a regime that has been identified in previous research as having a distinct effect on the spark path of flashover [1]. The majority of species contributing to the observed optical emission spectra between 200 and 700 nm has been identified, see Appendix B. It was possible to estimate the volume spark's electronic temperature (~35,000 K) for the lower pressures (50 torr) using lines of atomic spectra. However, for breakdown in 20 psig SF_6 or more, the broadband features mask distinct atomic or molecular lines. Assuming black body radiation the temperature is estimated to be of the order of 17,000 K at 20 psig (~2 kA) and similar to that at 40 psig (~2 kA).

The absence of metal lines in the low current breakdown spectra is a result of the low coulomb transfer and low current amplitude (~ 2 kA); however metal lines do show up in the optical emission spectra at higher currents (~10 kA). As expected, the spectral shape changes with the current amplitude and should continue to change as the current is increased to the 100 kA regime in future research. Overall, the volume breakdown results support the hypothesis of UV radiation contributing to the initiation of switch failure in the sense that UV radiation has been detected at wavelengths that a.) will cause photoemission of electrons from the surface and b.) easily propagates with little attenuation within radial distances found in the Sandia LTGS switch.

5.2 Dielectric Surface Flashover in SF_6

Several aspects of surface flashover along dielectric insulators have been studied in SF_6 environments. Imaging of the discharge along a dielectric surface revealed a material dependence on the discharge path. Previous low current experiments on grooved surface materials have shown that even with an electric field leading away from the surface, discharges continued to preferentially follow the surface for most materials; i.e. polycarbonate and the epoxies, indicating a strong interaction between the surfaces and the discharge. This interaction was believed to involve the productions of photoelectrons by the surface while exposed to UV radiation generated by the forming discharge, in which existence was confirmed by the collected optical emission spectra. Teflon showed the weakest interaction with the surface, following the surface only 50% of the time. This indicated that Teflon, or a material with similar or lower quantum yields for photo emission, would be the preferred choice for minimizing undesired envelope flashovers

[29].

In addition to imaging of the discharge, post-mortem imaging of the samples made the differences in surface conditioning apparent. For instance, the epoxy, Rexolite and polycarbonate exhibited very distinct visible surface damage, as opposed to Teflon that exhibited less visible damage. As surface conditioning reduces flashover fields of successive flashover events, Teflon was again shown superior to the other materials. This was further supported by the flashover delay time measurements, thus indicating that Teflon would hold off flashover longer under greater field stress than the epoxies, polycarbonate and Rexolite. It should be noted, however, that thus far only one Plexiglas sample was tested, and it too exhibited a long flashover delay time, and non-visible surface conditioning at low current surface flashover.

Comparing volume breakdown and surface flashover optical emission spectra revealed the presence of strong carbon lines in the UV for surface flashover at 20 psig. Since these line were absent in the volume breakdown spectra, they serve as an *in-situ* indicator for surface erosion for hydrocarbon based materials. This also implies that a measure of caution should be taken when using hydrocarbon based materials in envelope construction. As shown in section 4.3.3, the higher the composition of carbon in a material, the more damage to the surface; also possibly due to variances in the bond energies of the various materials.

The occurrence of sulfur on the dielectric surface, as recorded in literature [36], was consistent with the prevalent appearance of sulfur ionic lines in the flashover optical emission spectra (SII and SIII). The question remains as to whether these deposits are a cause or result of the poor hold-off characteristics of the materials. Future testing with

secondary surfaces placed in the chamber to measure hold-off potential, after collecting

any deposits created by an initial flashover event, should help clarifying the role of the

sulfur deposits.

REFERENCES

[1]   K. Morales, " Physics of Pulsed Unipolar Dielectric Surface Flashover at Atmospheric Conditions", Thesis for the Degree of Master of Science in Electrical Engineering, Texas Tech University, Lubbock, Texas, 2006.

[2]   Sandia Report: SAND2007-0217, "Fundamental Science Investigations to Develop a 6-MV Laser Triggered Gas Switch for ZR: First Annual Report", March 2007.

[3]   D. Lide, CRC Handbook of Chemistry and Physics, CRC Press, 81st Ed., 2000-2001.

[4]   D. K. Davies, "Charge generation on dielectric surfaces," Brit. J. Appl. Phys., Ser. 2, Vol. 2, 1969.

[5]   E. Nasser, Fundamentals of Gaseous Electronics, Wiley-Interscience, New York, NY, 1971.

[6]   B. G. Streetman and S. Banerjee, Solid State Electronic Devices, Prentice Hall, Upper Saddle River, NJ, 2000.

[7]   Y.P. Raizer, Gas Discharge Physics, Springer-Verlag, New York, NY, p. 71, 1991.

[8]   D. Alpert, D.A. Lee, E.M. Lyman, and H.E. Tomaschke, "Initiation of Electrical Breakdown in Ultrahigh Vacuum," Jour. Vac. Sci. & Tech., Vol. 1, Iss. 2, pp. 35-50, November 1964.

[9]   P.G. Slade and E.D. Taylor, "Electrical Breakdown in Atmospheric Air Between Closely Spaced Electrical Contacts," IEEE Trans. Components and Packaging Technologies, Vol. 25, No. 3, pp. 390-396, September 2002.

[10] Feuerbacher, Fitton, Willis, Photoemission and the Electronic Properties of Surfaces, John Wiley & Sons, 1978.

[11] Dionne, G. F., "Origin of Secondary-Electron-Emission Yield-Curve Parameters," J. Appl. Phys., Vol. 46, No. 8, August 1975, pp. 3347-3351.

[12] Meek, J.M. and Craggs, J.D., Electrical Breakdown of Gases, John Wiley and Sons, 1978.

[13] Christophorou and Olthoff, "Electron Interactions with SF_6", Journal of Physical and Chemical Reference Data, 29 (3): 267-330, May-Jun 2000.

[14] J. T. Krile, "Surface Flashover Under RF and Unipolar Excitation at Atmospheric Conditions," Dissertation for the Degree of Doctor of Philosophy in Electrical Engineering, Texas Tech University, Lubbock, Texas, 2006.

[15] E. Kuffel, W. S. Zaengl, and J. Kuffel, High Voltage Engineering: Fundamentals, Newnes, New York, NY, 2000.

[16] Brown, Sandborn C., Introduction to Electrical Discharges in Gases, John Wiley & Sons Inc., New York, 1966.

[17] G.G. Raju, Gaseous Electronics, CRC Press, 2006.

[18] L B. Loeb, Basic Processes of Gaseous Electronics, University of California Press, 1955.

[19] H Raether, Electron Avalanches and Breakdown in Gases, Butterworths, London, 1964.

[20] H Bluhm, Pulsed Power Systems: Principles and Applications, Springer, 2006.

[21] Miller, H., "Surface Flashover of Insulators," IEEE Transactions on Electrical Insulation, Vol. 24, No 5, pp. 765-786, October, 1989.

[22] Papoular, R., Electrical Phenomena in Gases, American Elsevier pub. Co. Inc., New York, 1965.

[23] S. Schreier, On the Beakdown Voltages of Some Electronegative Gases at Low Pressure, IEEE Trans. PAS, 83, 468, 1968.

[24] I. W. McAllister, "Electric Fields and Electrical Insulation", IEEE Trans. On Dielectrics and Electrical Insulation, Vol. 9, No. 5, Oct. 2002.

[25] I. W. McAllister, and G. C. Crichton, "The Concept of Paschen's law with Reference to SF_6", J. Phys. D: Appl. Phys. 20, 1537-1539, 1987.

[26] R. A. Kishek, Y. Y. Lau, L. K. Ang, A. Vafells, and R. M. Gilgenbach, "Multipactor discharge on metals and dielectrics: Historical review and recent theories", Physics of Plasmas, Vol. 5, No. 5, pp. 2120-2126, May, 1998.

[27] S. E. Black, "Nonlinear Magnetic Switches for Pulse Generation", Thesis for the Degree of Master of Science in Electrical Engineering, Texas Tech University, Lubbock, Texas, 1980.

[28] G. T. Coate, and L. R. Swain Jr., High-Power Semiconductor-Magnetic Pulse Generators, The M.I.T. Press, 1966.

[29] J. K. Krile, R. Vela, A. A. Neuber, H. G. Krompholz, "Pulsed Dielectric Surface Flashover in an SF_6 Environment", IEEE Trans. on Plasma Sciences, submitted for publication.

[30] H. Krompholz, K. Schoenbach and G. Schaefer, "Transmission Line Current Sensor," Proceedings of the ITMC-IEEE Instrumentation and Measurement Technology Conference, pp. 224-227, March 1985.

[31] S. T. Pai and Qi Zhang, Introduction to High Power pulse Technology, World Scientific Publishing Co. Pte. Ltd., 2003.

[32] J. Krile, "Physics of Dielectric Surface Flashover at Atmospheric Pressures," Thesis for the Degree of Master of Science in Electrical Engineering, Texas Tech University, Lubbock, Texas, 2003.

[33] J. Tom, H. A. Verhaart, A. L. Verhage, and C. S. Vos, "Photo-emission of Charged Insulators in Insulating Gases," Proceedings of the 2nd International Conference on Conduction and Breakdown in Solid Dielectrics, pp. 301-307, Erlangen, 1986.

[34] A. A. Guzhov, and Yu. A. Shuba, "The Phototemission of Some Massive Insulators in the Vacuum Ultraviolet," Optical Technology, Vol. 38, No. 4, pp. 198-199, April 1971.

[35] J.J. Lowke and R.W. Liebermann, "Predicted Arc Properties in Sulfur Hexafluoride," J. Appl. Phys., Vol. 42, 3532-3539, 1971.

[36] T. C. Mortensen, Y. Bunganaen, G. B. Scelsi, G. A. Woolsey, "Gaseous and solid by-products of SF_6 discharges", Properties and Applications of Dielectric materials, 1994., Proceedings of the 4th International Conference on, Vol. 1, Iss., 3-8 Jul 1994. pp. 135-138.

[37] NIST Atomic Spectra Database Lines Form, online at: http://physics.nist.gov/PhysRefData/ASD/lines_form.html

[38] K. P. Morales, J. T. Krile, A. Neuber, and H. Krompholz. "Pulsed Dielectric Surface Flashover at Atmospheric Conditions," Pulsed Power Conference, 2005 IEEE, Vol., Iss., June 2005, pp 1147-1150.

[39] J. Corley, et. al., "Tests of 6-MV Triggered Switches on APPRM At SNL", PPCS2001, pp 1778, IEEE 0-7803-7120-8, 2002.

[40] J. Corley, et. al., "Development/Tests of 6-MV Triggered Gas Switches at SNL", PPC2003, pp 875, IEEE 03CH37472C, 2003.

[41] J. K. Krile, R. Vela, A. A. Neuber, H. G. Krompholz, "Spectral Analysis of Pulsed Volume Breakdown in SF$_6$ at High Pressures", IEEE Trans. on Plasma Sciences, submitted for publication.

[42] J. Krile, A. Neuber, J. Dickens, and H. Krompholz, "DC and Pulsed Dielectric Surface Flashover at Atmospheric Pressure," IEEE Trans. On Plasma Sci., 1149-1154, Aug 2005.

[43] K. P. Morales, J. T. Krile, A. A. Neuber, and H. G. Krompholz, "Pulsed Dielectric Surface Flashover in Atmospheric Conditions," IEEE Trans. on Dielectrics and Electrical Insulation, vol. 13, no. 4, pp. 803-809, Aug. 2006.

[44] F. Hegeler, "Dielectric Surface Flashover in a Simulated Low Earth Orbit Environment," Dissertation for the Degree of Doctor of Philosophy in Electrical Engineering, Texas Tech University, Lubbock, Texas, 1995.

APPENDIX A

PASCHEN'S LAW WITH REFERENCE TO SF$_6$

$A_{sf6} := 3.74 kV$

$B_{sf6} := 6.96 \dfrac{kV}{mm \cdot bar}$

$V_b(x) := x \cdot 8.84 \left(\dfrac{kV}{mm \cdot bar} \right) + .5kV$ [1] Assuming a uniform electric field - requires adjusting to desired electrode configuration. See discussion below.

$V_{b2}(x) := A_{sf6} + B_{sf6} \cdot x$ [2] See discussion below.

pd [torr*m]
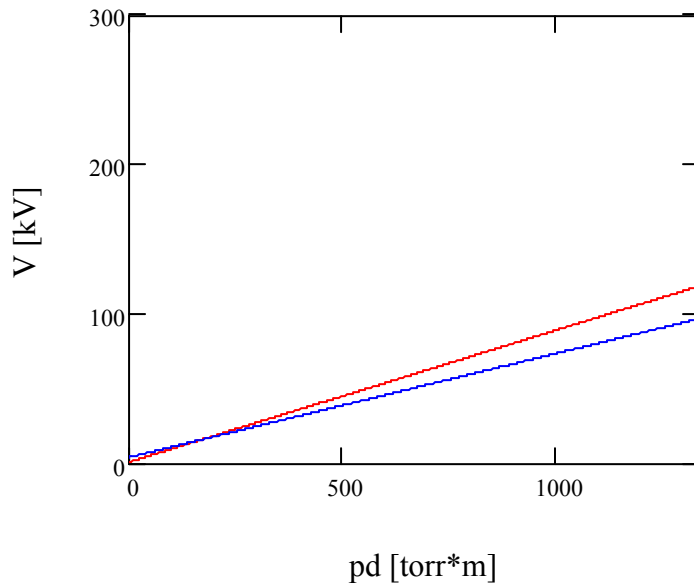
—— Curve according to reference 1
—— Curve according to reference 2

Discussion of curves:

The linearity of the paschen curve for SF_6 has been experimentally proven for ranges of

$.25 \le \dfrac{p}{bar} \le 4$ [2]. The electrode geometry was a point plane configuration, a hemispherically-

ended rod of tip radius 8 mm with a gap spacing of 5 mm [2]. As stated above, the equation from bluhm assumes uniform electric fields. Equations are available which will adjust Bluhm's breakdown equation for various electrode geometries [1].

It should be noted that the paschen curve for SF_6 deviates from linearity (tails off) at the ends [8].

According to literature [3,4] there is a E/p limit below which no sparking should be possible regardless of the magnitude of p*d to take note of for SF_6 :

<u>Predicted:</u> $117 \dfrac{V}{cm \cdot mmHg}$

<u>Observed:</u> $117.5 \dfrac{V}{cm \cdot mmHg}$ [3]

$103 \dfrac{V}{cm \cdot mmHg}$ [4]

References:

[1] Bluhm, Pulsed Power Systems, Springer, pp. 13-15

[2] McAllister, Crichton, The Concept of Paschen's law with reference to SF6, J. Phys. D: Appl. Phys. 20 (1987) 1537-1539.

[3] M. S. Bhalla and J. D. Craggs, Measurement of Ionization and Attachment Coefficients in Sulphur Hexafluoride in Uniform Fields, Proc. Phys. Soc., 1962, vol. 80.

[4] Geballe, R., and Reeves, M. L., A condition on Uniform Field Breakdown in Electron-Attaching Gases, 1953, Phys. Rev., 92, 867

Selected papers for more on SF_6 Paschen curve issues:

[5] Berger, Senouci, The role of impurities on the deviation from paschen's law of SF_6, J. Phys. D: Appl. Phys. 19 (1986). Printed in Great Britain.

[6] McAllister, Electric Fields and Electrical Insulation, IEEE Transactions on Dielectrics and Electrical Insulation, Vol. 9, No. 5, October 2002.

[7] McAllister, Crichton, The concept of paschen's law with reference to SF_6, J. Phys. D: Appl. Phys. 20 (1987) 1537-1539. Printed in the UK.

[8] Osmokrovic, krivokapic, Krstic, Mechanism of Electrical Breakdown left of Paschen minimum, IEEE, Transactions on Dielectrics and Electrical Insulation, Vol.1, No.1, February 1994. pp77-81.

APPENDIX B

SPECTRAL ANALYSIS OF PULSED VOLUME BREAKDOWN IN SF$_6$ AT HIGH PRESSURES

John T. Krile, *Member*, *IEEE*, Russell Vela, *Student Member*, *IEEE*, Andreas A. Neuber, *Senior Member, IEEE*, and Hermann G. Krompholz, *Senior Member*, *IEEE*

Abstract—**The Z-machine, located at Sandia National Laboratories, is currently undergoing refurbishment to increase the output drive current. Due to increased switching voltage requirements, some switch failure modes have been identified with the laser trigger gas switch design, including envelope surface flashover. In order to improve the performance and life time of these switches a basic understanding of the underlying physics of the failure mechanisms is required. A small-scale experimental setup has been constructed to approximate conditions within the switch. The possible impact of the SF$_6$ volume spark between the switch electrodes on the envelope surface flashover is investigated. Measured optical emission spectra of the SF$_6$ volume spark in a wide pressure range, rough vacuum to 40 psig, are analyzed regarding their potential to contribute to switch failure.**

Index Terms—**Breakdown, SF$_6$, Spectroscopy**

I. INTRODUCTION

PREMATURE switch failure has become a problem in the refurbishment of the Z-machine located at Sandia National Laboratories [1], [2]. The Laser Triggered Gas Switch, LTGS, typically operated at above atmospheric SF$_6$ pressures, such as 40 psig, has evolved to accommodate significantly higher voltage requirements over the years. The generic switch design, with 305 mm envelope diameter and 165 mm vertebrae diameter, can be seen in Fig. 1. In the present design, a primary failure mode is surface flashover in the high pressure gas (SF$_6$, > 40 psig) on the inside of the PMMA envelope. This surface flashover occurs initially during the regular cascade switching process without affecting the switch's electrical performance. However, the switch will pre-fire in the successive shot. The damage to the envelope has to be repaired before normal switch operation can resume. It is believed that damage to the envelope occurs prior to the failure. Under normal operation the envelope is exposed to optical radiation (UV-VIS) generated by the volume breakdown of the cascade section of the switch. In order to determine what effect this illumination might have on the envelope, a smaller scale pulsed SF$_6$ volume discharge setup was constructed. Optical emission spectroscopy is preformed on the radiation emitted by the volume spark and the emission spectrum is analyzed.

A literature survey focused on SF$_6$ emission spectra for the conditions found in the LTGS uncovered little information. Most research was done on stationary SF$_6$ arcs or for the power distribution industry, with the goal of detecting corona discharges in insulating SF$_6$. This is used primarily as a method of detecting emerging failures in SF$_6$ insulated power systems [3]-[5]. A reoccurring theme in the literature is the pronounced effect of nitrogen contamination on the observed optical emission spectra. Having as little as a 1% fraction of N$_2$ in SF$_6$ will show up prominently as the N$_2$ second positive band in the otherwise SF$_6$ dominated spectrum. There are several shortcomings in the literature, for instance, only the raw spectra are typically shown. This makes evaluating the plasma temperature from the spectrum difficult if not impossible. In some cases the temperature is inferred from spectra generated by the nitrogen contamination in the system; however, this is again done without adequate sensitivity correction. It is

imperative for accurate temperature determination to correct the raw spectra with the apparatus' spectral sensitivity. In addition to plasma temperature, identification of spectral line, specifically sulfur and fluorine from the dissociated SF_6, is difficult using merely the raw spectra only. By identifying these lines in the corrected spectra the plasma temperature can be more accurately determined.
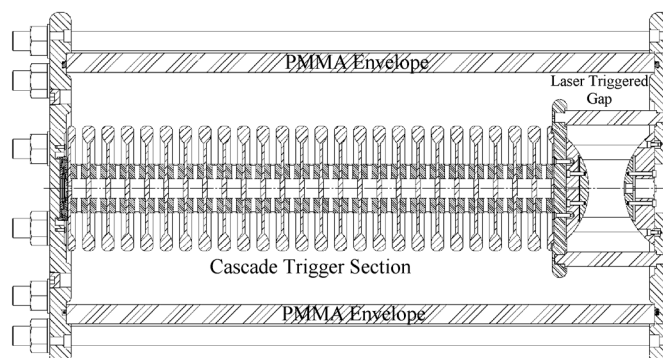
Fig. 1: Cross-sectional view of the LTGS with the laser triggered gap on the right and the self-break cascading section on the left. The cascade section is where envelope failures occur [2].

In the following, experimental results of pulsed volume breakdown in SF_6 at pressures from 10 torr to 40 psig are presented. Besides fast voltage and current monitoring of the breakdown event, an increased emphasis was put on imaging the event as well as gathering optical emission spectra (~200 nm to 700 nm). The role of UV emission due to a volume SF_6 spark as potentially flashover hold-off reducing cause is discussed. As much as possible, the small scale experiment was designed to reproduce at least partly the conditions as they are found in the large 5 MV Z switch. The physical dimensions of importance for the impact of volume breakdown on surface flashover are the backbone electrode gap distance of 9.5 mm and the distance between electrodes and envelope, 69.85 mm.

II. Experimental Setup

A. Test Chamber

In order to accurately simulate the conditions within the LTGS a test chamber has been constructed that can support pressures from 10 torr absolute to 40 psig, see Fig. 2. In order to achieve this pressure range the chamber is constructed of stainless steel. The chamber contains a variety of access ports to allow for the various diagnostics as well as pump-down and fill line access. The high voltage connection to the chamber inside is made by a custom fabricated feed through using an RG-220 cable fed through a compression port. The cable acts as a holder for one of the electrodes, while a sliding assembly attached to the chamber holds the ground electrode. This assembly enables the changing of the electrodes as well as the adjustment of the gap spacing.
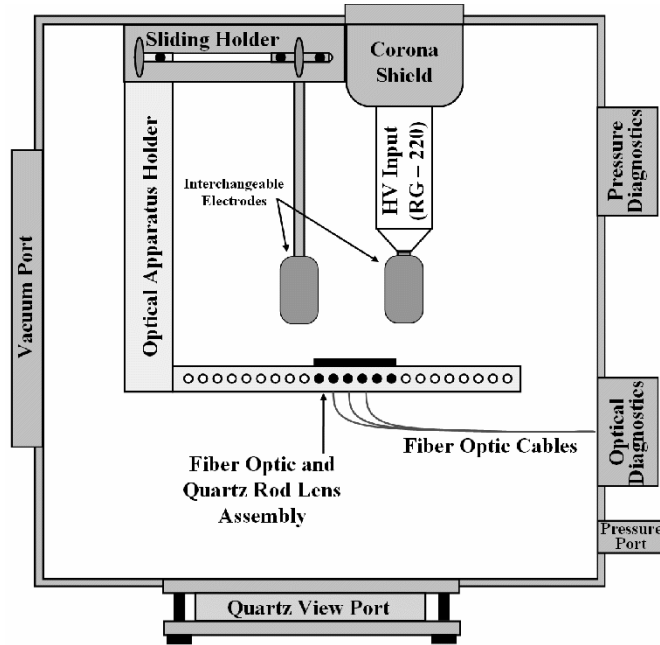
Fig. 2. Overview of the high pressure chamber (25.4 cm x 25.4 cm x 25.4 cm). Additional electrodes and flashover surfaces are omitted for clarity.

The chamber also contains features to study the effects of volume discharge on adjacent dielectric surfaces. Dielectric sample holders, complete with secondary excitation apparatus and electrodes, are located above and below the primary discharge electrodes. The sample holders ensure the distance from the primary gap to the dielectric is similar to that found in the LTGS. Future studies are aimed at investigating the direct impact of volume breakdown on surface flashover initiation, as well as the effect on hold-off voltages for various dielectric materials.

B. Electrical Diagnostics

Measurement of the breakdown requires instrumentation with high temporal resolution. For this reason, a capacitive voltage divider with a sensitivity of 109 mV/kV and a rise time better than 1 ns was incorporated on to the 52 ohm transmission line. Traveling wave current sensors are utilized for the current measurements and have a sensitivity of 0.1 V/A with a ~1 ns rise time. All signals were then recorded using a 500 MHz bandwidth, 2 GSa/s, Agilent Infinium oscilloscope.

C. Excitation

Transient excitation is achieved via an eight stage, 360 kV maximum pulse, Marx generator. The Marx generator is remotely charged with a HV DC power supply capable of generating up to 125 kV at a maximum of 2 mA. The Marx generator is triggered by a 40 kV high voltage pulser. When triggered, the voltage pulse from the Marx generator travels down a 1 m transmission line, through a 52 Ω water resistor (cupric sulfate), and then to the electrodes in the breakdown chamber. The Marx output voltage was typically set to 300 kV, which corresponded to a coulomb transfer of ~200 μC. Fig. 3 shows a typical voltage and current signal for volume breakdown.
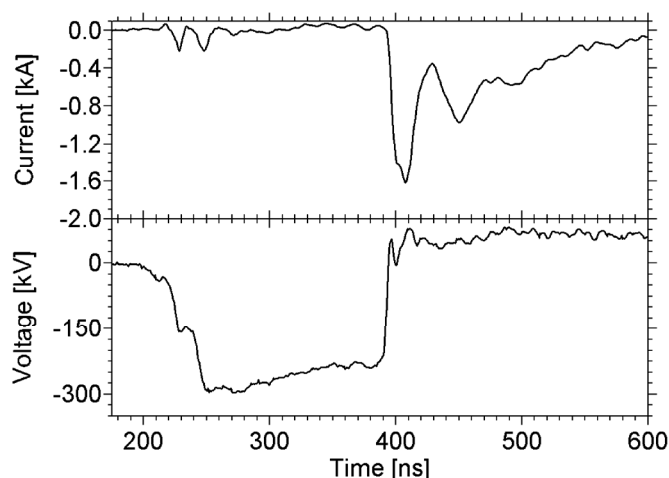
Fig. 3: Current and voltage waveform of SF_6 breakdown across a 9.52 mm gap at 40 psig. The voltage signal is not corrected for the voltage sensor droop.

D. Optical Diagnostics

Imaging of the flashover event is achieved using a digital SLR camera with open shutter exposure and neutral density filters with values ranging from 1 to 3. The SLR is primarily used with the high pressure setup due to the EMI generated by the discharge that could damage more sensitive equipment. The camera is fitted with a zoom lens and is positioned directly outside the breakdown chamber. The camera can either be focused on the gap through the quartz view port or through a smaller viewport, in the top flange of the chamber. The second method is utilized to allow for both imaging of the gap and collection of optical emission spectra concurrently.

In order to help determine some of the processes contributing to the breakdown, a spectrograph is utilized to analyze the emissions from the discharge. The spectrograph is an Oriel MS 257 ¼ meter imaging spectrograph. It has toroidal mirrors designed to allow multiple vertical points, or fiber optic inputs, to be diffracted simultaneously. This feature enables measuring spectra concurrently from multiple points. The light emitted by the volume spark is collected utilizing cylindrical quartz lenses that focus the optical light emission from three spatially distinct areas between the electrodes into three fiber optic cables leading back to the spectrograph, see Fig. 4. In this way, spatially resolved light emission can be collected concurrently. The spectrum is recorded with an intensified CCD camera located inside a screen room.
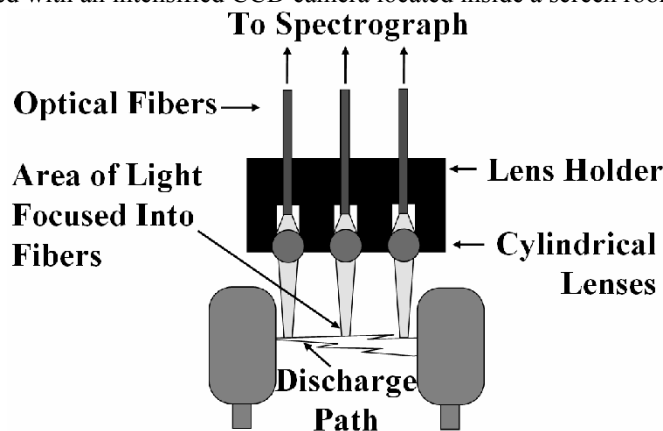
Fig. 4 Cross-section of the optical emission collection apparatus

In order to verify that UV is easily transmitted through high pressure SF_6, a broadband UV source was utilized to measure the spectral transmission through 12.7 cm of SF_6 and N_2, both at 40 psig, see Fig. 5. Overall, the SF_6 and the N_2 reference curve match well, clearly indicating very little, if any, absorption for

109

SF_6 in the range from 250 to 800 nm for the conditions found in the LTGS switch. It should be noted that the signal below ~ 250 nm becomes very noisy, which is due to the decreasing light output of the broadband source at shorter wavelength and the also smaller spectral response of the utilized spectroscopy system at shorter wavelength.

The lack of UV absorption by SF_6 is confirmed utilizing absorption cross section data available in the open literature [6], [7]. Using Beer's law for light absorption, it is calculated that 40 psig of SF_6 will transmit UV easily down to 160 nm, see Fig. 6. Note that the cut-off wavelength of air at around 180 nm is well known and due to dissociation of the O_2 molecule.

Since there is presently no known absorption resonance of SF_6 between 165 nm and 250 nm, it should hence be assumed that virtually all light between 160 and 800 nm is transmitted easily through up to 70 mm of SF_6 at 40 psig.
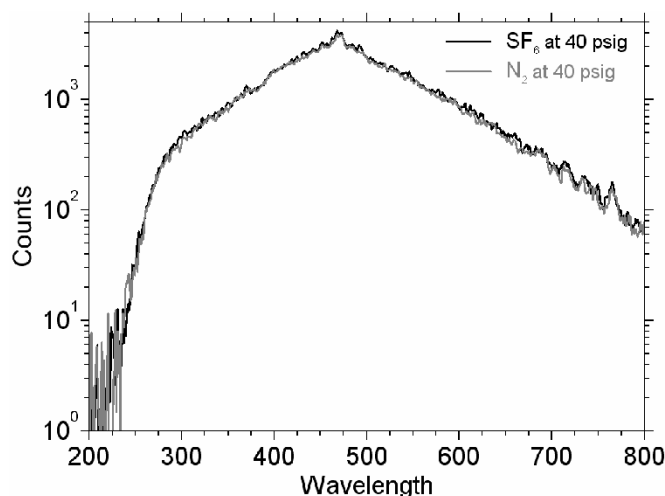
Fig. 5: Measured spectral response of the TTU spectroscopy system to a broadband Xe high pressure lamp for transmission through 12.7 cm of SF_6 or N_2, respectively.
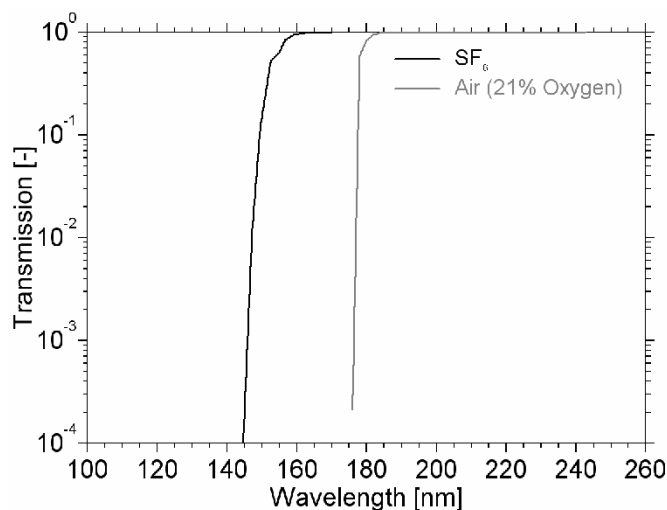
Fig. 6. Calculated light transmission for air (21% molecular oxygen) and SF_6 through 70 mm of the denoted gas at a pressure of 40 psig.

Previous studies revealed that the surface flashover path can be affected by external UV light illumination via photoemission of electrons from the surface if the wavelength range is extending down to ~ 320 nm and below (no noticeable impact for

light in wavelength range > 400 nm) [8]. Although these tests were done in a nitrogen environment at atmospheric pressure across a polycarbonate surface (Lexan), there is little reason to doubt that the wavelength range between 160 nm and 320 nm will play an important role in surface flashover initiation under the conditions found in the LTGS. The primary difference is expected from the photoemission yield that varies from material to material.

While the above clearly shows that UV (~ 180…360 nm) and even VUV (< 180 nm) light can easily propagate in the conditions found in the LTGS it still needs to be confirmed that the volume spark actually produces light emission in the spectral range of interest, i.e. between 160 and 320 nm.

The spectral sensitivity of the spectroscopic system is primarily determined by the spectrograph grating, the fiberoptics (UV grade fused silica fiber), and the camera's photocathode quantum efficiency. An inverse apparatus function accounts for these internal losses, and can be multiplied by the collected data to yield the actual spectra. This function is determined using two calibration sources with known outputs. The first source is a deuterium lamp (#63162 bulb from Newport) and the second is a high pressure xenon lamp (#6254 bulb from Oriel). Both sources have a relatively well defined output in specific wavelength ranges and the combined response was used to calculate the apparatus function. Any raw data recorded by the ICCD is typically in counts, while the scaled data, which account for the losses in the collection system, is labeled as relative intensity in arbitrary units. All spectra shown in the following were corrected using the calibration curve given in Fig. 7.
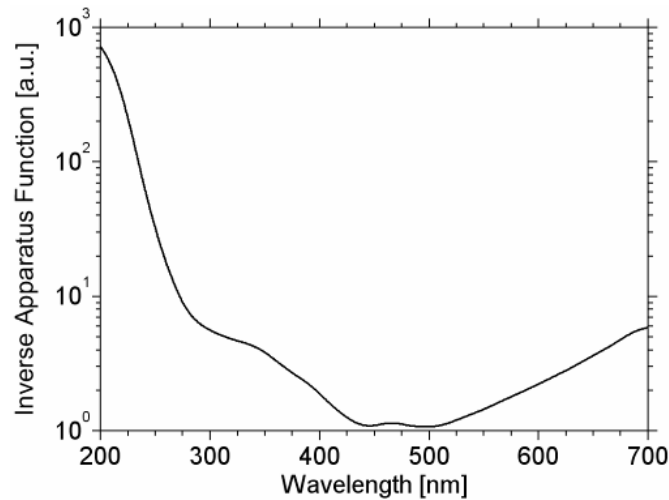
Fig. 7: Scaling curve for all collected spectra, accounting for internal loss in the collection apparatus, spectrograph, and imaging camera.

III. Results

A. Imaging

For accurate modeling of the vertebrae section of the LTGS, stainless steel electrodes with similar geometries to those in the switch are utilized with 9.25 mm gap spacing. The gap is imaged concurrent to the collection of spectra. These images are time integrated over the entire discharge. During testing the camera shutter is held open and the aperture is set to a minimum. Flashovers at lower pressures yield dimmer and more diffuse spark channels, with multi-channel sparks, as in Fig. 8, occurring roughly a fifth of the time. As the pressure is increased the discharge becomes more intense and multi-channel formations are still observed, as seen in Fig. 9 and 10. Multi-channel discharges are desired, as they decrease the switching time of the gap.
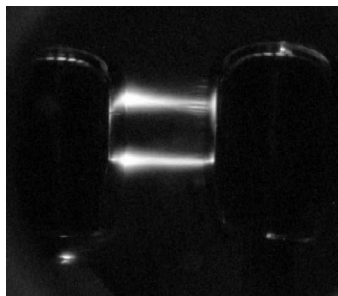
Fig. 8: Time integrated image of volume breakdown between two stainless steel electrodes in SF_6 at 10 torr. No Neutral Density used. Charged electrode is on the left.
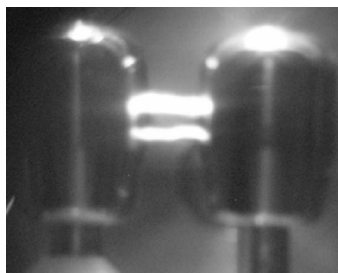
Fig. 9: Time integrated image of volume breakdown between two stainless steel electrodes in SF_6 at 20 psig. Image attenuated by Neutral Density filter of ND = 2. Charged electrode is on the left.

Fig. 10: Time integrated image of volume breakdown between two stainless steel electrodes in SF_6 at 40 psig. Image attenuated by Neutral Density filter of ND = 3. Charged electrode is on the left.

B. Breakdown Voltage

An additional effect of the increased pressure can be seen in the breakdown voltage, as shown in Fig. 11 below. The voltage at breakdown is recorded for pressures ranging from 10 Torr to 40 psig. It should be noted that in the pressure regime below 20 psig, the breakdowns occur on the rising edge of the incident pulse. As expected the increased hold-off voltages correspond to an increase in the delay time from pulse application to breakdown of the gap, also shown in Fig. 11. Increased hold-off and delay times can be attributed to increased electron energy loss processes, such as inelastic collisions, at higher pressures due to the decrease in mean free path.
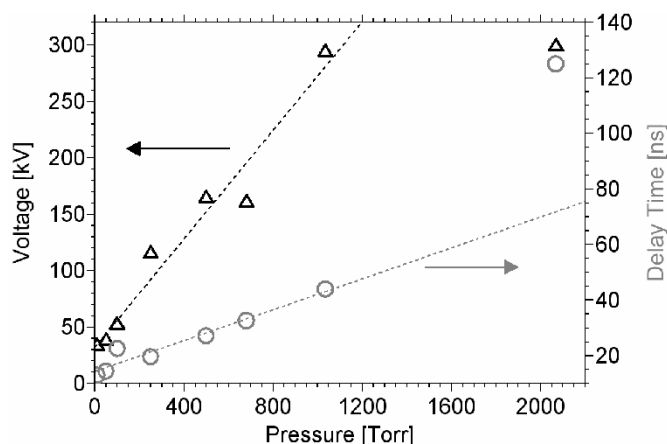
Fig 11: Breakdown voltage and delay time of a 9.52 mm gap in SF_6 at increasing pressures with ~ 50 ns risetime voltage pulse. Delay time is defined as the FWHM from the rise of the voltage pulse to the drop due to breakdown.

C. Optical Emission Spectra

The spectra collected at different points along the discharge path are almost identical. Given the similarities, only the spectrum from the middle fiber will be shown at each pressure. There are several distinct lines present in the spectra, especially at lower pressures. In order to identify these lines the spectra of various elements are calculated and compared to the experimentally collected spectra. In order to calculate the spectra certain values are needed, such as the wavelength of the species specific spectral lines, the level degeneracy, and the associated energy levels and Einstein coefficients for spontaneous emission. This information is gathered primarily from the National Institute of Standards and Technology (NIST) atomic spectra database [9]. From this information the relative line intensities are calculated with the plasma temperature as the principal parameter. Finally, the lines are convolved to account for the effects of the aperture of the spectrograph and natural spreading.

A test element such as fluorine, which was found to be present in the spectra, is used to determine the temperature of the collected spectra. This is done by varying the temperature until the relative intensity of the lines is identical to that of the measured spectra. The determined temperature is then used to calculate the spectrum of various other elements. Once calculated, the various elemental spectra are compared to the collected data.

Spectral line identification, as shown in Fig. 12, indicates the presence of sulfur and fluorine, as expected in a SF_6 discharge, in addition to strong nitrogen lines. It should be noted that the spark plasma is strongly non-thermal at the lower pressures as the calculated spectra in Fig. 12 matched the experimental spectra for an electronic temperature of $T_e = 30,000$ K, N_2 vibrational temperature of $T_v = 3,000$ K, and a N_2 rotational temperature of $T_r = 1,000$K. The calculated spectra will change significantly, i.e. perceivable with the naked eye, if any of these temperatures is changed by $\pm$ 20%.

It should be noted that breakdown studies with high power microwave excitation of SF_6 at 1 atmosphere have revealed that, as expected, small amounts of nitrogen (few percent) in SF_6 already show up prominently in the emission spectrum of a spark, see Fig. 13.
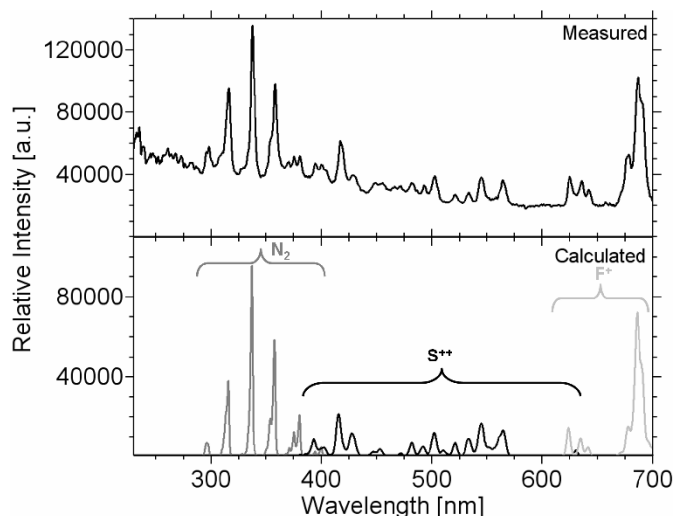
Fig 12: Spectra peak identification using calculated atomic and diatomic spectra. Measured spectra collected in SF_6 environment at 100 torr.
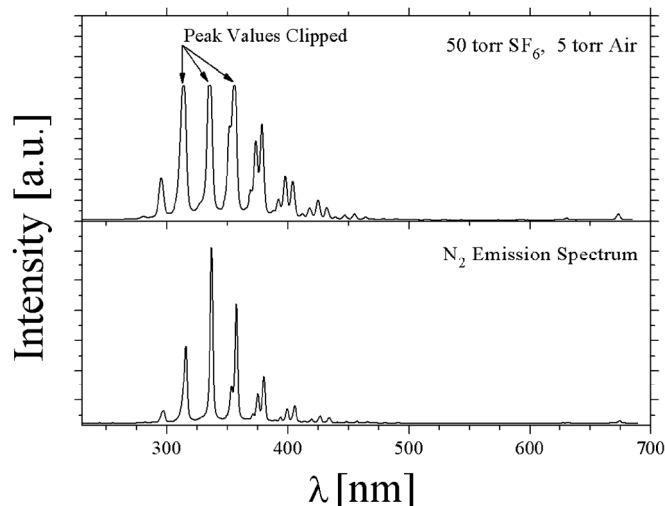
Fig. 13: Optical emission spectra at 50 Torr with high power microwave excitation at 2.85 GHz. *Top* – 10:1 mixture of SF_6 and N_2, *bottom* – control pure N_2.

Following the intensity of the N_2 lines with respect to background pressure in Fig. 14 thru Fig. 16 reveals that the N_2 lines fade as the pressure increases, and are almost indistinguishable at 500 Torr. These lines can be attributed to small leaks in the system that allows the outside environment, specifically air, into the system, primarily at lower pressures. Even with a fixed trace amount of air in the system, the ratio between SF_6 to air will increase with the absolute SF_6 pressure, thus causing fading of the N_2 line features at the higher pressures.

Another trend, especially at higher pressures, is the increasingly broadband nature of the spectra, with a strong contribution in the UV region. This is significant as external UV illumination of the surface in surface flashover experiments has been show to have a profound effect on surface flashover [8]. Illuminating the surface with a UV pulse significantly decreased the delay time, by up to 50%, from pulsed excitation to flashover, in addition to decreasing variations in the delay time from shot to shot. The UV also had a profound effect on the discharge path, resulting in the discharge following the surface as opposed to the electric field line. This effect could easily contribute to the switch failure modes.

The broad features in the spectra at higher pressure are compared to black body radiation. In Fig. 16, Plank's equation,

114

$$\rho_\lambda(T) = \frac{2 \cdot h \cdot c^2}{\lambda^5} \cdot \frac{1}{\exp\left(hc / kT\lambda\right) - 1} \tag{1}$$

at 18,000 K, is used to model the broad features, with a high degree of correlation (*h*: Planck's constant, *c*: speed of light, λ: wavelength, *T*: blackbody temperature). Hence, one might assume that the higher the pressure the closer the spectral output will be to a black body radiator. However, the spark plasma is still not completely thermalized at the 40 psig pressure as indicated by spectral line features superimposed onto the broad background.

Nevertheless, the estimated temperature of ~18,000 K for the SF_6 spark falls within the range of centerline temperatures measured for a stationary arc at a pressure of 120 psig (15,500 K for 400 A and 27,000 K for 13,000 A) [10].
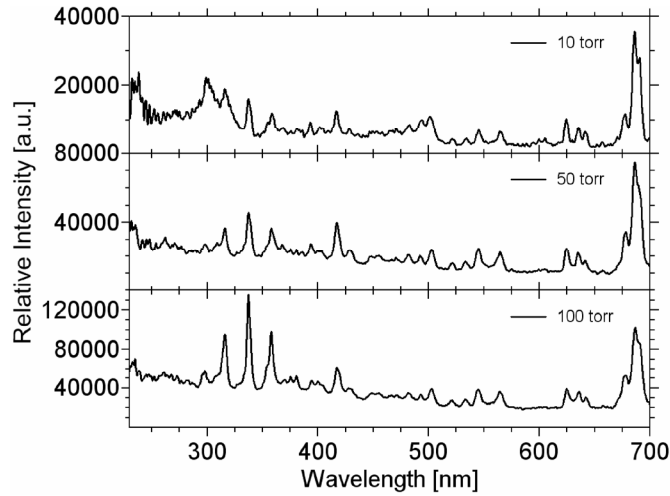
Fig. 14: Spectra collected from a volume discharge in SF_6 at various pressures. The 100 Torr spectrum exhibits more N_2 contamination.
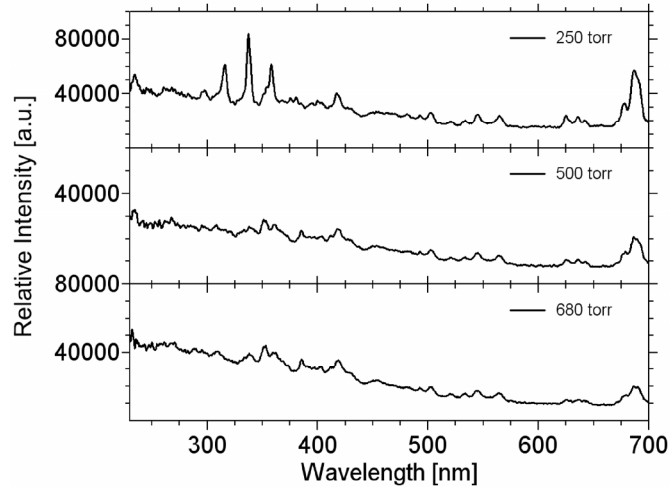
Fig. 15: Spectra collected from a volume discharge in SF_6 at intermediate pressures.
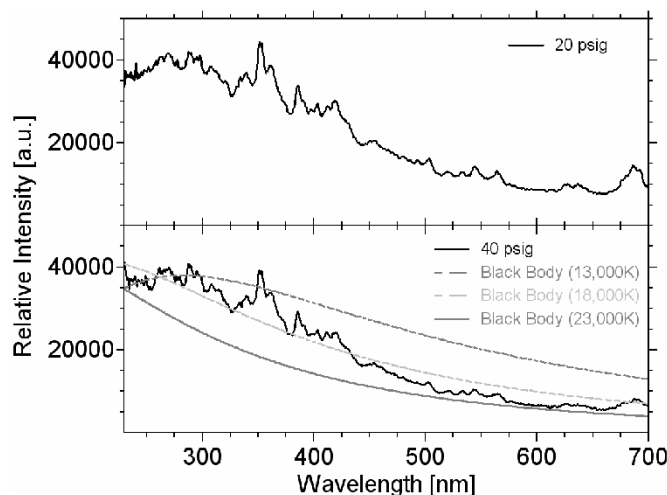
Fig. 16: Spectra collected from a volume discharge in SF_6 at high pressures.

Photoelectric emission from the surface increases with an increased photon energy, or decreased wavelength [11], [12]. As the spectrum broadens, higher intensity is seen in the lower wavelength ranges below 320 nm. Obviously, a higher UV output from the volume spark will liberate an increased number of photoelectrons from the envelope surface.

Due to the transient nature of the switching process one must assume that the electric field amplitude at the envelope is still considerably high even if the volume sparks in the cascade have formed. Hence, the increasing number photoelectrons with the non-zero field at the envelope in the early moments of switching are likely contributing to the observed LTGS envelope failure.

IV. Conclusions

Photoemission of electrons by UV photons impacting the envelope is one of the suspected reasons that can initiate the unwanted tracking along the inside envelope surface in the LTGS. It is shown that a significant amount of UV light is produced by the volume spark in high pressure SF_6. The more intense light output is in the wavelength regime below 320 nm; a regime that has been identified in previous research as having a distinct effect on the spark path of flashover. The majority of species contributing to the observed optical emission spectra between 230 and 700 nm has been identified. While it was possible to estimate the volume spark's electronic temperature (~35,000 K) for the lower pressures (50 torr) using individual spectral line, at 40 psig the broadband features mask distinct atomic or molecular lines. However, assuming black body radiation the temperature is estimated to be of the order of 18,000 K.

The absence of metal lines in any of the observed spectra is a result of the rather low coulomb transfer and low current amplitude (~ 2 kA) in the test setup. It should be assumed that the spectral shape will change with the current amplitude increased into the 100 kA regime in future research. Overall, our results support the hypothesis of UV radiation contributing to the initiation of switch failure.

REFERENCES

[1]   J. P. Corley, et. al., "Tests Of 6-MV Triggered Switches On APPRM At SNL", Digest of Technical Papers in Pulsed Powere Plasma Science, vol. 2, pp. 1778 – 1781, 2002.
[2]   J. P. Corley, et. al., "Development/Tests of 6-MV Triggered Gas Switches at SNL", Proc. 14th Pulsed Power Conference, vol. 2, pp. 875 -878, 2003.

116

[3]   A. M. Casanovas, J. Casanovas, V. Dubroca, F. Lagarde, and A. Belarbi, "Optical detection of corona discharges in SF_6, CF_4, and SO_2 under dc and 50-Hz as voltages," J. Appl. Phys., vol. 70, pp. 1220-1226, 1991.

[4]   A. Lemzadmi, N. Bonifaci, A. Denat, and M. Nemamcha, "Light emission from corona discharge in SF_6 and SF_6/N_2 gas mixtures at high pressure," Eur. Phys. J. Appl. Phys., vol. 33, pp. 213-219, 2006.

[5]   K. Fujii, M. Yamada, A. Tanaka, and K. Kurosawa, "Emission spectrum of partial discharge light in SF_6 gas," Proc. IEEE Intl. Symp. on Elect. Insul., June 1992.

[6]   C. Zetzsch, "UV absorption cross sections of sulfur hexafluoride and acetonitrile," presented at the International Ozone Symposium, 1988, published in: Ozone in the Atmosphere (R.D. Boikov and P. Fabian, Eds.), DEEPAK Publishing (1989), 685-689.

[7]   J.E. Frederick and J.E. Mentall, "Solar irradiance in the stratosphere: Implications for the Herzberg continuum absorption of O_2, " Geophys. Res. Lett. 9, 461-464 (1982).

[8]   K. P. Morales, J. T. Krile, A. A. Neuber, and H. G. Krompholz, "Pulsed Dielectric Surface Flashover in Atmospheric Conditions," IEEE Trans. on Dielectrics and Electrical Insulation, vol. 13, no. 4, pp. 803-809, Aug. 2006.

[9]   NIST Atomic Spectra Database Lines Form, online at: http://physics.nist.gov/PhysRefData/ASD/lines_form.html

[10] J.J. Lowke and R.W. Liebermann, "Predicted Arc Properties in Sulfur Hexafluoride," J. Appl. Phys., vol. 42, 3532-3539, 1971.

[11] J. Tom, H. A. Verhaart, A. L. Verhage, and C. S. Vos, "Photo-emission of Charged Insulators in Insulating Gases," Proceedings of the 2nd International Conference on Conduction and Breakdown in Solid Dielectrics, pp. 301-307, Erlangen, 1986.

[12] A. A. Guzhov, and Yu. A. Shuba, "The Photoemission of Some Massive Insulators in the Vacuum Ultraviolet," Optical Technology, Vol. 38, No. 4, pp. 198-199, April 1971.

John T. Krile (S'98–M'06) was born in Terra Haute, Indiana. He graduated from Texas Tech University in Lubbock, TX in 2006 with a Ph.D. degree in electrical engineering. He worked as a Research Assistant from 2002 to 2006 at the Center for Pulsed Power and Power Electronics. After graduating he has continued at Texas Tech as a Senior Research Associate. His research interests include surface flashover physics, high-power microwaves, explosively driven pulsed power, and compact pulsed power systems. He has published more than 12 journal articles and conference papers.

Russell Vela (S'01) was born in McAllen, TX. He received his B.Sc. degree in electrical engineering from Texas Tech University in Lubbock, TX in 2006. He is currently working as a Research Assistant for the Center for Pulsed Power and Power Electronics at Texas Tech University while pursuing his M.Sc. degree in electrical engineering.

Andreas A. Neuber (M'97-SM'03) was born in Aschaffenburg, Germany. He received the Dipl.-Phys. and Ph.D., ME, degrees from the Darmstadt University of Technology, Germany, in 1990 and 1996, respectively. He was a full time scientific employee at the institute of Energy- and Power Plant Technology, Darmstadt University of Technology, from 1990 through 1996, in the area of nonlinear laser spectroscopy and chemical reaction kinetics in combustion. He joined the Texas Tech University, Lubbock, in 1996 and is currently Associate Professor in Electrical Engineering. His present research interests are high-power microwaves, unipolar surface flashover physics, and explosive-driven pulsed power. He has published more than 90 journal articles and conference proceedings paper.

Hermann Krompholz (SM '84) received the Ph.D. degree in physics from Technical University Darmstadt, Germany, in 1977. He was research associate at TU Darmstadt from 1977 to 1982, working on nonequilibrium phenomena in high energy density plasmas. From 1982 to 1985, he joined Texas Tech University, Lubbock, with activities in the areas of diffuse discharge opening switches and spark gap erosion. After a brief stay at the Fraunhofer Institute for Laser Engineering and Technology in Aachen, Germany, he rejoined the faculty at Texas Tech University in 1987, where he is now Professor of Electrical and Computer Engineering/ Physics. His research interests include several aspects of pulsed power physics and technology, with emphasis on the physics of electrical breakdown in gases, liquids, and along surfaces. He has published about 110 journal articles and conference proceedings papers.

APPENDIX C

PULSED DIELECTRIC SURFACE FLASHOVER IN AN SF$_6$ ENVIRONMENT

John T. Krile, *Member*, *IEEE,* Russell Vela, *Student Member*, *IEEE,* Andreas A. Neuber, *Senior Member, IEEE*, and Hermann G. Krompholz, *Senior Member*, *IEEE*

Abstract— **A recently upgraded Laser Triggered Gas Switch, LTGS, at Sandia National Laboratories has developed a failure mode resulting in the breakdown spark tracking to the inside of the containment envelope. These breakdowns along the surface, or surface flashovers, degrade the performance of the overall switch, causing the switch to pre-fire in the successive shot. In the following, experimental results of pulsed surface flashover across different dielectric materials in SF$_6$ primarily at atmospheric pressure as well as flashover and volume breakdown in SF$_6$ at pressures from 1.3 kPa to 365.4 kPa are presented. In addition to fast voltage and current monitoring of the breakdown event, an increased emphasis was put on imaging the event as well as gathering optical emission spectra (~200 nm to 700 nm) from it. As much as possible, the small scale experiments were designed to reproduce at least partly the conditions as they are found in the large 5 MV switch. An effort was made to determine what changes could be made to reduce the occurrence of surface flashovers, in addition to some broadly applicable conclusions on surface flashovers in an SF$_6$ environment.**

Index Terms—**Flashover, Dielectric materials, Electric breakdown, Ultraviolet radiation effects**

I. INTRODUCTION

As part of an extensive overhaul of the Z-machine, located at Sandia National Laboratories, several Laser Triggered Gas Switches, LTGS, have been upgraded to operate in the 5 MV range [1]. With the new requirements in switching voltage, the present LTGS design has been deemed inadequate due to switch failure occurring after only a few shots. The primary failure mode was surface flashover in the high pressure gas (SF$_6$, > 365 kPa) on the inside of the polymethyl methacrylate, or PMMA, envelope. This surface flashover occurred initially during the regular cascade switching process without affecting the switch's electrical performance. However, the switch tended to pre-fire in the successive shot once flashover has occurred. The damage to the envelope has to be repaired before normal switch operation can resume.

It has been shown previously that a significant amount of UV radiation was generated during normal switch operation due to the volume breakdown between the cascade trigger electrodes [2]. In this investigation, the spectral output of dielectric surface flashover was analyzed over a wide pressure range (1.3 kPa to 365.4 kPa) and specifically compared to volume breakdown optical emission spectra taken at 365.4 kPa.

If an envelope flashover cannot be avoided, triggered due to, for instance, emission of photoelectrons from the surface, it is prudent to identify materials that exhibit the least damage to a surface flashover spark. In the present investigation, several electric material properties were compared, such as flashover delay time and the likelihood of spark formation along the surface under fields with a non-negligible component normal to the surface. The spectral output of a surface flashover along various surfaces in SF$_6$ was observed and high resolution imaging of the surface was utilized for surface damage assessment. The surface was also examined for possible sulfur deposits, as seen in previous research [3].

II. Experimental Setup

A. Atmospheric Pressure Apparatus

While the emphasis of this research was to closely mimic the conditions within the LTGS, which is typically pressurized to 365 kPa of SF_6, a much wider pressure range was covered to reveal possible pressure dependent tendencies. For instance, some initial testing was performed in a small surface flashover chamber, capable of maintaining an SF_6 environment at atmospheric pressures. This chamber as well as a second higher pressure chamber were excited with an 8 stage Marx generator with up to 45 kV charging voltage per stage. For this atmospheric chamber, the Marx output voltage was typically set to 90 kV with a 50 ns rise time, which led to a charge transfer of 60 µC.

The atmospheric testing setup was an adaptation from a previous project in which extensive field simulations and impedance matching between the transmission line and electrode feed-throughs was done to ensure minimal signal distortion and system robustness [2]. The design utilizes a coaxial geometry of 52-Ω impedance throughout the setup, see Fig. 1. The chamber was constructed of half inch thick polycarbonate to allow for easy optical access. Dotted lines in Fig. 1 represent a removable outer conductor which contains a small hole for imaging of the gap. Two ports, located at the base of the chamber, allowed for a continuous flow of SF_6. The chamber was kept at a slight overpressure during testing to prevent outside contamination.
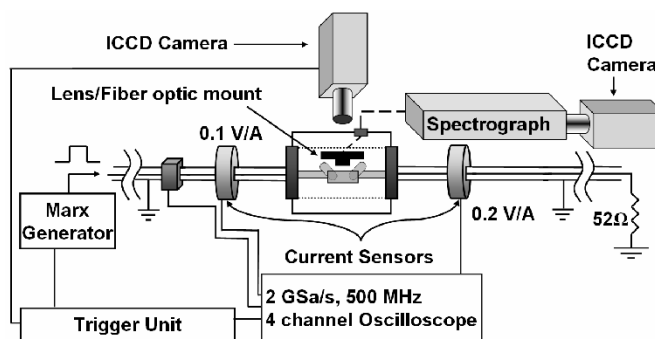
Fig. 1. Overview of the atmospheric chamber setup. The dotted lines represent the removable outer conductor and the dashed lines represent fiber optic cables.

B. High Pressure Test Apparatus

A high pressure chamber was utilized that enabled adjusting the pressure from the kilopascal range up to 365.4 kPa, see Fig. 2. In this case, the Marx output voltage was increased to 320 kV (~ 220 µC charge transfer) for the high pressure chamber to facilitate reproducible flashover.
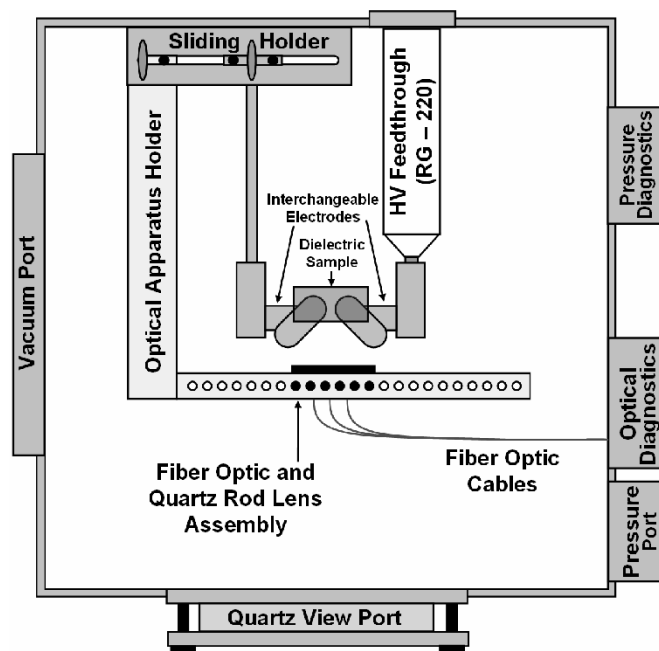
119

Fig. 2. Overview of the high pressure chamber (25.4 cm x 25.4 cm x 25.4 cm). Additional electrodes and flashover surfaces are omitted for clarity.

For the presented research, the second chamber was configured with a set of electrodes identical to the atmospheric setup. The chamber was pressure tested up to 500 kPa, and a minimum pressure in the millipascals range was achieved. The ability to evacuate the chamber was useful in eliminating the possible effects of environmental contaminations, specifically nitrogen gas, on the flashover processes. The chamber has been equipped with several ports to allow for easy access by the various diagnostics. The gap was excited with the same Marx generator discussed previously.

C. Electrical Diagnostics

Measurement of the breakdown required instrumentation with high temporal resolution. For this reason, a capacitive voltage divider with a sensitivity of 109 mV/kV and a rise time better than 1 ns was incorporated on to the 52-Ω transmission line. Traveling wave current sensors were utilized for the current measurements and have a sensitivity of 0.1 V/A with a ~1 ns rise time. All signals were then recorded using a 500 MHz bandwidth, 2 GSa/s, Agilent Infinium oscilloscope.

D. Optical Diagnostics

The flashover event was imaged using an Andor Technology Intensified CCD DH-734 camera with nanosecond temporal resolution. This camera was fitted with a zoom lens and positioned directly outside the flashover chamber. In the atmospheric chamber the camera was focused on the dielectric gap through a small hole in the detachable outer conductor. Optical gate times of 3 to 300 ns were utilized for the flashover experiments. In the high pressure chamber images of the flashover gap could either be taken through the quartz view port or through a secondary view port in the upper flange of the chamber. The second method was utilized to allow for both imaging of the gap (time integrated with digital camera) and collection of optical emission spectra concurrently.

Spatially resolved optical emission spectra were collected using a specially designed apparatus, see Fig. 3, consisting of three quartz (Suprasil) cylindrical rod lenses. These lenses were positioned to collect light from three rectangular shaped regions in the gap and focus it into three fiber optic cables which were fed into a spectrograph, Oriel MS 257. This spectrograph was an imaging spectrograph that had toroidal mirrors designed to allow multiple vertical points, or fiber optic inputs, to be diffracted at one time. This

feature was used to collect spectra from different positions along the discharge path at the same time.
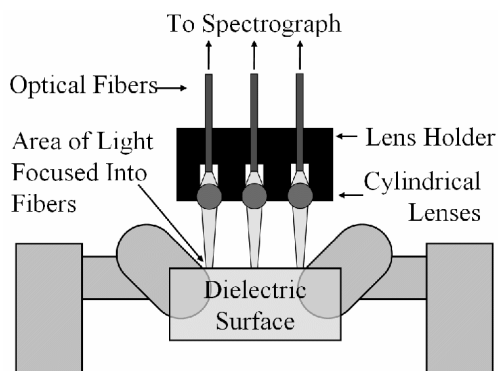
Fig. 3: Cross-section of the optical emission collection apparatus.

For quantitative optical emission spectroscopy, the spectral response of the complete spectral apparatus has to be considered. In this case, the spectra collected by the CCD will be a function of the spectral sensitivity of the entire system, which is primarily determined by the spectrograph grating, the fiber optics (UV grade fused silica fiber), and the camera's photocathode quantum efficiency. Two light sources with known spectral output were utilized to determine the inverse spectral response of the apparatus, which was given in detail elsewhere [2]. Note that all spectral data shown in this manuscript was corrected with the spectral response.

In addition to the sensitivity of the collection apparatus, the attenuation of the environment must also be considered. However, the expected absorption due to SF_6 for distances within the chamber or LTGS conditions has been shown negligible above 160 nm through the visible [2]. Hence, no correction due to "cold" gas absorption has been made for the wavelength range between 200 nm through 700 nm.

E. Electrode, Dielectric Geometry

The electrode geometry, see Fig. 4, was chosen to produce an electric field with a strong electric field component normal to the surface. Both electrodes are embedded approximately 13.7 mm into the dielectric material. Electrostatic field simulations were done on the electrode geometry using Ansoft's Maxwell 3D simulation program.
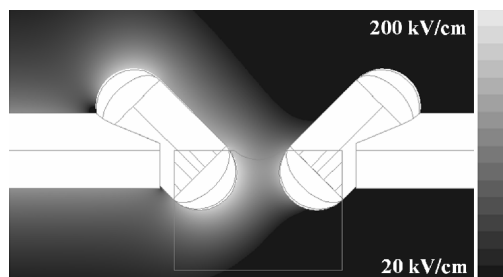
Fig. 4. Maxwell 3D simulation of electric field vector for the angled electrode geometry in a cut plane normal to the dielectric surface. Left electrode charged to 72 kV, right electrode grounded. Gap spacing of 7.87 mm.

Two different surface geometries were tested. Some dielectric samples had surfaces that were not altered or machined except for the electrode slots. These samples were utilized for optical spectra collection. In order to increase the surface path length between the electrodes a groove was machined along the surface of the sample, see Fig. 5.
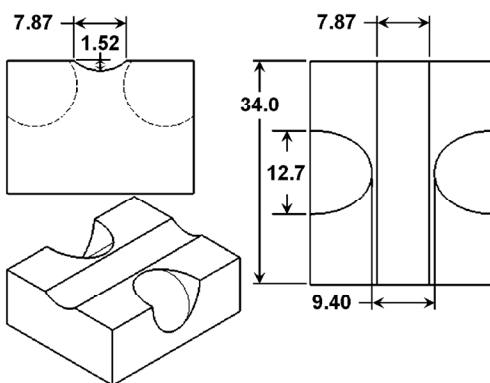
Fig. 5. Dielectric sample geometry and dimensions used for testing. All units in millimeters.

In both cases the overall dimensions of the dielectric samples remained the same. Due to different machining methods, the groove depth varied slightly from sample to sample, however, the basic field shape was the same for all grooved samples.

Preparation of the samples involved removing the protective film used during machining and gently cleaning off any residual adhesive with cyclohexane and lint-free wipes. The sample was then inserted into the test chamber with powder-free latex gloves in order to prevent contamination of the surface. Before testing, the chamber was evacuated to 0.01 Pa to efficiently remove background gases (humidity) from the chamber and at least to some extend from the chamber walls, and the dielectric surface. In a final step, the chamber is backfilled with SF_6 to the desired pressure.

III. Results and Discussion

A. Reference Waveforms

For each flashover event, the camera gate (when applicable), current, and voltage waveforms were acquired and recorded. A representative set of waveforms for a typical surface flashover event in the atmospheric chamber is depicted in Fig. 6. The typical flashover voltage waveform was characterized by a rise in voltage as the voltage pulse is applied to the gap, followed by a sharp drop in voltage as flashover occurs. The collapse of the voltage due to flashover was accompanied by the simultaneous rise in current. Note that the first portion of the current (or voltage waveform) remained unchanged from shot to shot. That is, the small hump in current is due to charging of the capacitance associated with the gap and the supporting structure. This charging is considered complete when the current returns to zero, indicated by the first dashed line in Fig. 6. All recorded flashovers occurred after fully charging of the gap, that is after the first dashed line. The Marx output a negative voltage pulse and had a maximum coulomb transfer of ~220 µC at maximum output voltage. The breakdown delay time was defined as the full width at half maximum from the voltage rise to the voltage drop due to breakdown. The output voltage was adjusted to ensure no flashover events occur during the voltage rise. The voltage and current signals typical in the high pressure chamber were similar to Fig. 6; however, since the gap has a higher breakdown voltage at higher SF_6 pressure, the Marx output voltage was significantly increased to reliably achieve a breakdown.
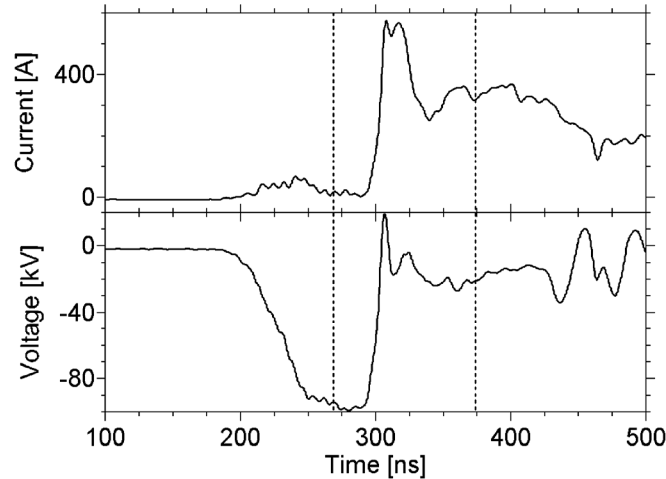
Fig. 6. Representative waveforms of current and voltage signals for flashover in SF_6 at 90.6 kPa. Dashed lines represent the beginning and end of the camera exposure.

B. Imaging the Discharge

For imaging of the flashover event with the ICCD camera, the surface was slightly angled to provide a side-on view of the flashover path. Given that the electric field leads away from the surface it was desired to know whether the discharge would form along the field lines, as in volume breakdown, or along the surface. Following the surface would indicate the surface played some role in the spark development and the potential for increased surface erosion. If the surface was important for the flashover path then varying the dielectric material could have an impact on the performance of the switch by limiting undesirable surface tracking. Fig. 7 and 8 show examples of the varying degrees of surface tracking observed.
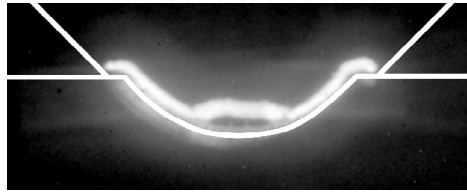
Fig. 7: Grooved Teflon sample at 90.6 kPa of SF_6. Gap = 10.53 mm, T_{delay} = 92 ns, $V_{pulse} \approx$ 91 kV. White lines indicate the location of the surface and electrodes.
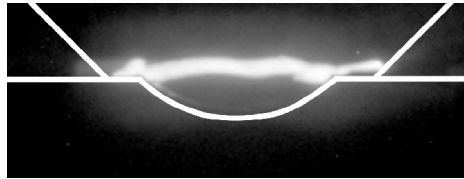
Fig. 8: Grooved Teflon sample at 90.6 kPa of SF_6. Gap = 9.48 mm, T_{delay} = 307.3 ns, $V_{pulse} \approx$ 90 kV. White lines indicate the location of the surface and electrodes.

It became apparent that surface tracking varies widely depending on the dielectric material, see Table 1. From the table, it can be seen that Teflon produced the largest percentage of flashover liftoffs, which would make it the preferred choice in applications where surface tracking or erosion is undesirable.

The epoxies listed in Table 1 were selected by Sandia in order to determine the feasibility of producing the envelope material in-house. The epoxies consist of an Epon 826 resin with either a D-400

(polyoxypropylene diamine) or T-403 (polyoxypropylene triamine) curing agent. The second material also incorporated a degassing agent, KF-865.

While data on quantum yields for photoemission is relatively scarce, especially for custom epoxy compounds, it is generally accepted that Teflon's photoemission coefficient is smaller than most dielectrics [4]-[5]. As stated previously, a decrease in surface liftoffs indicated a lesser interaction between the discharge and the surface. It is believed that, at least in part, this interaction involves the UV radiation emitted by the spark itself producing photoelectrons from the surface [6]. As such, the quantum yield of the envelope should be minimized either through careful material selection or the application of a UV absorbing coating to prevent surface flashover.

Table 1. Various dielectrics and there percentages of liftoff.

Materials	Lift-off Percentages
Teflon	50%
Polycarbonate	0%
Epon 826/T-403	13%
Epon 826/D-400/KF-865	18%

C. Dielectric Sample Degradation

In addition to imaging the discharge, the dielectric samples were examined to assess the damage or tracking produced by the discharge. Any damage to the surface could affect subsequent flashover events. This phenomenon is known as conditioning the surface. Each dielectric was photographed using an optical microscope. This process documented any visible damage on the surface of the material. Next a scanning electron microscope (SEM) was utilized to achieve better resolution in areas of interest. This proved useful when damage could not be seen or was vague under a light microscope with its limited magnification. Surface tracking damage was clearly visible using the optical microscope for some materials, as seen in Fig. 9. Fig. 10 shows that, although Teflon flashover did follow the surface (≈ 50% of the time), the flashover did not leave visible tracking on the surface, as opposed to the other materials.
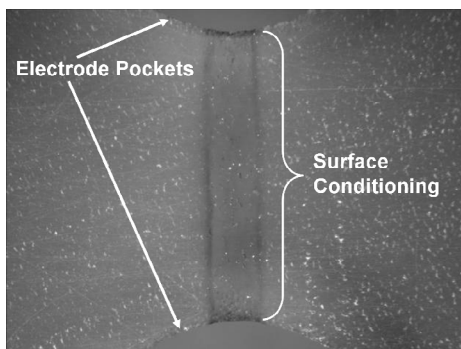

Fig 9: Smooth surface dielectric sample 826/D400/KF-865 after 38 discharges (1 atm SF$_6$, 30 µC). Similar to all epoxy mixtures tested. Gap distance of ~9.9 mm.
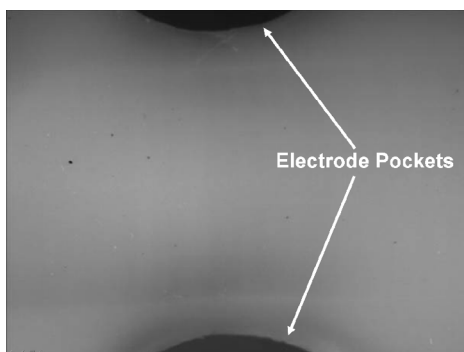
Fig 10: Grooved Teflon after 10 discharges (1 atm SF_6, 30 µC). No damage visible other than groove machining. Gap distance of ~10.5 mm.

While no notable damage was found on Teflon with the SEM, the epoxy, see Fig. 11, exhibited significant changes. Since the SEM was sensitive to both topography and composition, the observed pattern could have been simply due to deposits on the surface or due to changes in the material, including charging of the material just below the surface.
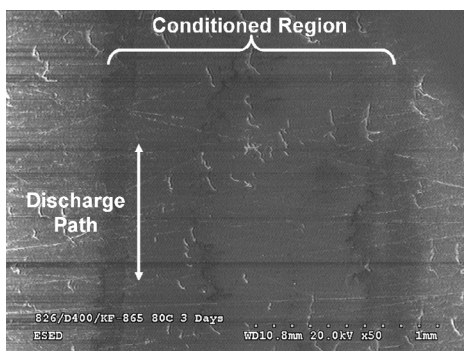
Fig 11: SEM image of smooth surface dielectric sample 826/D400/KF-865 after 38 discharges (1 atm SF_6, 30 µC). The flashover region is denoted by the dark area in the center of the image which lacks significant machining marks. The region appears to be altered compared to the surrounding epoxy surface. Imaged area is ~2.5 mm wide.

The same materials were tested in the high pressure chamber and displayed similar damage characteristic as in the atmospheric chamber. Again, Teflon showed no signs of visible damage, unlike the epoxy and polycarbonate samples. Examination of the polycarbonate sample with the SEM revealed significant damage at the electrode surface interface, as seen in Fig. 12. The polycarbonate was flashed 40 times, five times at each of the following pressures: 1.3 kPa, 2.7 kPa, 6.7 kPa, 13.3 kPa, 33.3 kPa, 90.6 kPa, 227.5 kPa, and 365.4 kPa. Since changes in the structure of the material would show up in the SEM images as well, it could again be speculated that the internal cracking and discoloration of the material was due to a change in the composition of the material.
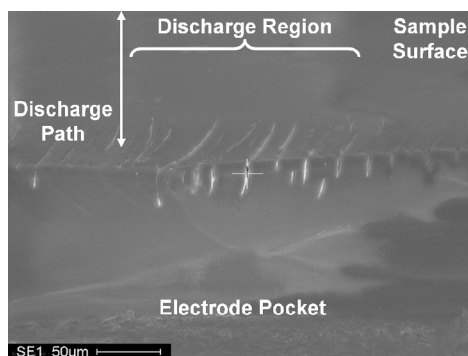
Fig 12: SEM image of smooth surfaced optical grade polycarbonate. View is into the hole for the electrode, the upper surface is the where the flashover occurred. The cracks visible in the surface are located on the edge of the surface corresponding to the electrode/dielectric interface. Discharges occurred 40 times at eight various pressures (Varied pressure SF_6, 108 μC).

In addition to the damage observed, spherical deposits were observed on the surface of the epoxy, as seen in Fig. 13. Utilizing the SEM, X-Ray spectroscopy analysis was performed on the deposits revealing that they consisted primarily of sulfur. Subsequent analysis showed that sulfur deposits also were present in the crack in the polycarbonate surface, seen in Fig. 12. The sulfur deposits were found imbedded in the surface as opposed to on the surface, as a settled byproduct of the discharge would be. These discharge byproducts were eventually found for all dielectric materials tested with the exception of Teflon, although in some of the materials sulfur deposits took the form of flakes, rather than spheres. It is possible that sulfur exist on the Teflon as well, however locating it is difficult due to the nearly identical coloration assigned to sulfur deposits and Teflon surface by the SEM. These deposits further contribute to the surface conditioning and showed that the background gas could also play a role conditioning.
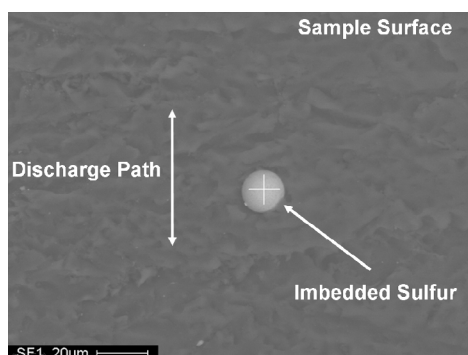
Fig 13: SEM Image from dielectric material 826/D400/KF-865 used for X-Ray Spectroscopy analysis (90.6 kPa SF_6, 30 μC).

D. Flashover Delay Time

The study of the time delay for breakdown was most revealing for the pulsed voltage hold-off capabilities of different materials. All materials were tested under identical environmental conditions, 90.7 kPa of SF_6. In the ideal case the field strength of all tested samples would be identical, however, due to minor gap adjustments (± 1.0mm) necessary to fall within the atmospheric breakdown chamber's voltage limits (90kV), the field strength varied between samples. As a result, a direct comparison of the time delays was not straightforward and had to be approached with caution. The average delay times of the tested materials are depicted in Fig. 14, sorted by applied field strength. All delay times have been averaged over more than 60 shots per material type. The figure can be interpreted such that if a material exhibits a longer breakdown delay time at a larger applied field than another material, its hold-off strength can be considered superior.

Fig 14: Dielectric material comparison of average time delays. Samples arranged by field strength (asterisk indicates one sample only tested).

Despite the varying field strengths, Fig. 14 indicates that Teflon had a longer breakdown delay time even at a higher applied field when compared to the Lexan and the epoxies. The one sample of Plexiglas (material taken directly from an unused Z switch envelope) exhibited the best performance at 1 atmosphere of SF_6, however, this value has to be treated with some caution as only a single sample could be tested her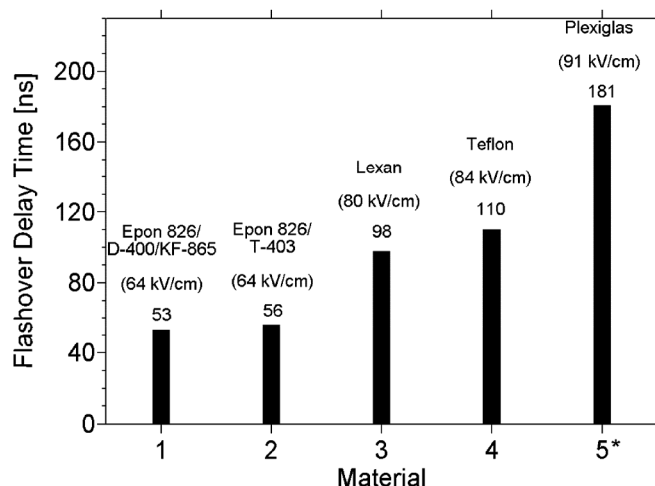e. Nevertheless, the change of flashover delay time of Plexiglas was very pronounced, and in general was much larger than any of the sample to sample variations for the other materials. Polycarbonate, Teflon, and Plexiglas have dielectric constants between ~ 2 to 3, while the epoxy based materials fell out of this range with a relative permittivity of ~ 5, which could help explain their poor performance. A higher dielectric constant could lead to increased electron emission at the triple point. Given their propensity for surface conditioning and low hold-off times, the epoxy based materials were not suited for high voltage switch envelopes.

E. Optical Emission Spectra

Using the optical emission collection apparatus described earlier, spectra was collected from three points along the spark channel, see Fig. 15. The first lens collected light from just in front of the negative high voltage (charged) electrode, the second observed the middle of the gap, and the third observed just in front of the grounded electrode. In general, the spectra from different positions in the gap were quite similar over the entire length of the gap, as shown in Fig. 15. However, one notable difference was the increased UV content just in front of the cathode. This was significant given the suspected interaction of the UV radiation and the dielectric surface.

Most spectral peaks have been identified, including sulfur, fluorine, hydrogen and carbon, see Fig. 16. A temperature of around 30,000 K resulted in the best fit between calculated and experimental spectra. The carbon and hydrogen was of particular significance because it indicates the discharge was removing material from the surface and exciting it. Note that the hydrogen could also be attributed to moisture, not fully removed while under vacuum, being desorbed from the surface. In either case the discharge was altering or conditioning the surface and potentially lowering its flashover hold-off ability.

Fig 15: Spectra collected from a surface flashover of a polycarbonate surface in an SF_6 environment at 6.7 kPa. Spectra are collected from three points along the discharge path, as denoted.
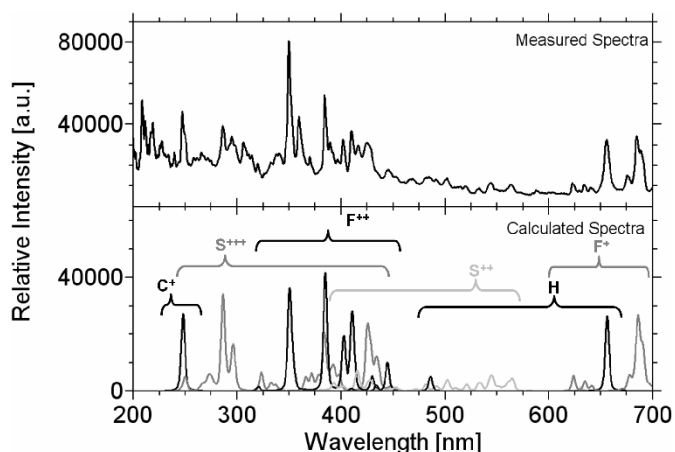
Fig. 16: Spectra peak identification using calculated atomic spectra. Measured spectra collected in SF_6 environment, across a polycarbonate sample, at 6.7 kPa. The calculated spectra are given for a temperature of 30,000 K.

In order to isolate any peaks that have not yet been identified, and to illustrate the underlying, broadband spectra, the identified peaks were added together and subtracted from the original signal. The convolution profiles used in the calculation of the atomic spectra were adjusted to match those of the actual setup. Fig. 17 shows the result of this subtraction. It can be seen that most of the peaks in the 450 nm to 700 nm range have been identified and removed leaving an approximation of the broadband spectra, which was most likely due to contributions from excited SF_6 molecules and recombination.

128
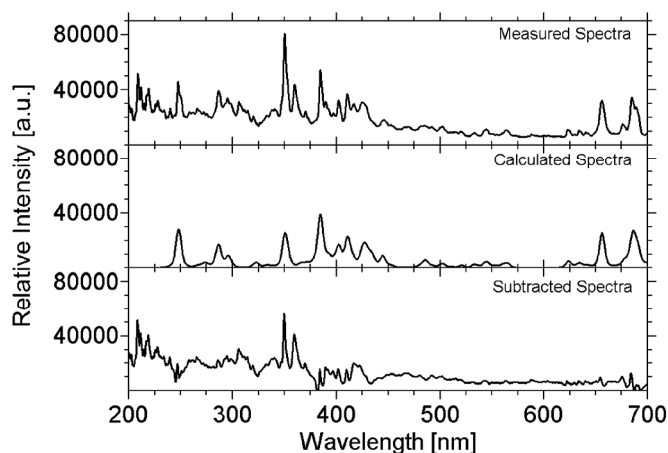
Fig. 17: Calculation of remaining spectra after identified atomic spectra lines are removed. Measured spectra collected in SF_6 environment, across a polycarbonate sample, at 6.7 kPa. The calculated spectra is given for an temperature of 30,000 K.

.

A series of shots were performed while varying the pressure of SF_6 in the chamber, Fig. 18 shows selected results of the 1.3 kPa to 365.4 kPa series of tests. Due to the consistency of the spectra along the discharge path, only the center of the gap is shown at each pressure. All presented spectral data has been scaled by the correction factor to account for internal losses in the collection system discussed previously. At increasing pressures the intensity of the singly ionized fluorine relative to the other atomic/ionic lines was suppressed followed by the weakening of all lines compared to the broadband features and the singly ionized carbon line.
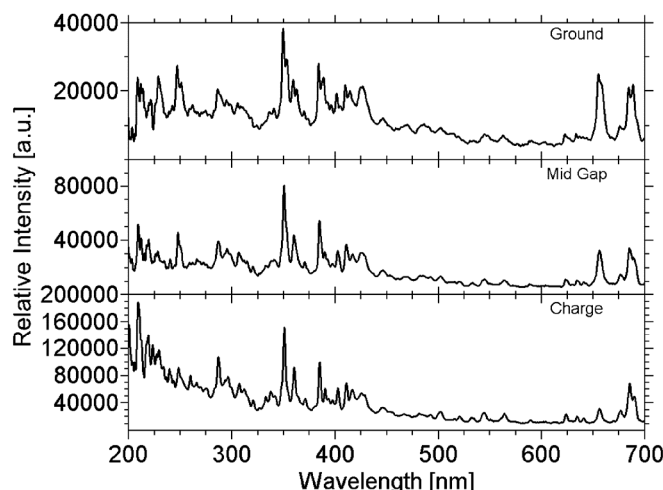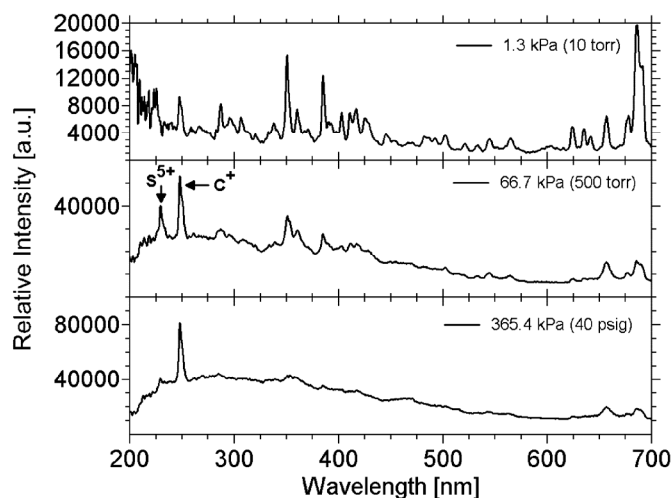

Fig. 18: Spectra collected from a surface flashover of a polycarbonate surface in an SF_6 environment at various pressures. Spectra are collected from middle of the gap at each noted pressure.

Overall, the pressure dependence of the flashover spectra was similar to what was previously measured for volume breakdown [2]. That is, the measured optical emission spectra start out at low pressures as line spectra that are, with increasing pressure, increasingly masked by broadband radiation, as indicated by Fig. 18. The only spectral line in flashover that shows up dominantly at 365.4 kPa was the singly ionized Carbon line at 250 nm, see bottom of Fig. 19. This clearly shows the erosion of the surface as no carbon line was present at the higher pressures for volume breakdown under similar conditions, as shown in Fig. 19.
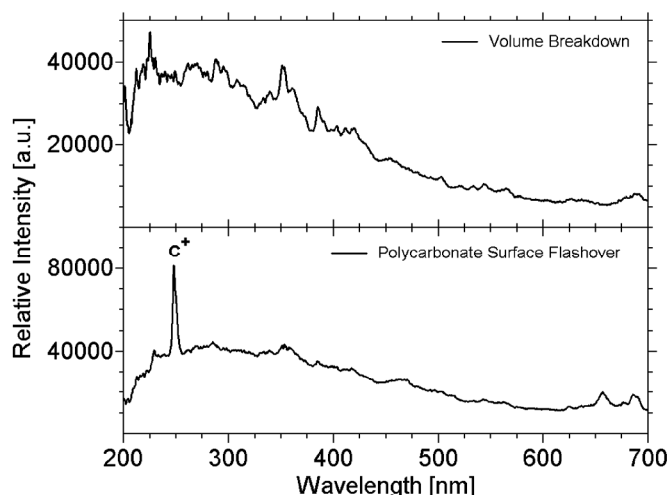
Fig. 19: Comparison of spectra collected from a volume breakdown and a surface flashover of a polycarbonate surface in an SF_6 environment at 365.4 kPa. Spectra are collected from middle of the gap in both cases.

IV. Conclusions

Several aspects of surface flashover along dielectric insulators have been studied in SF_6 environments. Imaging of the discharge along a dielectric surface revealed a material dependence on the discharge path. Even with an electric field leading away from the surface discharges continued to preferentially follow the surface for most materials, i.e. polycarbonate and the epoxies, indicating a strong interaction between the surfaces and the discharge. This interaction was believed to involve the productions of photoelectrons by the surface while exposed to UV radiation generated by the forming discharge, which existence was confirmed by the collected optical emission spectra. Teflon showed the weakest interaction with the surface, following the surface only 50% of the time. This indicated that Teflon, or a material with similar or lower quantum yields for photo emission, would be the preferred choice for minimizing undesired envelope flashovers.

In addition to imaging of the discharge, post-mortem imaging of the samples made the differences in surface conditioning apparent. For instance, the epoxy and polycarbonate exhibited very distinct visible surface damage, as opposed to Teflon that exhibited almost no visible damage. As surface conditioning reduces flashover fields of successive flashover events, Teflon was again shown superior to the other materials. This was further supported by the flashover delay time measurements, which indicated that Teflon would hold off flashover longer under greater field stress than the epoxies.

Comparing volume breakdown and surface flashover optical emission spectra revealed the presence of a strong carbon line in the UV for surface flashover at 365.4 kPa. Since this line was absent in the volume breakdown spectra, it serves as an *in-situ* indicator for surface erosion for hydrocarbon based materials. This also implies a measure of caution should be taken when using hydrocarbon based materials in envelope construction.

The occurrence of sulfur on the dielectric surface, as recorded in literature, was consistent with the prevalent appearance of sulfur ionic lines in the flashover optical emission spectra (SII and SIII). The question remains as to whether these deposits are a cause or result of the poor hold-off characteristics of the materials. Future testing with secondary surfaces placed in the chamber to measure hold-off potential after collecting any deposits created by an initial flashover event should help clarifying the role of the sulfur deposits.

REFERENCES

[1] J. P. Corley, et. al., "Development/Tests of 6-MV Triggered Gas Switches at SNL", Proc. 14th Pulsed Power Conference, vol. 2, pp. 875 -878, 2003.

[2] J. K. Krile, R. Vela, A. A. Neuber, H. G. Krompholz, "Pulsed Volume Breakdown of SF_6 at High Pressures," IEEE Trans. on Plasma Sciences, submitted for publication.

[3] H. R. Hiziroglu, J.M. Kokosa, and A. Przyjazny, "Discharge By-Products of SF_6 in the Presence of Polymeric Materials," Annual Report of IEEE Conference on Electrical Insulation and Dielectric Phenomena, pp. 877, October 1994.

[4] J. Tom, H. A. Verhaart, A. L. Verhage, and C. S. Vos, "Photo-emission of Charged Insulators in Insulating Gases," Proceedings of the 2nd International Conference on Conduction and Breakdown in Solid Dielectrics, pp. 301-307, Erlangen, 1986.

[5] A. A. Guzhov, and Yu. A. Shuba, "The Phototemission of Some Massive Insulators in the Vacuum Ultraviolet," Optical Technology, Vol. 38, No. 4, pp. 198-199, April 1971.

[6] K. Morales, J. Krile, A. Neuber, and H. Krompholz, "Dielectric Surface Flashover at Atmospheric Conditions with Unipolar Pulsed Voltage Excitation," IEEE Trans. Dielectr. Electr. Insul., August 2007, to be published.

John T. Krile (S'98–M'06) was born in Terra Haute, Indiana. He graduated from Texas Tech University in Lubbock, TX in 2006 with a Ph.D. degree in electrical engineering. He worked as a Research Assistant from 2002 to 2006 at the Center for Pulsed Power and Power Electronics. After graduating he has continued at Texas Tech as a Senior Research Associate. His research interests include surface flashover physics, high-power microwaves, explosively driven pulsed power, and compact pulsed power systems. He has published more than 12 journal articles and conference papers.

Russell Vela (S'01) was born in McAllen, TX. He received his B.Sc. degree in electrical engineering from Texas Tech University in Lubbock, TX in 2006. He is currently working as a Research Assistant for the Center for Pulsed Power and Power Electronics at Texas Tech University while pursuing his M.Sc. degree in electrical engineering.

Andreas A. Neuber (M'97-SM'03) was born in Aschaffenburg, Germany. He received the Dipl.-Phys. and Ph.D., ME, degrees from the Darmstadt University of Technology, Germany, in 1990 and 1996, respectively. He was a full time scientific employee at the institute of Energy- and Power Plant Technology, Darmstadt University of Technology, from 1990 through 1996, in the area of nonlinear laser spectroscopy and chemical reaction kinetics in combustion. He joined the Texas Tech University, Lubbock, in 1996 and is currently Associate Professor in Electrical Engineering. His present research interests are high-power microwaves, unipolar surface flashover physics, and explosive-driven pulsed power. He has published more than 90 journal articles and conference proceedings paper.

Hermann Krompholz (SM '84) received the Ph.D. degree in physics from Technical University Darmstadt, Germany, in 1977. He was research associate at TU Darmstadt from 1977 to 1982, working on nonequilibrium phenomena in high energy density plasmas. From 1982 to 1985, he joined Texas Tech University, Lubbock, with activities in the areas of diffuse discharge opening switches and spark gap erosion. After a brief stay at the Fraunhofer Institute for Laser Engineering and Technology in Aachen, Germany, he rejoined the faculty at Texas Tech University in 1987, where he is now Professor of Electrical and Computer Engineering/ Physics. His research interests include several aspects of pulsed power physics and technology, with emphasis on the physics of electrical breakdown in gases, liquids, and along surfaces. He has published about 110 journal articles and conference proceedings papers.

PERMISSION TO COPY

In presenting this thesis in partial fulfillment of the requirements for a master's degree at Texas Tech University or Texas Tech University Health Sciences Center, I agree that the Library and my major department shall make it freely available for research purposes. Permission to copy this thesis for scholarly purposes may be granted by the Director of the Library or my major professor. It is understood that any copying or publication of this thesis for financial gain shall not be allowed without my further written permission and that any user may be liable for copyright infringement.

<u>Agree</u> (Permission is granted.)

<u>Russell Vela</u>_____ __   07/27/07_____
        Student Signature   Date

<u>Disagree</u> (Permission is not granted.)

_____   _____
        Student Signature   Date